Information Processing in the Lateral-Line System of Fish

Julie Goulet
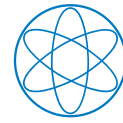
Physik Department
Technische Universität München

Information Processing in the Lateral-Line System of Fish

Julie Goulet

Preface

The nervous system enables animals to get information and react to their environment. Sensory systems are *the doorways* through which animals get information about their surroundings. How they handle this information is crucial and permits animals to create an inner representation of the outside world. In neuroscience therefore studying sensory systems is always an important source of information on how the brain works.

In addition to the traditional human "five senses" (touch, vision, hearing, smell, and taste), there are many other sensory systems that deal exclusively with body-internal processes. For instance, the vestibular system which deals with equilibrium and position in space. Other systems specialize in order to analyze the physical information contained in a particular physical quantity available in the environment of an animal. Many more sensory systems have evolved in other animals.

Aquatic vertebrates use a special sensory system to detect minute water movements: *the lateral line system.* The lateral-line system decodes the information in the water surrounding the fish to enable the fish to identify and localize the source of the perturbation. This thesis deals with *how* a fish can analyze and extract the important information contained in the water motion around its body to create a representation of its environment.

Analyzing water motion is complicated. Unlike light for vision, a moving object in water travels in a continuous medium at smaller velocity. Important parameters such as distance, viscosity, boundary layers must be taken into account.

Organization of this thesis

After reviewing the actual knowledge of the anatomy and the physiology of the fish lateral-line system in chapter 1, a major part of this thesis will show which quantities are measured by the lateral-line detectors (*neuromasts*) and that a minimal model based on the Euler equation can explain accurately the stimuli to the fish lateral-line (chap. 2 and 3). This model will be compared with experimental measurements (chap. 3). We will then characterize (chap. 4) the response of the

lateral-line neuromasts on the skin of the fish to white noise. Using information theory, we will try to characterize which features of the stimulus (displacement, velocity, acceleration) play a role in spikes generation. Chapter 5 will be devoted to how the position of an object can be encoded and decoded by the lateral line periphery and in the brain of the fish. In chapter 6, we continue with the question of integration by showing how the lateral input can form a map compatible with the retinotopic map to be integrated in a multimodal representation in the optic tectum. Finally, chapter 7, is an in depth discussion of the results presented in this thesis.

Thank you

Many people have been of help during my time at the *Physik Department*. First I would like to thank Prof. J. Leo van Hemmen, my thesis supervisor. His love and motivation for physics and neuroscience are most impressive. He convinced me to come to Munich and do my doctoral studies here, in this wonderful city. Scientifically, I also have a great debt to Prof. Pierre Depommier from the Université de Montréal. He encouraged me to undertake a scientific career, and his knowledge of sciences and culture helped me to find my place in the sciences.

I also want to thank my biological collaborator: Prof. Jacob Engelmann, a good neurophysiologist. The collaboration with him was beneficial (and I hope will last). In a more general way, I want to thank Prof. Horst Bleckmann, who invited me to visit his laboratory in Bonn and supported this collaboration with people from his laboratory.

Writing this thesis would not have been possible without all my colleagues at the "T35" chair. In particular, Christine Vossen and Maria Suttner, who shared (for a time) an office with me. I also want to thank the Bernstein Center for Computational-Neuroscience Munich for funding (Dr Isolde von Bülow, Dr Dagmar Bergmann-Erb).

I have had the opportunity to learn many things in Munich. I am grateful to the Studentinnenheim Theresianum where I passed four wonderful year (Ms Emanuela Romero and Maria Conception Baqué), the KHG Leopoldstrasse 11, my zen meditation group (P. Dr Stefan Bauberger SJ). In particular, the contact with Stefan Bauberger (also a physicist) really influenced my vision of the world as a physical and spiritual entity. I want to thank,all the people I met during this adventure of writing a PhD in the Bavarian capital. Many are really special to me, some of them became really good friends (Zoé, Christine, Kerstin, Jörg, Dominik, etc.). A special thanks also to Prof. J. Leo van Hemmen, Mr Klaus Hardtke, Prof. Jacob Engelmann and Dr Moritz Franosch for careful editing.

Preface

Finally, I want to thank my father, Dr Ronald Goulet, to whom I dedicate this thesis. He shared with me a love for science in general and computational neuroscience in particular. He has been a major source of support psychologically personally, scientifically and financially during all my life and particularly during my studies.

Munich, January 2010

Contents

Contents

Contents

1. Function, Anatomy and Physiology

This chapter discusses the function, anatomy and physiology of the lateral-line both at the periphery and in the brain. It should give the reader enough biological understanding to follow the rest of the physical argumentation in the thesis.

As in all vertebrates, the most important function of the central nervous system of fishes is the coordination of interactions between the animal and its environment. These interactions are brought about by muscles (controlling the response of the animal to its environment) and sense organs (controlling the information available for the animal about its environment), which are connected with the central nervous system by cranial and spinal nerves. Thus, an understanding of the peripheral motor and sensory systems of fishes is necessary for a proper evaluation of the structure and function of brain centers.

Like other vertebrates, fishes are equipped with olfactory, visual, acoustic, vestibular, gustatory and somatosensory sense organs to receive signals from the environment. In addition, they have a lateral line system to sense water currents and pressure, while some groups have specialized electrosensory lateral line organs. The organization of all these sensory systems has been reviewed in some detail in the book by Atema et al [7]. This thesis deals with information processing at the afferents and in the brain for the *lateral-line* system of fishes.

Many aquatic vertebrates possess a mechano-sensory lateral system. It has often been described as a system enabling an animal to *feel at a distance* by *detecting* and

1

analyzing water motion on their skin. The first one to write a review on the topic was Sven Dijkgraaf [42]. For more modern reviews on the topic, one can consult [10, 32].

The lateral-line system plays a role in a variety of behaviors. The lateral-line system contributes in prey capture [88, 109], predator avoidance, object recognition [17], communication [127], schooling behavior [117] and rheotaxis [88, 102, 132].

1.1 Anatomy and Physiology of Detectors

The sensory units of the lateral line (see Fig. 1.1) are the neuromasts [113]. In fish, one can find two types of neuromasts: superficial neuromasts (SN) located on the surface of the skin and,canal neuromasts (CN) situated in sub-dermal fluid-filled canals that are connected to the outside medium by pores [10, 35, 106, 122]. In the latter there is typically one neuromast between two adjacent canal pores [46, 122, 141]. CNs are orientated parallel to the length axis of the respective canal [46]. Most SNs are orientated either parallel or orthogonal to the body axis [35, 46].

Neuromasts are composed of hair cells. A single neuromast may contain up to several hundred hair cells (we refer the reader to Fig. 1.2 and the next subsection). The ciliary bundles of the hair cells are embedded in a gelatinous cupula that extends into the surrounding water or into the canal fluid [51, 86]. The sensory epithelium of a lateral-line neuromast contains two populations of antagonistically orientated hair cells [52].

1.1.1 Hair Cells

Hair cells are known as the primary transducer cells in hearing. In the hearing system, hair cells are located in four inner hair organs: the semicircular canals, the utricle, the saccule and the cochlea of higher vertebrates [44]. Hair cells are also the organ that detects the mechanical vibration of the medium in the lateral-line system [91] see Fig. 1.2. A typical hair cell consists of a body and some cilia and a single kinocilium protruding from the apical surface of the body, known as the hair bundle. As shown in Fig. 1.2, the cilia are arranged in such a way that they increase in length towards the kinocilium. Thereby the morphology of each hair-cell is polarized with regard to the kinocilium.

Individual cilia are connected to each other by so-called lateral and tip links. The tip links are thought to be important for the sensory function of the hair cell, as they are generally considered to directly activate the Ca^{2+} sensitive mechano-transducer channels [80], which are situated near the tips of the stereocilia [41, 81]. The
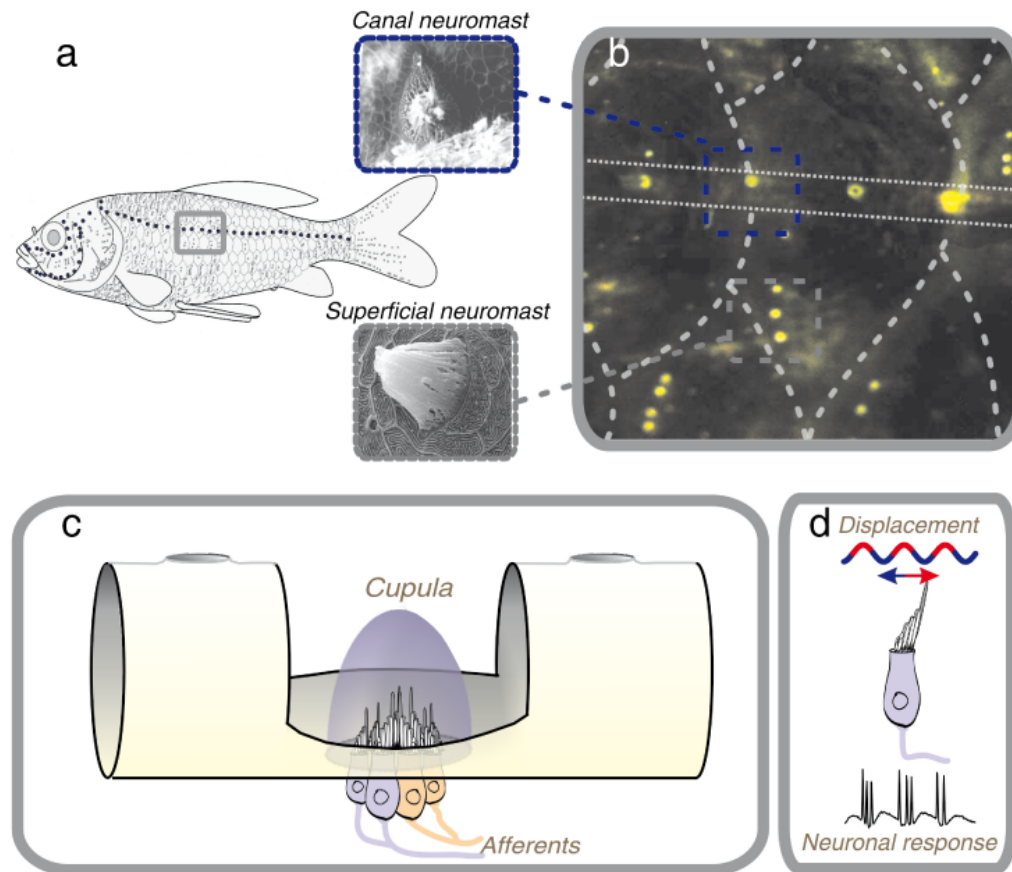
Figure 1.1: *Organization of canal and peripheral lateral-line system.* **a** *The distribution of canal pores (small black disks) and superficial neuromasts (grey dots) in goldfish (Carassius auratus); fish picture modified after A. Grotefeld.* **b** *Close-ups of SNs and CNs situated on the trunk of a goldfish. Neuromasts (light dots) are marked by the fluorescent dye DASPEI. The insets show SEM images of a single SN with cupula and a single CN.* **c** *Schematic of a CN embedded in the surrounding canal. The cupula and the two separately innervated populations of hair cells of opposite polarity are sensitive to either water moving from left to right or in the opposite direction.* **d** *Schematic of a sinusoidal stimulus used in physiological experiments and its impact on a single hair cell.*
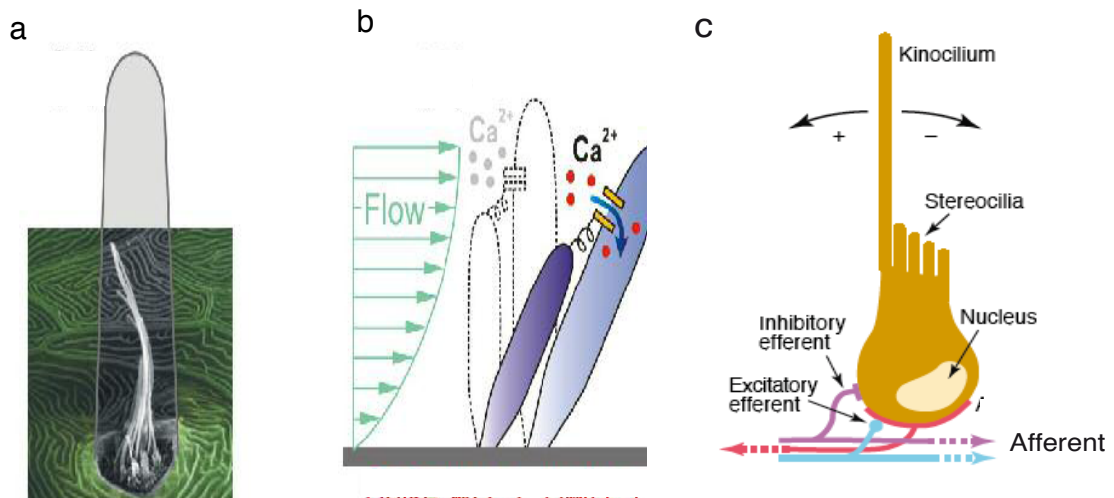
Figure 1.2: *Cupula and function of hair cells.* **a** *Superposition of a scanning electron micrograph and a drawn oval basal shape jointly demonstrating a neuromast on the skin surface of a zebrafish. The scanning electron micrograph shows the ciliary bundles of the neuromast with the cupula removed. The grayish oval basal shape schematically illustrates the gelatinous cupula that encapsulates the ciliary bundles.* **b** *Diagram illustrating the transduction mechanism of a hair cell underlying a ciliary bundle in a neuromast. Two neighboring stereocilia with different heights in the same ciliary bundle are interconnected by a tip link. The bending or sliding of the encapsulating cupula (not shown) under water flow results in the deflection of the stereocilia and causes the tip link to open nanopores. The resulting ionic flow leads to an excitatory receptor potential and stimulates neuron spiking [**a** and **b** are modified after Yingchen Yang].* **c** *Scheme of a hair cell, illustrating its functional asymmetry, as well as its afferent and efferent innervation. The implication that excitatory efferents act on the afferent fiber rather than directly on the hair cell is plausible but has not been demonstrated yet, picture modified after [64].*

mechanical vibration of the medium surrounding the hair cells coupled to the hair bundle forces it to pivot at its base. This process transmits tension to the mechano-transducer channels via the tip links. The probability of the mechanotransducer channel being in an open state increases if the hair bundle is displaced in the excitatory direction, which is in the direction from the lowest stereocilia to the kinocilium. The overall stiffness of the hair bundle is the sum of the passive pivotal stiffness of the stereocilia and the stiffness of lateral links and tip links. The latter stiffness depends on the conformational state of the transducer channels. When the cell is stimulated in the other direction, it will reduce the probability of the mechano-transducer channel being in an open state.

1.1.2   Mechanics of the Cupula

Lateral line cupulae can be seen as displacement sensitive devices. A water motion induced displacement of the cupula results in a shearing of the hair bundles that leads to a change of the hair cell resting potential. Displacement of the ciliary bundle toward the kinocilium causes a depolarization, displacement in the opposite direction a hyperpolarization of the hair cells [91]. The hair cells in a cupula are orientated such a way that the excitation direction of the hair bundle is either parallel or anti-parallel to the largest axis of the cupula. Thus, displacement of the cupula leads to an increase in discharge rates in the fibers innervating one population of hair cells and to a decrease in discharge for the hair cells sensitive to motion in the *opposite* direction. In each neuromast, there will be one population of hair cells whose open probability increases when the cupula is displaced from head to tail and a second population whose open probability increases for displacements in the opposite direction. This has also been demonstrated in early studies of extra-cellular potentials, generated by the hair cells [53, 84].

It has been shown, that the frequency-selective properties of the lateral line are predominantly determined by hydrodynamic forces and mechanical properties of the neuromast, not by individual hair cell tuning [91]. For a discussion of the mechanics of the cupula the reader is referred to [108]. In practice, this means that the water around the fish will deform the cupula. It was shown that the mean firing rate of SN will increase in a constant flow, whereas the mean firing rate of CN will stay stable due to the fact that CNs respond to the water velocity *in* the canal (i.e., the pressure gradient between two adjacent pores, see [46, 47], and section 3.1.2). Therefore, classically, SNs have been understood as velocity detectors, whereas CNs (sensitive to the water motion *in* the canal) have been understood as *acceleration* detectors; see chapter 3 and Fig. 1.1. Clarifying the issue of *what* encodes the lateral line neuromast is a major issue of the present dissertation. My work will be based on an analytical study of the water motion and comparisons with electrophysiological measurements.

1.2   Anatomy and Physiology of the Afferent Nerves

Based on the possession of separate ganglia and distinct areas of peripheral innervation, information of the peripheral lateral line enters the medulla through at least three pairs of lateral line nerves. These are the dorsal and ventral anterior lateral line nerves (ALLN) which carry information of lateral line neuromasts situated on the head, and the posterior lateral line nerves (PLLN) which carry information of neuromasts situated on the trunk [113, 114]. On some species, one or more additional nerves have been reported [10].

At the nerve level, the information between canal and superficial neuromasts is carried by different fibers [50, 104, 105, 107]. Developmental studies on the zebrafish (*Danio rerio*) and tracing studies in goldfish *carassius auratus* [92] show that the afferents project to the medulla in a crude somatotopic manner. The position of the neuromasts along the antero posterior axis (from head to tail) of the fish is represented in the central projection of the afferents [3, 64]. There is also evidence that fibers innervate hair cells of, on average two and up to five, consecutive neuromasts. When an afferent innervates more than one neuromast, the innervated neuromasts are nearly always consecutive, as expected if somatotopy is encoded in the system [107]. The fibers innervate *exclusively* hair cells of the same polarity [50, 107]. It is still unclear if the information of differently tuned hair-cells is maintained in the projection pattern of the afferent i.e., if the orientation selectivity is maintained. However, maintaining this information would be beneficial for computational tasks like determining flow directions.

1.3   Central Processing of the Lateral Line Projection

Little is known about the central physiology of hydrodynamic stimuli in fishes [7, 10, 12, 13, 16, 32]. Here, we try to summarize the knowledge of anatomy and physiology of the lateral-line system for fish, most of the data coming from trout or goldfish. However, due to the great variety of species, a great variability in brain structures and sensory systems can be found [16, 112]. Variations in the organization of the brain of fishes are closely related with functional specializations. In this dissertation, I will try to produce a minimal model in order to understand some *general principles* of information processing in the lateral-line system of fishes.

For a general review of the brain of fishes, one can consult [16, 103, 111, 112] and Fig. 1.3 a. The brain of vertebrates is composed of two symmetric hemispheres. From an embryonal point of view, one can first distinguish two main structures: the *rhobencephalon* (hindbrain) and the *prosencephalon*. The prosencephalon later divide in two substructures, namely the *diencephalon* (middle brain) and the *telencephalon* (forebrain). The rhobencephalon will later divides in three substructures namely the *myencephalon* the *metencephalon* and the *mesencephalon*. The rhobencephalon without the cerebellum (a structure of the metencephalon) is known as the *brainstem* [103].

1.3.1   Central Projection of the Lateral-Line System

Lateral-line information is processed at all levels of the brain from the metencephalon up to telencephalon (for review [11, 16] and Fig. 1.3 a & b). Roots of the lateral-line nerves enter the ipsilateral brainstem and bifurcate into ascending and descending

branches which terminate in the medial octavolateralis nucleus (MON) [11, 23, 100, 135]. It should be mentioned that some primary lateral line projections always reach the ipsilateral cerebellar granular eminence [11, 100, 135], and in a few species, the corpus and valvular cerebelli [11, 23]. The functional significance of these projections is not known, but they can be involved in the formation of a central representation of expected stimuli [11]. Up to now, there is no evidence of recurrent connectivity within the MON (Engelmann, private communication).

The second-order projections from the MON ascend in the lateral longitudinal fascicle and terminate bilaterally (with the contralateral projection being stronger) on the lateral portion of the torus semicirularis and from where they project to the deep layers of the optic tectum. Additionally, the second-order neurones of MON also project to the contralateral MON and have a weak direct projection to the tectum opticum. There are also lateral-line projections to various diencephalic nuclei and to the forebrain [11, 100] and a prominent feed-back loop from the torus semicircularis to the MON and from the tectum opticum to the torus semicircularis. The feedback from the tectum opticum to the torus semi-circularis is believed to be at least in part inhibitory [139].

1.3.2 Lateral-Line Maps

Several anatomical, behavioral and physiological studies have demonstrated the existence of central lateral-line maps [11]. As I discussed earlier for bony fish, the primary afferents project in a double somatotopic way (the afferent *and* the cells they project to present both a somatotopic organization) [3, 11, 100, 135]. There is also behavioral evidence that Mottled Sculpin can position their snout near where a hydrodynamic stimulus occurs along their trunk. That show that the information about position of the lateral-line detectors on the body is preserved.

Some studies also point out the existence of a crude somatotopic organization in the MON of some fishes [11, 135]. There is evidence that toral cells receiving input from flow insensitive MON cells map the position of a sphere into a somatotopic map [45, 119]. In this thesis, I will show by means of simulation that the previous study data demonstrate that both flow insensitive and flow sensitive toral neurons encoded the water motion (velocity for the flow sensitive and the pressure gradient, not the position of the object) on the skin of the fish in a somatotopic and directional way. There is evidence that, at least in part, CNs and SNs map separately [45, 119].

Computed lateral-line maps of water wave direction in the tectum of the clawed frog *Xenopus laevis* [145] and of the Axolotl *Ambystoma mexicanum* [8] exist. For the clawed frog a minimal model shows how the direction of the water waves can be encoded to form a spatial map [57] and an extension of this model shows how
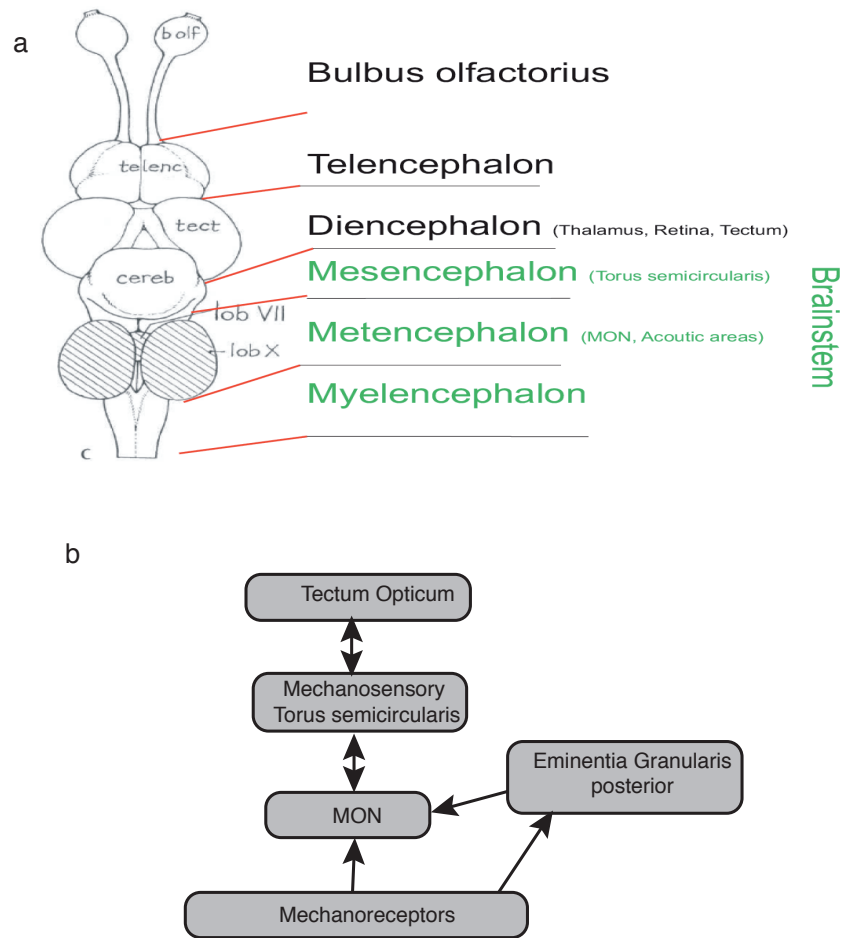
Figure 1.3: **a** *Sketch of the dorsal view of the brain of a teleostean fish.The brain of vertebrates is composed of two symmetric hemispheres. The brainstem is composed of several sub-structures: the myelencephalon, metencephalon and the mesencephalon. The brainstem with the cerebellum is know as the rhobencephalon. The prosencephalon is composed of the diencephalon and the telencephalon. Lateral-line information is processed at all levels from metencephalon to telencephalon [image from Jacob Engelmann modified from [112]]. **b** Schematic view of the projection of the lateral-line in the brain of teleostean. The mechanoreceptors project by mean of at least three different nerves in the medial octavolateralis nucleus (MON) in the metencephalon. Some afferents also terminate in the Eminentia Granularis posterior. The cell of the MON will project bi-directionally to the lateral portion of the torus semicircularis and also bi-directionally into the deep layer of the tectum opticum. Lateral-line information will also be processed from the torus and the tectum opticum to higher brain areas, (picture redrawn from a sketch of Jacob Engelmann).*

Xenopus can compute this map using a STDP learning rule and a visual teacher [55].

For fish, the cells in the MON answer only to lateral-line stimulus. I n the torus semi-circularis some cells may also respond to an auditory stimulus [11]. In the optic tectum, the cells are multimodal responding to visual, mechanosensory, auditory and visual stimuli [9]. The projection between torus and optic tectum are topographically matched [138, 139]. This means that the lateral-line map in the torus and the multi-modal map in the optic tectum should have an organization compatible with each other.

2. Hydrodynamics of the Stimulus

In this chapter, we provide a detailed theoretical, i.e., mathematical, analysis of the biophysics of fish lateral-line detection.

A key motivation leading to this doctoral dissertation was to improve our general understanding of the biological physics governing the *interaction* between the lateral-line system and the water surrounding it by applying and solving the Navier-Stokes equation and in this way clarifying the mechanisms underlying the ensuing neuronal processing. We also vindicate the assumption that the Euler equation, although neglecting viscosity, is a valid starting point and, hence, we justify the approach of numerous preceding works in this field [33, 38, 56, 71, 126], as discussed below.

The lateral line functions in a rather complex context with many different physical factors, and the environment can be really noisy. All these factors must be analyzed separately, considering also the behavioral contexts, in order to understand the underlying neuronal mechanisms involved in processing the information and generating the behavioral responses observed. In addition, we consider the boundary layer, a thin layer of fluid around any moving object where viscosity is essential. The behavior of this layer can be described by the Navier-Stokes equation. Although the Euler equation does not take fluid viscosity into account, it nevertheless effectively justifies a simple description of the stimulus once the boundary layer has been "added" to the fish body Having elucidated the underlying physics, we incorporate these facets into our model.

Based on our analysis of the fundamental stimulus properties we present a detailed investigation of the responses of lateral-line receptors within and outside the canals, the latter being the superficial neuromasts (SN), and reveal strong similarities between the two. We then compare modeling results and neuronal data.

2.1 Equations of Motion

The major difference between classical mechanics for particles and fluid dynamics is that in fluid dynamics the equation of motion considers the rate of change of a continuous medium rather than the motion of discrete particles in an empty space. One major consequence of this approximation is that even if the velocity is constant at a certain point in space the velocity of one single particle moving in the fluid can change in time i.e. the acceleration of this particle does not vanish. For textbooks about fluid mechanics please consult [2, 95]. Here, we follow the proof given by Chorin [22] in section 1.3.

The usual way of describing a fluid motion in 3D space is a system of equations of the form $\boldsymbol{v}\,(x,y,z,t) = \{u(x,y,z,t), v(x,y,z,t), w(x,y,z,t)\}$, where u,v,w are the spatial components of the fluid motion, x,y,z are the spatial coordinates and t is the time. To describe the motion of fluids in 3D you then need a system of three equations $\{u,v,w\}$ and four variables (x,y,z,t). Applying the chain rule, one can easily find that the acceleration of the fluid at a certain position (x,y,z) is

$$\frac{\mathrm{D}\boldsymbol{v}}{\mathrm{D}t} = \frac{\partial \boldsymbol{v}}{\partial t} + (\boldsymbol{v}\,\cdot\nabla)\boldsymbol{v}\ . \tag{2.1}$$

An ideal fluid is defined as a fluid in which forces across a surface are normal to that surface (no diffusion on the surface). In this case the only acting force is called the *pressure*. For an ideal fluid, we can express the force acting on the surface of the fluid per unit of area as $F = p(x,y,t) \cdot \boldsymbol{n}$, where $p(x,y,t)$ is the pressure and $\boldsymbol{n}$ is normal to the surface. This assumption is not valid for a real fluid, since faster molecules from above a surface will diffuse across the surface to slow down the fluid above a surface. Therefore we have to change our definition and assume that the force per unit of area on the surface will be of the form $F = p(x,y,t)\boldsymbol{n}\,+\boldsymbol{\sigma}\,(x,t)\boldsymbol{n}$. Newton's second law states that the *rate* of change of momentum for any moving portion of the fluid $\mathcal{V}$ equals the force acting on its surface $\partial\mathcal{V}$ (balance of momentum)

$$\frac{d}{dt}\int_{\mathcal{V}} \rho\boldsymbol{v}\ dV = -\int_{\partial\mathcal{V}} (p\cdot\boldsymbol{n}\,+\boldsymbol{\sigma}\,\cdot\boldsymbol{n}\,)dS\,. \tag{2.2}$$

We should choose σ in such a way that it approximates the transport of momentum due to *molecular motion.* The fact that force acting on the surface is a linear function of the normal $\boldsymbol{n}$ is not an assumption, but can be proven (Cauchy Theorem, [2]). In order to do so, we make the two following assumptions:

- The fluid is newtonian. That means that $\boldsymbol{\sigma}$ depends only on the velocity gradients $\nabla\boldsymbol{u}$ and is proportional to them.

- Under rigid body rotations and translations $\boldsymbol{\sigma}$ is invariant. This is reasonable, since when a fluid undergoes a rigid body rotation, there should be no diffusion of momentum.

From the balance of angular momentum, one can deduce that $\boldsymbol{\sigma}$ is symmetric $(\sigma = \sigma^T)$. Since $\boldsymbol{\sigma}$ is symmetric it can only come from the symmetric part of $\nabla\boldsymbol{v}$ that is the deformation tensor $\boldsymbol{D} = 1/2[\nabla\boldsymbol{u} + (\nabla\boldsymbol{u})^T]$. It does not come from the rigid rotation of the fluid.

Since $\boldsymbol{\sigma}$ is a linear function of $\boldsymbol{D}$, the two matrices commute. Thus, the eigenvalues of $\boldsymbol{\sigma}$ can be expressed as linear combinations of those of $\boldsymbol{D}$. This implies that the eigenvalues must be linear and symmetric since we can always choose an orthogonal matrix $\boldsymbol{U}$ to permute two eigenvalues of $\boldsymbol{D}$ (by rotating through an angle π about an eigenvector) and this must permute the corresponding eigenvalue of $\boldsymbol{\sigma}$. The only linear functions that are symmetric in this sense are of the form

$$\boldsymbol{\sigma}_i = \lambda(d_1 + d_2 + d_3) + \mu d_i \qquad i = 1, 2, 3\,, \tag{2.3}$$

where σ_i are the eigenvalues of $\boldsymbol{\sigma}$ and d_i those of $\boldsymbol{D}$. This defines the constants λ and μ. The trace of $\boldsymbol{D}$ is equal to $\nabla\cdot\boldsymbol{v}$. For proof of that statement see for instance [22] p.21. We can then use the fact that the matrix $\boldsymbol{\sigma}$ is invariant under rigid body translation and rotation to transform σ_i back to the usual basis and deduce that

$$\boldsymbol{\sigma} = 2\mu[\boldsymbol{D} - \nabla\cdot\boldsymbol{v}\,\boldsymbol{I}] + \xi(\nabla\cdot\boldsymbol{v})\boldsymbol{I} \tag{2.4}$$

where μ is the *first coefficient of viscosity* and $\xi = \lambda + 1/3\mu$ is the *second coefficient of viscosity.*

Applying the transport and the divergence theorem on the balance of momentum (2.2), and using (2.1) we find

$$\rho\frac{\partial\boldsymbol{v}}{\partial t} + \rho(\boldsymbol{v}\cdot\nabla)\boldsymbol{v} = -\nabla p + (\lambda+\mu)\nabla(\nabla\cdot\boldsymbol{v}) + \mu\cdot\Delta\boldsymbol{v} + \rho\boldsymbol{g} \tag{2.5}$$

The Navier-Stokes equation for the case of an incompressible Newtonian fluid (ρ is constant) is

$$\frac{\partial\boldsymbol{v}}{\partial t} + (\boldsymbol{v}\cdot\nabla)\boldsymbol{v} = -\nabla p' + \nu\cdot\Delta\boldsymbol{v} + \boldsymbol{g} \qquad \text{with} \qquad \nabla\cdot\boldsymbol{v} = 0 \tag{2.6}$$

where $\nu = \mu/\rho$ and $p' = p/\rho$. The boundary condition of (2.6) demands that $\boldsymbol{v}$ vanishes on solid boundaries taking into account the friction between the fluid and the wall.

We shall then discuss some scaling properties with the aim of introducing a parameter (the Reynolds number) that measures the effect of viscosity on the flow. In any flow we can define L to be a characteristic length and V a characteristic velocity. These numbers are chosen in a somewhat arbitrary way. For example, if we consider the flow passing a sphere, L could be either the radius or the diameter of a sphere and V the velocity at infinity. Their choice determines a time scale scale $T = L/V$. The other quantity can also be expressed dimensionless $\boldsymbol{v}' = \boldsymbol{v}/V$, $x' = x/L$ and $t' = t/T$. The incompressible Navier-Stokes equation (2.6) in dimensionless variables takes the form of

$$\frac{\partial \boldsymbol{v}'}{\partial t'} + (\boldsymbol{v}' \cdot \nabla')\boldsymbol{v}' = -\nabla p'' + \frac{\nu}{LV}\Delta'\boldsymbol{v}' \qquad \text{with} \qquad \nabla \cdot \boldsymbol{v}' = 0 \,. \qquad (2.7)$$

where $p'' = p/(\rho V^2)$. We define the *Reynolds number* as

$$Re = \frac{LV}{\nu} \,. \qquad (2.8)$$

Two flows that have the same geometry besides scaling and the same Reynolds number are said to be *similar*. The solution for one is a suitable (rescaled) solution for the second.

In the case of an incompressible fluid of small viscosity apart from obstacles the things are easier. The Navier-Stokes equation (2.6) can be reduced formally to the Euler equation,

$$\frac{\partial \boldsymbol{v}}{\partial t} + (\boldsymbol{v} \cdot \nabla)\boldsymbol{v} = -\frac{\nabla p}{\rho} + \boldsymbol{g} \qquad \text{with} \qquad \nabla \cdot \boldsymbol{v} = 0 \,, \qquad (2.9)$$

where the velocity gradient orthogonal to the direction of motion is negligible and therefore makes the pressure the only effective surface force. The boundary condition of the Navier-Stokes equation (2.6) demands that $\boldsymbol{v}$ vanishes on solid boundaries taking into account the friction between fluid and wall, whereas for the Euler equation (2.9) it only required that fluid motion is effectively bounded by the wall.

2.2 Boundary Layers

Fluids of low viscosity, therefore, show two types of behavior. Far away from obstacles the shear forces vanish and therefore the dynamics of the fluid is well described by the Euler equation (2.9). The second behavior is in a thin layer of fluid around

the object. In this *boundary layer*, the fluid velocity decreases rapidly to zero and $\mu \cdot \Delta \boldsymbol{v}$ is not negligible. Therefore, one needs to solve the Navier-Stokes equation (2.6). Even if the flow outside the boundary layer is laminar, the flow within the boundary layer can be either laminar or turbulent. The boundary-layer is usually defined as the zone where the velocity goes from 0 to 99% of its value without the obstacle. For information about boundary layer theory in general, please consult chapter 6 of [2], [95, §371] and [128].

The dynamics within the boundary is governed by the Reynolds number. Flow within the boundary layer around a flat plane is laminar up to a Reynolds number of about $Re = 3.2 \cdot 10^5$. Above this value the water motion undergoes a transition and becomes turbulent. The transition from laminar to turbulent causes a significant increase in the thickness of the boundary layer because of changes in the proportional relation. The thickness of a boundary layer for a laminar flow can be approximated by $\delta / L \simeq 5 / \sqrt{Re_{\mathrm{L}}}$ and for turbulent flow by $\delta / L \simeq 0.37 \cdot Re_L^{-1/5}$. In our case, however, the boundary layer is thin as compared to the characteristic length (L). For a theoretical explanation of this increase in the thickness of the boundary layer in the transition between laminar and turbulent flow, the reader is refer to [128] section 18.2.5.

In addition, the transition from laminar to turbulent is connected with a shift of the separation point. In turbulent boundary layers the separation occurs much further downstream, which, despite the larger thickness of the boundary layer, entails a reduction of friction resistance due to the smaller dead water area. Streamlined bodies, however, often show no separation at all, since the modest pressure slope behind the point of maximum body cross section can be overcome by the boundary layer without separation, but only if the flow in the boundary layer is turbulent. Experimental results have shown no boundary layer separation on fish bodies. The Reynolds numbers on the fish body surface range from $Re = 10^3$ to $Re = 10^5$, thus including both laminar and turbulent current regimes. [1] [4].

2.2.1 Neuromasts as Lateral-line Detectors

Since the stimulus of the lateral-line detectors is the water velocity on the skin of fish (for SN) or the pressure difference between two adjacent pores on the skin of the fish (for CN), the boundary layer around the fish is likely to play a role, and we have to verify it. For CN, we will show in the next subsection that the pressure within a boundary layer is constant and, therefore, we can calculate it neglecting the presence of the boundary layer. The case of SN is a bit more tricky. Simulations

---

[1]   The indicated Reynolds numbers actually are below the critical value. Yet, for rough fish surfaces and non trouble-free incident flow, turbulence can also occur for these values.
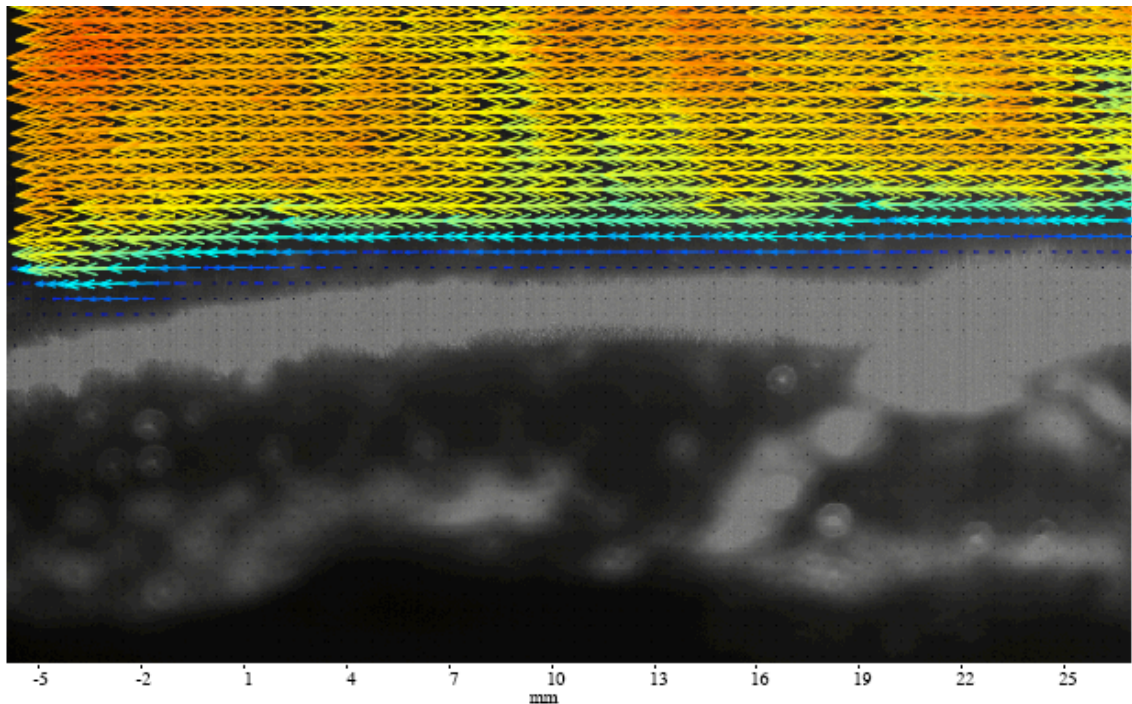
Figure 2.1: *Measurement of the water flow using PIV (particle image velocimetry) in the boundary layer around a model fish (black) in a 10cm/s flow. The vector plot represents the direction of the water motion around the fish and the color its intensity. In this picture, the boundary layer is the part where the color changes rapidly from orange/yellow to blue. The boundary layer has a thickness of about 3 mm (picture due to Boris Chagnaud).*

show that the turbulence induced by the convection term is not likely to affect the form of a dipole stimulus. Moreover, we will show that the experimental firing rate at the afferent nerves of the detectors is highly predictable by a potential formulation obtained from the Euler equation. In the next chapter, we will also show evidence that SNs encode even white noise on a really reproducible way.

2.2.2 Pressure within a Boundary Layer

Canal neuromasts are stimulated by pressure differences between pores at the surface of the skin of fish. In order to be able to use the Euler equation to calculate the pressure around a body (stating that pressure inside the boundary layer is equal to the pressure outside), we have to show that the pressure is constant within the boundary layer. In the following subsection, we will show that the pressure is

constant in the boundary layer around a plate for a laminar flow, then show the same for a turbulent flow and finally we will generalize this result for a curve surface. We exclude boundary layer separation from our analysis.

Pressure above a Plane for a Laminar Boundary Layer
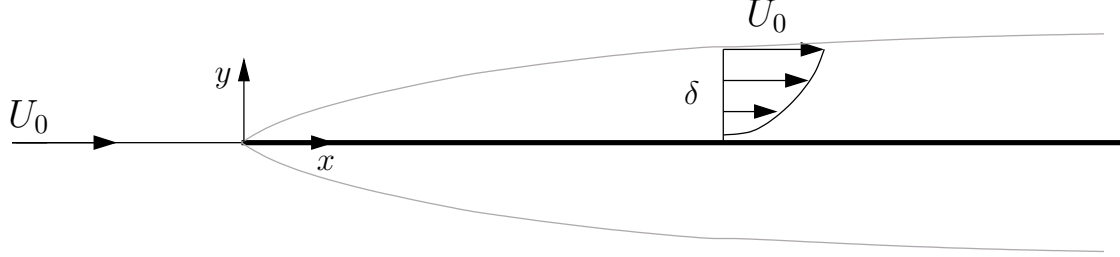
Figure 2.2: *Flow past a solid plane. We can see here, the velocity given by U_0 outside the boundary layer rapidly decreases towards the surface where $\boldsymbol{v} = 0$. The thickness of the boundary layer δ increases with increasing disc length L(not shown) in the $\boldsymbol{x}$ direction.*

Figure 2.2 shows the physical situation we want to analyze here, namely the effect of the boundary layer on the flow around a plane surface. The Navier-Stokes equation and the condition of incompressibility is reductable in the 2D case (with $\nu = \mu/\rho$) to

$$
\begin{aligned}
u\frac{\partial u}{\partial x} + v\frac{\partial u}{\partial y} &= -\frac{1}{\rho}\frac{\partial p}{\partial x} + \nu\left(\frac{\partial^2 u}{\partial x^2} + \frac{\partial^2 u}{\partial y^2}\right) \\
u\frac{\partial v}{\partial x} + v\frac{\partial v}{\partial y} &= -\frac{1}{\rho}\frac{\partial p}{\partial y} + \nu\left(\frac{\partial^2 v}{\partial x^2} + \frac{\partial^2 v}{\partial y^2}\right)
\end{aligned}
\tag{2.10}
$$

$$
\frac{\partial u}{\partial x} + \frac{\partial v}{\partial y} = 0
\tag{2.11}
$$

where u and v are the velocity components in the x- and the y-direction. Within the boundary layer u varies much stronger in the y-direction than in the x-direction. Within the boundary layer, we can therefore write

$$
\left|\frac{\partial u}{\partial y}\right| \gg \left|\frac{\partial u}{\partial x}\right|.
\tag{2.12}
$$

Moreover, using (2.11) we obtain:

$$
\left|\frac{\partial u}{\partial y}\right| \gg \left|\frac{\partial v}{\partial y}\right|
\tag{2.13}
$$

A scaling argument follows. Assuming that L is the length of the plate and δ the thickness of the boundary layer which is much smaller than L and the magnitude of u is U_0, we can then estimate the terms of (2.12) by: $U_0/\delta \gg U_0/L$.

As the vertical velocity v must vanish at $y = 0$ using (2.12) we can consequently estimate the magnitude of v by $U_0\delta/L$. All derivatives of the velocity components with respect to x and y can now be obtained by dividing by L or δ respectively [128]. From this one derives:

$$
\begin{aligned}
\frac{1}{\rho}\frac{\partial p}{\partial x} &= \mathcal{O}\left\{\nu\left(\frac{U_0}{L^2} + \frac{U_0}{\delta^2}\right) - \frac{2U_0^2}{L}\right\} \\
\frac{1}{\rho}\frac{\partial p}{\partial y} &= \mathcal{O}\left\{\nu\left(\frac{U_0\delta}{L^3} + \frac{U_0}{L\delta}\right) - \frac{2U_0^2\delta}{L^2}\right\} = \mathcal{O}\left\{\frac{\delta}{L}\frac{1}{\rho}\frac{\delta p}{\delta x}\right\}
\end{aligned}
\tag{2.14}
$$

And therefore:

$$
\left|\frac{\partial p}{\partial x}\right| \gg \left|\frac{\partial p}{\partial y}\right| \qquad \text{or} \qquad \left|\frac{\partial p}{\partial y}\right| \approx 0 \,,
\tag{2.15}
$$

That means the pressure within the boundary layer changes in the x-direction, but can be regarded as constant and equal to the outside pressure perpendicular to it. Thus the performance of the canal lateral line system is not compromised by a stationary and laminar boundary layer.

Turbulent Boundary Layers

As can be demonstrated for a turbulent boundary layer, the mainstream field can be assumed to be laminar. In general, turbulent flow requires the description of chaotic fluctuations; liquid lumps irregularly drift off the laminar streamlines and produce vorticity and fluctuation.

This can be approached by separating the movement into its temporal mean value and a fluctuation part

$$
q = \bar{q} + q' \qquad \text{where} \qquad \overline{q'} = 0 \,.
\tag{2.16}
$$

The fundamental concept is that the fluctuations u', v', w' act on the average movement $\bar{u}, \bar{v}, \bar{w}$ like an additional shearing stress, so that the average movement exhibits an apparently higher viscosity [128]. Fluctuation is taken as large scale diffusion. The chaotic, turbulent behavior can subsequently be described by a slightly modified Navier-Stokes equation.

Inserting (2.16) in (2.10) yields, after time averaging and the use of continuity,

$$
\bar{u}\frac{\partial \bar{u}}{\partial x} + \bar{v}\frac{\partial \bar{u}}{\partial y} = -\frac{1}{\rho}\frac{\partial \bar{p}}{\partial x} + \nu\left(\frac{\partial^2 \bar{u}}{\partial x^2} + \frac{\partial^2 \bar{u}}{\partial y^2}\right) - \left(\underbrace{\frac{\partial \overline{u'^2}}{\partial x} + \frac{\partial \overline{u'v'}}{\partial y}}_{\text{Reynolds}}\right)
$$

$$
\bar{u}\frac{\partial \bar{v}}{\partial x} + \bar{v}\frac{\partial \bar{v}}{\partial y} = -\frac{1}{\rho}\frac{\partial \bar{p}}{\partial y} + \nu\left(\frac{\partial^2 \bar{v}}{\partial x^2} + \frac{\partial^2 \bar{v}}{\partial y^2}\right) - \left(\underbrace{\frac{\partial \overline{v'^2}}{\partial y} + \frac{\partial \overline{u'v'}}{\partial x}}_{\text{Reynolds}}\right).
$$

(2.17)

Fluctuation exclusively appears in the additional stress tensor; the apparent stresses are called Reynolds stresses.

The set of equations (2.17) has the same form as (2.10) and is subject to the same boundary layer conditions and assumptions. With the same scaling argument, the following is obtained

$$
-\frac{\partial \bar{p}}{\partial y} - \frac{\rho \overline{v'^2}}{\partial y} \simeq 0\,,
$$

(2.18)

Integration over the thickness of the boundary gives:

$$
\left[-\bar{p} - \rho\overline{v'^2}\right]_0^\delta = 0\,,
$$

(2.19)

As fluctuation must vanish on the surface and at the edge of the boundary layer, the following can be stated

$$
\bar{p}_{\text{Wall}} = p_{\text{boundary}}\,.
$$

(2.20)

That means on *average* the pressure inside the boundary layer is constant. These fluctuations probably add noises in the stimulation pattern on the fish body.

Curved Surfaces

For an axially symmetric body placed in a homogeneous, stationary flow along its axis, (Fig. 2.3) the general curvilinear coordinates α and β are introduced, taking into account each point of the body surface in the tangential and normal direction respectively.

Under this transformation, the two-dimensional Navier-Stokes equation takes the form
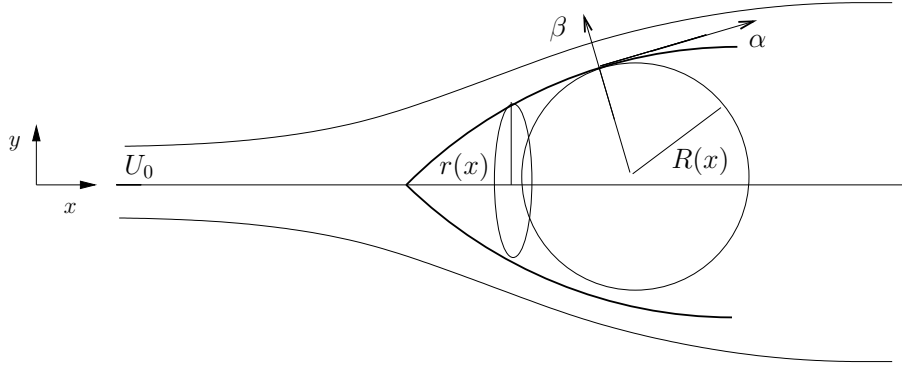
Figure 2.3: *Flow passing an axially symmetric body of cross section $r(x)$, described in a curvilinear coordinate system with α being the meridian length and β the distance from the body surface at each point. $R(x)$ is the radius of curvature. The (x, y) coordinate axes have been indicated on the left*

$$\frac{1}{1+\kappa\beta}u\frac{\partial u}{\partial\alpha} + v\frac{\partial u}{\partial\beta} + \frac{\kappa}{1+\kappa\beta}uv = -\frac{1}{\rho}\frac{1}{1+\kappa\beta}\frac{\partial p}{\partial\alpha} + \nu\left[\frac{1}{(1+\kappa\beta)^2}\frac{\partial^2 u}{\partial\alpha^2} + \frac{\partial^2 u}{\partial\beta^2}\right.$$
$$\left. -\frac{\beta}{(1+\kappa\beta)^3}\frac{\partial\kappa}{\partial\alpha}\frac{\partial u}{\partial\alpha} + \frac{\kappa}{1+\kappa\beta}\frac{\partial u}{\partial\beta} - \frac{\kappa^2}{(1+\kappa\beta)^2}u + \frac{1}{(1+\kappa\beta)^3}\frac{\partial\kappa}{\partial\alpha}v + \frac{2\kappa}{(1+\kappa\beta)^2}\frac{\partial v}{\partial\alpha}\right]$$

$$\frac{1}{1+\kappa\beta}u\frac{\partial v}{\partial\alpha} + v\frac{\partial v}{\partial\beta} - \frac{\kappa}{1+\kappa\beta}u^2 = -\frac{1}{\rho}\frac{\partial p}{\partial\beta} + \nu\left[\frac{1}{(1+\kappa\beta)^2}\frac{\partial^2 v}{\partial\alpha^2} + \frac{\partial^2 v}{\partial\beta^2}\right.$$
$$\left. -\frac{\beta}{(1+\kappa\beta)^3}\frac{\partial\kappa}{\partial\alpha}\frac{\partial v}{\partial\alpha} + \frac{\kappa}{1+\kappa\beta}\frac{\partial v}{\partial\beta} - \frac{\kappa^2}{(1+\kappa\beta)^2}v + \frac{1}{(1+\kappa\beta)^3}\frac{\partial\kappa}{\partial\alpha}u\right.$$
$$\left. + \frac{2\kappa}{(1+\kappa\beta)^2}\frac{\partial u}{\partial\alpha}\right]$$

$$(2.21)$$

κ denoting the inverse radius of curvature and u and v the velocity components in the transformed coordinate system [128]. Once more the boundary layer approximation process assumes small values for κ and $\partial\kappa/\partial\alpha$ so that the pressure gradient becomes

$$\frac{1}{\rho}\frac{\partial p}{\partial x} = \mathcal{O}\left\{\nu\frac{U_0}{\delta^2} - \frac{2U_0^2}{L}\right\}$$
$$\frac{1}{\rho}\frac{\partial p}{\partial y} = \mathcal{O}\left\{-\kappa U_0^2\right\}.$$

$$(2.22)$$

The variation of p in y-direction may again be neglected compared to the variation in x-direction; p is constant in a cross section of the boundary layer.

It has, therefore, been demonstrated that this assumption holds for all boundary layers, both laminar and turbulent independently of their geometrical shape. It follows that the pressure distribution at the edge of the boundary layer is equal to the pressure distribution on the fish body and can be taken as the stimulus input to the canal lateral-line system.

2.2.3 Velocity Field Within a Boundary Layer

Since SNs are stimulated by the velocity field on the skin of the fish, they are more likely to be affected by the presence of a boundary layer around the fish. The velocity of water decreases intensity around the fish within the boundary layer. What interests us here is how much the velocity profile (image) of the flow parallel to the fish body is affected by the boundary layer. For low Reynolds numbers, the flow within the boundary layer will be laminar. That means that the fluid flows in parallel layers with no disruption between the layers. In this case, the *shape* of the flow dragging the cupula (parallel to the wall) will decrease in intensity. However, its geometry parallel to the wall would not be affected.

In some conditions, however, the flow around a fish becomes *turbulent*. That means that the streamwise velocity is characterized by unsteady (changing with time) swirling flows inside the boundary layer. The external flow reacts to the edge of the boundary layer, just as it would to the physical surface of an object. So the boundary layer gives any object an "effective" shape which is usually slightly different from the physical shape. To make things more confusing, the boundary layer may lift off or *separate* from the body and create an effective shape really different from the physical shape. However, as we said earlier, flow separation has not been observed in the case of a swimming fish [4]. The most probable effect on the flow field of a turbulent boundary that does not separate will be to add some *noise* to the clarity of the hydrodynamics image available from the detectors.

In order to verify how *much* the flow profile is likely to be affected by the turbulences within the boundary layer, we have done simulations using Comsol (a numerical simulation software) simulating the Navier-Stokes equation (2.6) at 1 mm from the wall and compared the results with a calculation using the Euler equation (2.9). We were only interested in the water flow *parallel* to the boundary since the flow perpendicular to the boundary layer decreases fast within the boundary layer. Using the method of images to satisfy the boundary conditions of the Euler equation, one can show that in the presence of a plane wall, the fluid velocity near and parallel to the wall will double; see for example section 4.4 of [2] and section 3.1. In the case of a *viscous* fluid the boundary condition of the Navier-Stokes equation prescribes that the velocity field is to vanish at the wall. It shows that fluid velocity parallel to a wall is *almost* twice the velocity produced by the same stimulus without

a wall (Fig. 2.4). We therefore conclude that even within the boundary layer the flow *parallel* to the wall can be approximated by the Euler equation, so that we can neglect the effect of the boundary layer.

Here, we will not discuss why an oscillating sphere is a relevant stimulus to the lateral line (it will be done later in section 2.4). At this point, we just want to show to the reader, that even if the boundary layer adds some noise to the water velocity profile, it does not affect its shape. Later on, we will confirm this assumption showing that the firing pattern at the afferent nerves is well explained by the Euler equation (section 3.1.1) and that SN encoded even white noise reliably (chapter 4). Therefore, we will calculate the flow field outside the boundary layer and compare it with the activity of the detectors.

2.3 Outer Flow

Since the effect of viscosity is limited to the boundary layer, outside the boundary layer, we can treat flow as *inviscid* (i.e. frictionless) and irrotational (i.e the fluid particles are not rotating). Under these assumptions, a flow potential ϕ can satisfies the Laplace equation and Euler boundary conditions

$$\Delta\phi = 0 \quad \text{with} \quad \boldsymbol{v} = \nabla\phi \quad \text{and} \quad \left.\frac{\partial\phi}{\partial\boldsymbol{n}}\right|_{\partial\mathcal{B}} = 0. \quad (2.23)$$

The Laplace equation being linear, any superposition of harmonic functions is a solution to that same equation; for given boundaries, the problem can always be solved by a unique superposition. The vector field in (2.23) is also additive, but does not necessarily solve the Euler equation; it only applies to incompressible, non-rotational flow because, in this case, the Euler equation (2.9) can be written as a gradient equation

$$\rho\nabla\left(\frac{\partial\phi}{\partial t} + \frac{1}{2}(\nabla\phi)^2\right) = -\nabla p \quad (2.24)$$

and the free variable p will always adapt to the needs of the equation. Potentials and velocity fields are therefore additive, as opposed to pressure which can be computed by the Bernoulli equation (2.24).
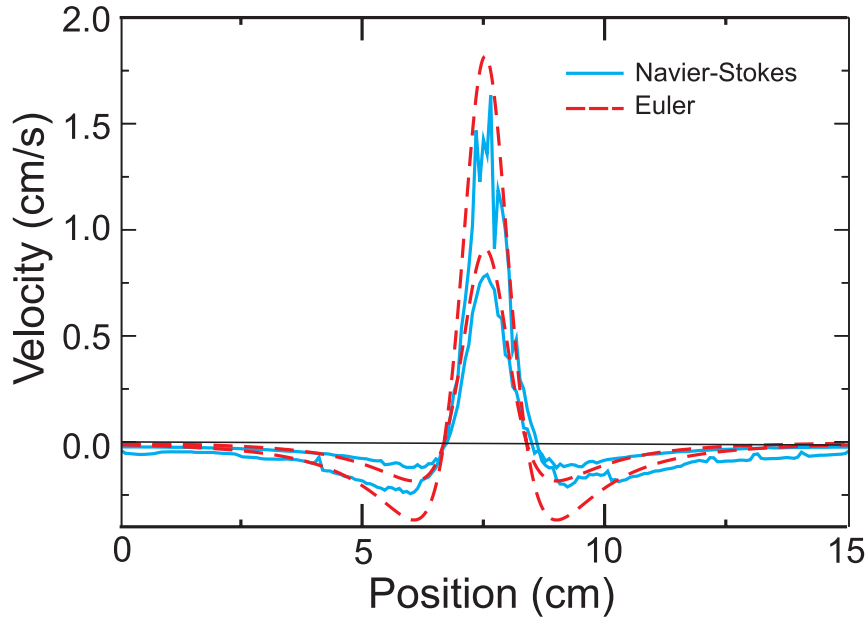
Figure 2.4: *Velocity field $\boldsymbol{v}$ parallel to the fish body (x) at 1 mm distance from the skin of the fish, modeled as a wall, for both the Navier-Stokes (solid line) and the Euler (dashed line) equation function of the position in x. The stimulus is a sphere oscillating in x-direction with frequency $f = 50$ Hz, sphere diameter $a = 5$ mm, and amplitude $s = 0.8$ mm at a distance of 1 cm from the wall (the two upper curves). The two lower curves are simulation results where the wall is missing. There are local fluctuations in the velocity field because of the viscosity of water, but the resulting dipole field has the same spatial characteristics as in the Euler case. The simulations show that the effect of the wall as predicted by the Euler equation (2.9), namely doubling the velocity, is also present in numerical simulations using the Navier-Stokes equation (2.6).*

2.4 Stimulus

An important question here is: What is a relevant stimulus to the fish lateral line? It seems that the lateral line is sensitive to all kinds of water motion: from water currents (in rheotaxis), to wakes (vortex ring) produced by other fish while swimming. The simplest stimulus is a small moving sphere that generates a so-called dipole flow field as defined in Lamb ([95, §92]). Any stimulus that can be written in the form of a potential can be expanded mathematically into a multipole series (linearity of the Laplace equation) consisting of a monopole, a dipole, a quadrupole and so forth [121].

The quadrupole and higher terms are negligible as they rapidly decrease with distance. The monopole term, if at all present, is a sound wave that is only relevant far away from a source, and exists only when there is a gain or lost of fluid in the environment i.e the monopole is a source or a sink alone. Thus, for the lateral line, the dipole is the most important stimulus, which is easily realized experimentally by a small vibrating or translating sphere (a doublet composed of a source and a sink together). A recent work showed that the information on the form of stimulus is also encoded in the water velocity field at the detectors up to about one body length of the stimulus away from the fish [131]. We will discuss the relevance of the form of the stimulus while discussing distance determination (section 5.7). We will also analyze the case of a translating sphere (section 3.2), a vortex ring (section 3.3) and white noise (chapter 4).

2.5 Effect of the Fish Body

In this section, the model developed by Hassan [74, 76] will be used to study how the perturbation due to the presence of the fish in water can influence the pressure on pores of the canal lateral-line system. This model is based on the method developed by Handelsman and Keller [68] to calculate the velocity potential of a slender body for an axially symmetrical potential. The method was generalized later for any finite potential by Geer [62].

The profile for the axially symmetric function representing the fish body can be written as

$$r = \epsilon R(z) \,. \tag{2.25}$$

where $R(z)$ is the body profile function with max $R(z) = 1$. As in [76], the function

representing the form of a fish is

$$R(z) = \sqrt{S(z)}, \tag{2.26}$$

$$S(z) = Kz(1-z)(1+q^2-z), \tag{2.27}$$

$$K = \frac{27\sqrt{(q^2-q+1)(q^2+q+1)}}{2+3q^2(1-q^2)+2(q^4+q^2+1)} - 6q^2. \tag{2.28}$$

In our case, the rapport between the maximum radius of the fish body and the length of the fish is $q = \frac{\epsilon}{2}$ and $\epsilon = 0.05$. The dorsal lateral line is a series of pores situated in the middle of the fish. In a cylindrical axis of reference, $\theta = \frac{\pi}{2}$, $r = \epsilon R(z)$ and z is the axis of the fish; the dorsal lateral line is taken as occupying the middle of the fish from $z = 0.3$ to $z = 0.8$, see Fig. 2.5.

2.5.1 Fish Body Within a Constant Flow

Hassan solved the case of a fish submitted to a constant flow [74]. In this dissertation, the part of the velocity potential (VP) of the fluid motion due to the presence of the body in the stream was represented as a superposition of potentials of point source distributed along a segment of the body axis and lying entirely within the body. The boundary condition of vanishing normal flow at the body surface leads to a linear integral equation for the source strength distribution (SSD); the complete uniform asymptotic expansion of the solution of this integral equation was obtained as a function of the slenderness ratio (ϵ), defined as the ratio of the body's maximum radius to its length. The VP equation of the flow over the body can be written as

$$\phi = \phi_{\text{stimuli}} + \phi_{\text{body}}. \tag{2.29}$$

In the case of constant flow

$$\phi_{\text{stimuli}} = U_0 z. \tag{2.30}$$

Thus, the VP equation of the flow over the body can be written as

$$\phi(r^2, z, \epsilon) = U_0 z - \frac{1}{4\pi} \int_{\alpha(\epsilon)}^{\beta(\epsilon)} \frac{f(\xi, \epsilon)}{\sqrt{(z-\xi)^2 + r^2}} d\xi, \tag{2.31}$$

where $f(z, \epsilon)$ is the SSD function, and $\alpha(\epsilon)$ and $\beta(\epsilon)$ determine the distribution extent within the body and can be expressed as a power series in ϵ [68]

$$\alpha(\epsilon) = \frac{1}{4}c_1\epsilon^2 - \frac{1}{16}c_1c_2\epsilon^4 + \frac{1}{64}\epsilon^6(c_1^2c_3 + 2c_1c_2^2) + O(\epsilon^8) \tag{2.32}$$

with $c_j = \frac{\partial^j S(z)}{\partial z^j}\frac{1}{j!}$ at $z = 0$, and

$$\beta(\epsilon) = 1 - \frac{1}{4}d_1\epsilon^2 + \frac{1}{16}d_1d_2\epsilon^4 - \frac{1}{64}\epsilon^6(d_1^2d_3 + 2d_1d_2^2) + O(\epsilon^8), \tag{2.33}$$
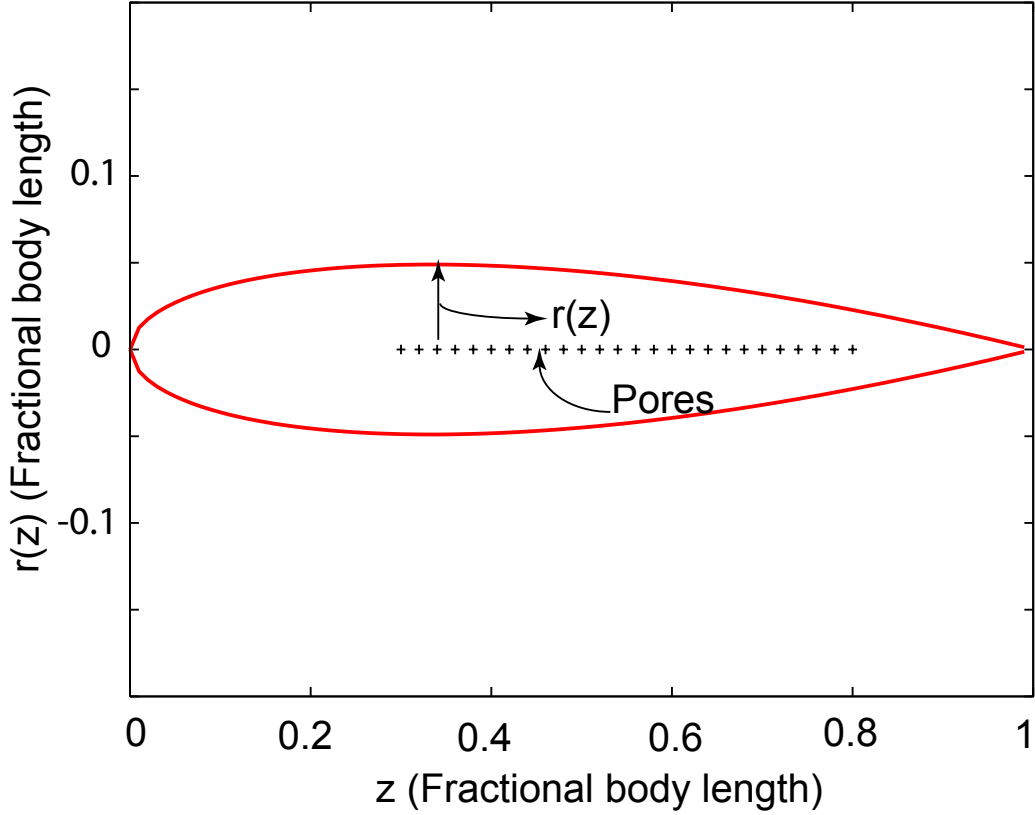
Figure 2.5: *Transversal projection of the radially symmetrical function for the fish body. The dorsal lateral is modelled as a line of pores occupying half of the length of the fish starting at 0.3 up to 0.8 (length fraction of the complete body).*

with $d_j = (-1)^j \frac{\partial^j S(z)}{\partial z^j} \frac{1}{j!}$ at $z = 1$. The condition of vanishing normal velocity on the body surface when used with the VP equation results in

$$2\pi\epsilon U_0 S'(z) = \frac{\partial}{\partial z} \int_{\alpha(\epsilon)}^{\beta(\epsilon)} \frac{(z-\xi)}{\sqrt{(z-\xi)^2 + \epsilon^2 S(z)}} f(\xi, \epsilon) d\xi \,. \qquad (2.34)$$

This equation is an integral equation for the SSD function $f(z, \epsilon)$, where Handelsman and Keller[68] have shown that it can be expanded as a series of the form

$$f(z, \epsilon) = \sum_{n=1}^{\infty} \sum_{m=0}^{n-1} \epsilon^{2n} (ln(\epsilon^2))^m f_{nm}(z) \,, \qquad (2.35)$$

where $f_{nm}(z)$ can be obtained recursively with the following system of equations,

$$f_{10} = \pi U_0 S'(z) \tag{2.36}$$

$$f_{n0} = \sum_{j=1}^{n-1} \frac{d}{dz}(L_j f_{n-j,0}) \qquad (n \geq 2) \tag{2.37}$$

$$f_{1m} = 0 \qquad (m \geq 1) \tag{2.38}$$

$$f_{nm} = \frac{-1}{2}[\sum_{j=1}^{n-1} \frac{d}{dz}(L_j f_{n-j,m}) +$$

$$\sum_{j=1}^{n-1} \frac{d}{dz}(G_j f_{n-1,m-1})] \qquad (n \geq 2, m \geq 1). \tag{2.39}$$

The L_j and G_j are linear operators [68]. In the present study, for the case of a moving body in open water, the SSD has been computed to a rest of $O(\epsilon^8)$ with

$$f(z, \epsilon) = \sum_{n=1}^{3} \sum_{m=0}^{n-1} \epsilon^{2n} (\ln(\epsilon)^2)^m f_{nm}(z). \tag{2.40}$$

2.5.2   Dipole Oscillating Near the Fish Body

The derivation proposed can lead to the calculation of the pressure difference on the pores for a motionless fish stimulated by a dipole in its proximity.

Stimulus

For the purpose of this analysis, only a dipole in a plane perpendicular to the fish dorsal canal lateral line will be considered. The flow field of a sphere oscillating with a frequency f can be approximated to that of a stationary doublet with oscillating strength μ located at the sphere center in its rest position the oscillation amplitude s must be small in comparison to the sphere radius a. In this case, the strength of the doublet can be written as [95, §92]

$$\mu = 2\pi\omega s a^3 \sin(\omega t), \tag{2.41}$$

where $\omega = 2\pi f$ .The coordinates of the sphere center are X, Y, Z, and its axis of oscillation makes an angle δ with the $z \cdot x$ plane, where the projection of this axis in

$z \cdot x$ plane makes an angle γ with the z axis. The equation for the velocity potential (VP) of the oscillating sphere can be written as

$$\phi^0(x, y, z) = \frac{\mu}{4\pi} \left(\cos\delta \sin\gamma \frac{\partial}{\partial x} + \sin\delta \frac{\partial}{\partial y} + \cos\delta \cos\gamma \frac{\partial}{\partial z} \right) \left(\frac{1}{R} \right), \qquad (2.42)$$

where

$$R = [(x - X)^2 + (y - Y)^2 + (z - Z)^2]^{\frac{1}{2}}. \qquad (2.43)$$

This equation can be transformed into cylindrical coordinates r, θ, z with $x = r \cdot \cos(\theta)$, $y = r \cdot \sin(\theta)$ and $z = z$. Three independent modes of oscillation for the sphere will be considered for the sphere, the first being in the z direction when δ and γ are equal to zero. Which is mode a

$$\phi^0(r, \theta, z) = \frac{-\mu}{4\pi R^3}(z - Z), \qquad (2.44)$$

The second, when $\delta = \pi/2$, (γ has no meaning), in the y direction

$$\phi^0(r, \theta, z) = \frac{-\mu}{4\pi R^3}(r \cdot \sin(\theta) - Y), \qquad (2.45)$$

The third, when $\delta = 0$ and $\gamma = \pi/2$, in the x direction

$$\phi^0(r, \theta, z) = \frac{-\mu}{4\pi R^3}(r \cdot \cos(\theta) - X). \qquad (2.46)$$

This study just treats the case where the sphere's center is located in the $z - x$ plane, so that $Y = 0$.

Potential Formulation

The flow field is not axially symmetric if the sphere location or its axis of oscillation depart from the body axis. The presence of the body in the flow can then be represented as a superposition of potentials of point sources and higher-order singularities distributed along a segment of the body axis and lying within it [62]. The function of the singularities strength distribution (SSD), can be written as

$$g(z, \epsilon) = \sum_{n=0}^{\infty} g_n(z, \epsilon). \qquad (2.47)$$

The VP function of the body can then be written as

$$\phi^b(r, \theta, z) = -\frac{1}{4\pi} \sum_{n=0}^{\infty} \int_{\alpha(\epsilon)}^{\beta(\epsilon)} \frac{r^n \exp(in\theta)(\xi - \alpha)^n(\beta - \xi)^n}{[r^2 + (z - \xi)^2]^{n+1/2}} g_n(\xi, \epsilon)d\xi. \qquad (2.48)$$

The components of the SSD function can be found after expanding the VP function of the oscillating sphere with a series of the form [62]

$$\phi^0(r, \theta, z) = \sum_{n=0}^{\infty} r^n \psi_n(r^2, z) \exp(in\theta) \,, \tag{2.49}$$

$$\frac{\partial}{\partial n}(\phi^0 + \phi^b) = 0 \,. \tag{2.50}$$

When the boundary condition (2.50) is used with the series expansion VP of the oscillating sphere (2.49) and of body (2.48) this form yields a linear integral equation for each singularity order n. From the leading terms of the uniform asymptotic solutions of the integral equations, the SSD function $g_n(z, \epsilon)$ can be determined as

$$g_0(z, \epsilon) \sim \epsilon^2 2\pi \frac{d}{dz}[\psi_0(0, z)S(z)] + O(\epsilon^4 \ln(\epsilon^2)) \,, \tag{2.51}$$

$$g_n(z, \epsilon) \sim -\epsilon^2 \frac{\pi n^2}{2^{2n-3}} \binom{2n-1}{n} \left[\frac{S(z)}{z(1-z)}\right]^n \psi_n(0, z) \tag{2.52}$$

$$+ O(\epsilon^{2n+2} \ln(\epsilon^2)) \qquad (n \geq 1) \,. \tag{2.53}$$

The expression of the ψ for the three modes (see 2.44, 2.45 and 2.46) was developed by Hassan [76].

2.5.3   Constant Flow and Dipole

The velocity potential in the case of a vibrating sphere in presence of a fish body is taken as $\phi_{\text{dipole+body}}$, and the potential in the case of a constant flow with velocity $\mathbf{v}$ in the presence of a fish body is taken as $\phi_{\text{constant flow+dipole}}$.

In case of a vibrating sphere, for which the center of mass moves *with the same velocity* $\mathbf{v}$, as the constant flow, the velocity potential $\phi_{\text{dipole+constant flow+body}}$ will be shown to be approximately

$$\phi_{\text{dipole+constant flow+body}} \approx \phi_{\text{dipole+body}} + \phi_{\text{constant flow+body}} \,. \tag{2.54}$$

For the case where a fish swims past a vibrating object, the Laplace equations can be applied to fluids, where $\nabla^2 \phi_{\text{dipole+body}} = 0$ and $\nabla^2 \phi_{\text{constant flow+body}} = 0$, therefore also $\nabla^2 \phi_{\text{dipole+constant flow+body}} = 0$. There only remains to be shown that the potential $\phi_{\text{dipole+constant flow+body}}$ given above fulfills the appropriate boundary condition at infinity

$$\nabla \phi_{\text{dipole+constant flow+body}} = \mathbf{v} \,, \tag{2.55}$$

at the fish body

$$\frac{\partial \phi_{\text{dipole+constant flow+body}}}{\partial \mathbf{n}} = 0 \qquad (2.56)$$

and at the surface of the sphere moving with velocity $\mathbf{v} + \mathbf{u}(t)$

$$\frac{\partial \phi_{\text{dipole+constant flow+body}}}{\partial r} = \frac{(\mathbf{v} + \mathbf{u}(t)) \cdot \mathbf{r}}{r} . \qquad (2.57)$$

For the potential $\phi_{\text{dipole+body}}$, the boundary condition $\nabla \phi_{\text{dipole+body}} = 0$ applies at infinity, $\partial \phi_{\text{dipole+body}}/\partial \mathbf{n} = 0$ at the fish body and $\partial \phi_{\text{dipole+body}}/\partial r = \mathbf{u}(t) \cdot \mathbf{r}/r$ at the surface of the sphere. For the potential $\phi_{\text{constant flow+body}}$, the boundary condition $\nabla \phi_{\text{constant flow+body}} = \mathbf{v}$ applies at infinity and $\partial \phi_{\text{constant flow+body}}/\partial \mathbf{n} = 0$ applies at the fish body. Therefore, (2.55) and (2.56) correspond exactly. At the surface of the sphere, the following description can be considered

$$\frac{\partial \phi_{\text{dipole+constant flow+body}}}{\partial r} = \frac{[\mathbf{v}(\mathbf{r}) + \mathbf{u}(t)] \cdot \mathbf{r}}{r} , \qquad (2.58)$$

where $\mathbf{v}(\mathbf{r})$ is the velocity of the constant flow at position $\mathbf{r}$. As the influence of the fish body is small if the sphere is far enough away from the body $\mathbf{v}(\mathbf{r}) \approx \mathbf{v}$. Therefore, the boundary condition (2.57) corresponds approximately.

In the case of a dipole in a constant flow, it must also be shown that the two earlier solutions are additive in terms of body potential. The external potential of a dipole (translating or a oscillating sphere[95, §92]) takes the form of

$$\phi^0(x, y, z) = U_0 z + \frac{\mu}{4\pi} \left(\cos\delta \sin\gamma \frac{\partial}{\partial x} + \sin\delta \frac{\partial}{\partial y} + \cos\delta \cos\gamma \frac{\partial}{\partial z} \right) \left(\frac{1}{R} \right) . \qquad (2.59)$$

Since this corresponds exactly to the addition of the two previous potential, the only thing that remains to be shown is that the formulation of the body potential derivated leads to two different body terms. The formulation proposed for a symmetric potential [68] is also the formulation of the solution in the general case for a finite potential [62]. The additivity can be derived from the potential formulation hypothesis. In general this correspond to

$$\phi^0(r, z) = \phi_{\text{constant flow}}(r^2, z) + \phi_{\text{dipole}}(r, z) , \qquad (2.60)$$

$\phi^0(r, z)$ can also be described according to

$$\phi_0(r, z) = \phi_{\text{constant flow}}(r^2, z) + \sum_{n=0}^{\infty} (r^n \psi_{\text{n dipole}}(r, z) \exp(in\theta)) . \qquad (2.61)$$

The potential integral can be written as

$$\phi^b(r,\theta,z) = -\frac{1}{4\pi} \sum_{n=0}^{\infty} \int_{\alpha(\epsilon)}^{\beta(\epsilon)} \frac{r^n \exp(in\theta)(\xi-\alpha)^n(\beta-\xi)^n}{[r^2 + (z+\xi)^2]^{n+\frac{1}{2}}} \tilde{g}_n(\xi,\epsilon)d\xi. \qquad (2.62)$$

The $\tilde{g}(z,\epsilon)$ being the new SSD function,will take the form

$$\tilde{g}_0(z,\epsilon) \sim \epsilon^2 2\pi \frac{d}{dz}[(\phi_{\text{constant flow}}(r^2,z) + \phi_{\text{dipole}}(r,z))S(z)] + O(\epsilon^4 \ln(\epsilon^2)) \qquad (2.63)$$

$$\tilde{g}_0(z,\epsilon) = f(z,\epsilon) + g_0(z,\epsilon). \qquad (2.64)$$

and

$$\tilde{g}_n(z,\epsilon) = g_n(z,\epsilon), \qquad (2.65)$$

where $f(z,\epsilon)$ and the $g_n(z,\epsilon)$ are the SSD function for the constant flow alone and the dipole alone. Therefore the integral for the body potential can be re-specified as

$$\phi^b(r,\theta,z) = \phi^b(r\theta,z) = \phi^b(r^2,\theta,z)_{\text{constant flow}} + \phi^b(r,\theta,z)_{\text{dipole}}. \qquad (2.66)$$

2.5.4 Numerics

The integration has been realized on Maple V and Mathematica using an adaptative Gauss 10 points and a Kronrod 21 points. The numerical convergence was tested with $\epsilon = 5 \cdot 10^{-9}$.

2.5.5 Numerical Simulation

Parameters
The parameters used as defaults are presented in the following table 2.1. Any parameter with another value for a specific simulation will be specified in the figure caption and in the text.

Results

The flow potential for a constant flow, for a vibrating sphere and a for a vibrating sphere in a constant flow was calculated using the theory developed here. To calculate the pressure differences we solved the Bernouilli equation (2.24), and then we said that $\Delta P(z,t) = P(z+\delta/2,t) - P(z-\delta/2,t)$, where δ is the distance between two consecutive pores. Figure 2.6 shows that the effect of the constant flow is filtered mechanically by the canal lateral-line system. This filtering was already observed experimentally [47]. The next figure 2.7 shows that the effect of the body is also negligible for a dipole oscillating at 1 cm of the fish body. In this picture we also show that the effect of the curvature is negligible. The increase of intensity shown in

Parameters	Values
ϵ	1/20
K	6.175
Constant flow U_0	10 cm/s
Sphere radius a	5 mm
X	1 cm
Y	0
Z	5 cm
Distance between two consecutive pores δ	2 mm

Table 2.1: *Default parameters for the hydrodynamic simulations*

Fig. 2.7 can be explained by the non-slip condition of the Euler equation. We will show it in section 3.1.

In this chapter, we have discussed the effect due to the boundary layer, the geometry of the fish body on object detection by means of the lateral line. These results will be used in the next chapter to establish a minimal model based on the potential formulation of the stimulus alone to explain the firing rate observed at the afferent of the lateral-line system (SN and CN) of fish.
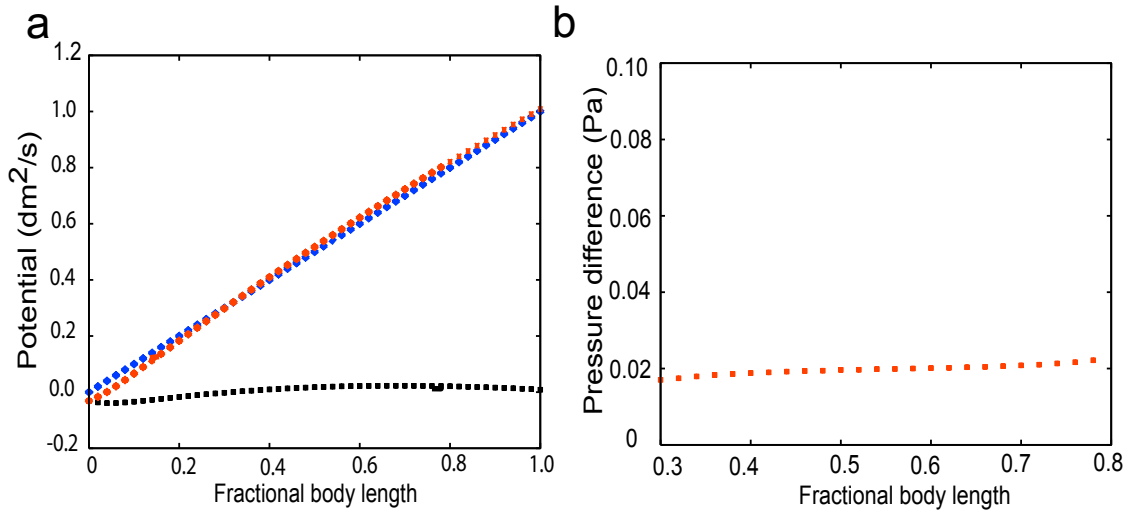
Figure 2.6: **a** *Simulation of the flow potential* $(\mathrm{dm}^2/s^2, 1\mathrm{dm} = 10\,\mathrm{cm})$ *for a fish body in a constant flow of* $10\,\mathrm{cm/s}$ *as a function of the position on the fish body (fractional body length).The black square represents perturbation due to the fish body only (2.31), the red square is the potential due to the constant flow only (2.30). Finally, the blue square represents the perturbation due to a fish in a constant flow.* **b** *Pressure difference at the pores of the canal lateral line for a flow of* $10\,\mathrm{cm/s}$. *This image confirms the result of [47] and shows that the fact that canal lateral-line detectors filter constant flow is due to the mechanics of the canal and not to neuronal filtering. This figure shows that the effect of the body in the flow is negligible in comparison to the effect of flow alone.*
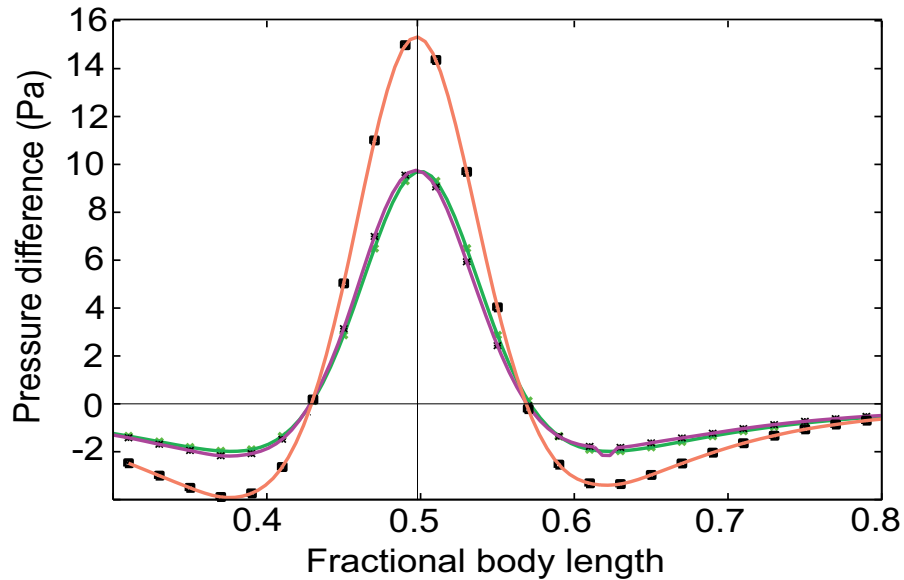
Figure 2.7: *Pressure difference (Pa) at the pores of the canal lateral-line system as a function of the position (fish body length) on the fish body for a dipole at* 1 cm *from the fish body (see 2.5). The red line represents the effect of the body and the dipole together, the black squares represent the effect of the fish body and the dipole in a constant flow of* 10 cm/s, *the green line indicates the effect of the dipole alone, although respecting the exact position of the detector on the fish body. Finally, the purple line,which can hardly be seen in regard to the green one, represents the pressure difference on a flat line at a distance of* 1 cm *from the dipole. This figure shows that the shape of the pressure-difference curve is not affected by the presence of the body, the curvature or a constant flow.*

3. Minimal Model

In the present chapter, we will provide a minimal model based on the potential formulation of the stimulus and we will compare it with the activity at the nerve afferents.

To theoretically analyze a complicated situation, models with a minimal number of assumptions are very useful. For the canal lateral-line system, a "minimal" model means a straight line of detectors with equidistant pores and cupulae inbetween. More precisely, These detectors are either sensitive to velocity (SN) or to the pressure difference between pores (CN), i.e., to acceleration.

In order to establish our minimal model, we make the following assumptions (see Fig. 3.1 for a dipole):

- The detectors are arranged in a flat line (Figs. 2.7 and 3.1) of detectors sensitive either to velocity or pressure difference.

- The stimulus is given by a velocity potential (consult sections 2.2 and 2.3).

- The stimulus, usually a vibrating sphere, is at the origin.

- The detectors are located at a distance D from the stimulus.
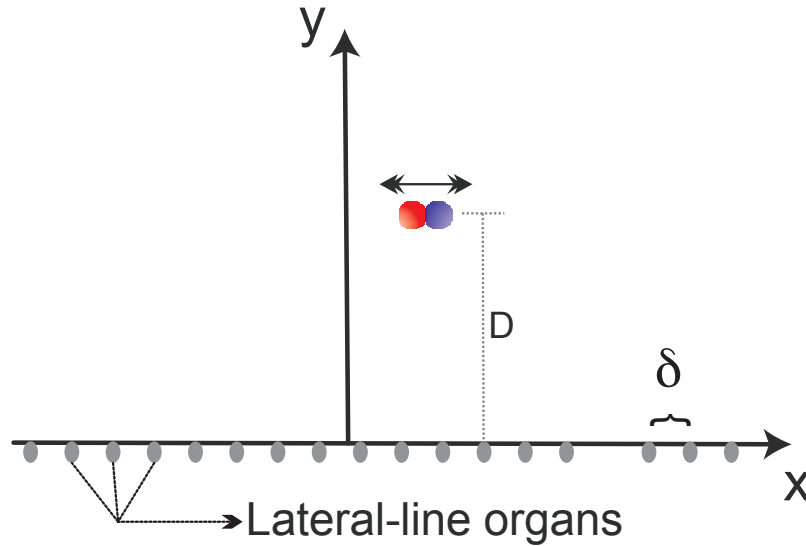
Figure 3.1: *In the 2-dimensional* minimal *model, the lateral-line organs are arranged in a linear array on the x-axis. A stimulus is located at position $(0, D)$. It oscillates parallel to the x-axis, generating a dipolar velocity field.*

3.1 Vibrating Sphere

As we discussed earlier, in potential flow theory (section 2.4) any source can be written in the form of a multipole expansion. The multipole expansion is of great interest when the series converges and we can thus keep the first term relevant to our problem. If the region we consider does not have any gain or loss of fluid, the first term (the *monopole*, either a source or a sink alone) vanishes and the dominant term in the series will be the dipole (a couple of source and sink). The question is whether the higher-order terms in the series are relevant. As we noted earlier, the higher-order terms are relevant if the fish is at less than one body length distance from the body length of the object to be detected (call it the *prey*) [131]. The effective range of detection of the lateral-line system is one body length away from the *predator*. The effect of the form of the prey in distance determination for short distances will be discussed in section 5.7.

For a sphere at position (D_x, D_y) that oscillates *parallel* to the x-axis and in

the plane of the lateral-line organ (Fig. 3.1) with $\mu(t) := 2\pi\omega s a^3 \sin(\omega t)$, the two-dimensional potential ϕ, as described in Lamb [95, §92], is

$$
\phi_{\parallel}(x, y, t) = \frac{-\mu(t)}{4\pi} \left\{ \frac{(x - D_x)}{[(x - D_x)^2 + (y - D_y)^2]^{3/2}} + \frac{(x - D_x)}{[(x - D_x)^2 + (y + D_y)^2]^{3/2}} \right\},
\tag{3.1}
$$

which satisfies the boundary condition $\boldsymbol{v} \cdot \boldsymbol{n} = 0$ of the Euler equation at the surface of the sphere. If not stated otherwise, the sphere has a diameter $a = 5$ mm and oscillates at frequency $f = 50$ Hz (angular frequency $\omega = 2\pi f$) with a displacement amplitude $s = 0.8$ mm. The resulting water velocity $v_x = \partial\phi_{\parallel}/\partial x$ in x-direction is

$$
v_x(x, y = 0, t) = \frac{\mu(t)}{2\pi} \frac{(2x^2 - D^2)}{(x^2 + D^2)^{5/2}}.
\tag{3.2}
$$

The boundary condition here just results, in twice the velocity produced by a dipole *without* boundary condition. This explains the result presented in Figs 2.4 and 2.7. In the case of a sphere oscillating *perpendicularly* to the skin of the fish, i. e., in the direction of the y-axis (Fig. 3.1), we find[1]

$$
\phi_{\perp}(x, y, t) = \frac{-\mu(t)}{4\pi} \left\{ \frac{y - D_y}{[(x - D_x)^2 + (y - D_y)^2]^{3/2}} - \frac{y + D_y}{[(x - D_x)^2 + (y + D_y)^2]^{3/2}} \right\}.
\tag{3.3}
$$

The resulting water velocity $v_x = \partial\phi_{\perp}/\partial x$ in x-direction is

$$
v_x(x, y = 0, t) = \frac{3\mu(t)Dx}{2\pi (x^2 + D^2)^{5/2}}.
\tag{3.4}
$$

Canal neuromasts are sensitive to the pressure *difference* between two adjacent pores. We are, therefore, interested in the pressure field and will show analytically that the pressure difference distribution along the lateral line canal has a form *identical* to the velocity field.

To calculate the pressure in a *non*viscous fluid at the pores of the canal lateral line, we can use the Bernoulli equation (2.24),

---

[1] The potential for an *arbitrary* axis of vibration in the xy-plane making an angle α with the x-axis is $\phi(x, y, t) = \phi_{\parallel}(x, y, t) \cos\alpha + \phi_{\perp}(x, y, t) \sin\alpha$.

$$\left[p(x,y,t) + \frac{1}{2}\rho \boldsymbol{v}^{\,2}\,(x,y,t) + \rho \frac{\partial \phi_{\|}}{\partial t} \right]_{\mathrm{y=D}} = p_0(t)\,, \tag{3.5}$$

where $\boldsymbol{v^2}$ is the square of the water flow velocity at the body and $p_0(t)$ is a constant depending on the time t only. Since the velocity $v_y = \partial\phi_{\|}/\partial y$ perpendicular to the skin is zero at the skin because of the Euler boundary condition, we find $\boldsymbol{v}^{\,2} = v_x^2$. Using. (3.3) for a sphere at distance D from the skin oscillating parallel to the x-axis we get

$$\begin{aligned} \boldsymbol{v}^{\,2}(x, y=0, t) &= v_x^2 = \left(\partial\phi_{\|}/\partial x\right)^2 \\ &= \frac{a^6\omega^2 s^2 \left(2x^2 - D^2\right)^2}{\left(x^2 + D^2\right)^5} \sin^2\left(\omega t\right) . \end{aligned} \tag{3.6}$$

Again, the notion of a *thin* boundary layer is important since outside of this layer we can use the Euler and Bernoulli equations to obtain the pressure. It holds that $\partial_t\phi_{\|} \gg \boldsymbol{v}^{\,2}$ since $a^3\omega s \gg a^6\omega^2 s^2$.

The time derivative ∂_t of the velocity potential for an oscillating sphere is

$$\frac{\partial\phi_{\|}\left(x,y,t\right)}{\partial t} = \frac{1}{2\pi}\frac{\mathrm{d}\mu(t)}{\mathrm{d}t}\frac{x}{\left(x^2 + D^2\right)^{3/2}} \tag{3.7}$$

where $\mathrm{d}\mu\left(t\right)/\mathrm{d}t = 2\pi\omega^2 a^3 s \cos\left(\omega t\right)$. The water velocity within the canal and thus the deflection of the CNs is proportional to the pressure difference Δp between two adjacent pores at position $(x, y = 0)$ on the skin

$$\Delta p(x, y=0, t, \delta) = \frac{\partial\phi_{\|}(x+\delta, 0, t)}{\partial t} - \frac{\partial\,,\phi_{\|}(x, 0, t)}{\partial t} \tag{3.8}$$

where δ is the distance between the pores. As δ is small, we obtain

$$\begin{aligned} \Delta p(x, y=0, t, \delta) &\approx \frac{\partial}{\partial t}\frac{\partial\phi_{\|}(x, y=0, t)}{\partial x}\cdot\delta \\ &= \omega\,v_{x-\mathrm{max}}(x, y=0)\cos(\omega t)\cdot\delta\,. \end{aligned} \tag{3.9}$$

In general, using (3.1) we get

$$\begin{aligned} \Delta p(x, y=0, t, \delta) &= -\omega^2 a^3 s\rho \left[\frac{\delta + x}{\left((\delta + x)^2 + D^2\right)^{3/2}} \right. \\ &\left. \quad - \frac{x}{(x^2 + D^2)^{3/2}} \right]\cos(\omega t)\,. \end{aligned} \tag{3.10}$$

Figure 3.2 shows a plot of the maximum amplitude of $\Delta p(x, y = 0, t, \delta)$ as a function of x for $\cos\left(\omega t\right) = -1$. It reveals that the pressure difference distribution for a dipole has a form *identical* to the velocity field.
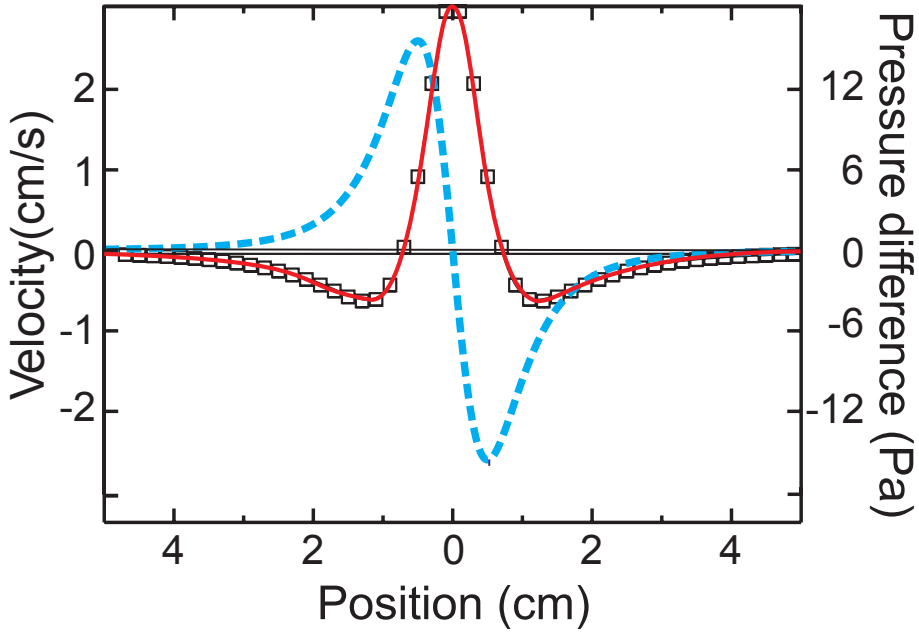
Figure 3.2: *Amplitude of the velocity v_x near the skin of the fish in dependence upon the x-position. The stimulus is an oscillating sphere at $D = 1$ cm from the skin. The sphere is oscillating either parallel (solid line, cf. (3.2)) or perpendicularly (dashed line, cf. (3.4)) to the line of detectors and thus generates either a triphasic or a bi*phasic response. The squares represent the pressure difference between two adjacent pores at a distance of 2 mm cf. (3.10). The velocity field and pressure difference field are proportional to each other; cf. (3.9).*

3.1.1 Comparison Between Modeled and Measured Data

We now test the theoretical model by comparing its prediction to results obtained from recordings of lateral-line nerve fibers. As shown in previous studies, the two observed patterns can be predicted by the amplitude and direction of the pressure gradients surrounding a dipole source for a vibration axis that is either parallel (*tri*modal pattern) or orthogonal (*bi*modal pattern) to the orientation of the pores [30, 33, 36, 126].

To determine the degree of agreement between the theoretical predictions and the measured neuronal responses, we compare a "firing rate" function of the form (triphasic field)

$$F(x) = \left| I + A \frac{[2(x - x_0)^2 - D^2]}{[(x - x_0)^2 + D^2]^{5/2}} \Theta \right| \tag{3.11}$$

with actual receptive fields. Here, I is the experimentally determined instantaneous

firing rate, A denotes a scaling parameter and x_0 is the position of the sphere. The variable Θ is 1 when the neuronal response is in phase with the vibrating sphere and -1 when there is a 180° phase difference. This is due to the fact that the afferent nerves respond only to the water velocity in one direction parallel to the greater axis of the cupula($+$ or $-$), the reader is also referred to figure 5.1. In other words, the hair cells can be divided into two populations of opposite polarity, cf. Fig. 1.1 For a description of the experimental setup, the reader is referred to Goulet et al [65].

Accordingly, in the case of a sphere moving perpendicularly to the skin of the fish (biphasic field), the firing rate is given by

$$F(x) = \left| I + A \frac{D(x - x_0)}{[(x - x_0)^2 + D^2]^{5/2}} \Theta \right| . \tag{3.12}$$

As shown in Fig. 3.3, the agreement between the modeled firing rate F and the three arbitrarily chosen neuronal receptive fields is quite good. In the next chapter, we will deduce the FI curves for the SNs and will show that, even thought the firing rate is best fit with a sigmoidal function, a linear function up to saturation point explains the data satisfactorily well.

3.1.2 Constant Flow

Former studies [45, 47] had shown that the firing rate of SN increases significantly in response to increasing the velocity of a constant flow, whereas for a CN the flow is filtered (see also for instance Fig. 2.6). However, it has been shown that for some flow-sensitive medulla units the firing rate increases in presence of a flow, but this does not mask the response to an additional dipole [48]. In order to model the activity at the afferent nerves, we use (3.11) and increases the instantaneous firing rate in order to include the effect of the flow.

3.2 Translating Sphere

The velocity field due to a *translating* sphere is a dipole [95, §92]. Assuming that a sphere is moving in the x-direction with velocity w and starting point x_0 at time $t = 0$, then the distance in the x-direction between a neuromast at position x and the sphere at time t is

$$X(t, x) = x - (x_0 + wt) . \tag{3.13}$$
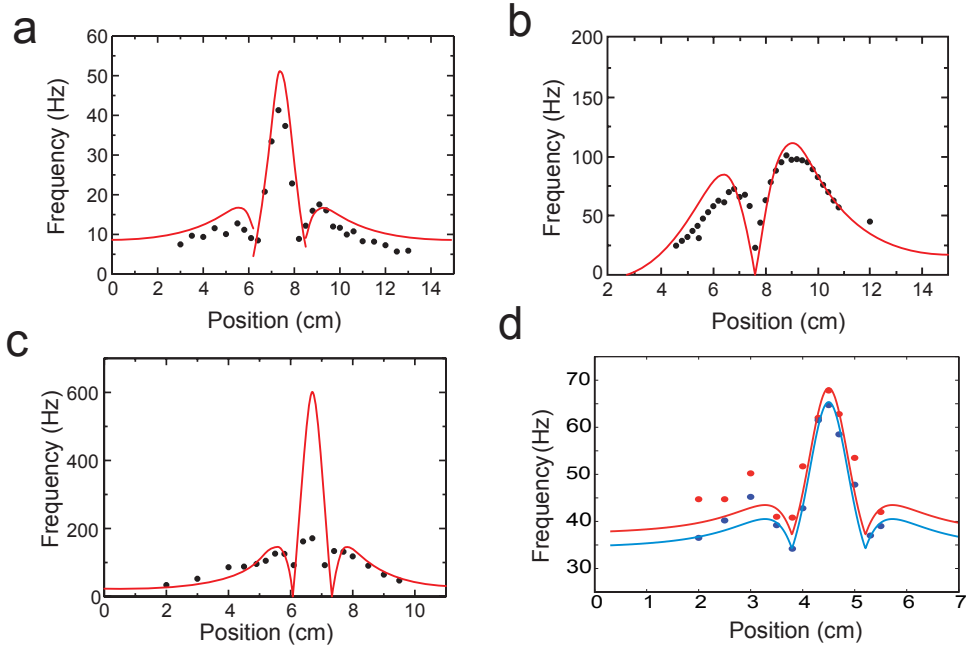
Figure 3.3: *Experimentally measured firing rates (black dots, mean of ten stimuli) at afferent nerves and theoretical predictions (solid lines) of (3.11) and (3.12).* **a** *A triphasic field of a CN for an oscillating sphere at distance $D = 1.5\,$cm from the skin of the fish, instantaneous firing rate $I = 8$, and the free parameter $A = 170$ to fit the amplitude.* **b** *A* biphasic field for a sphere at distance $D = 2.6\,$cm from the skin of the fish, $I = 13$ and $A = 6000$. **c** *A triphasic field of a superficial neuromast for an oscillating sphere at distance $D = 0.93\,$cm, $I = 13$ and $A = 500$. In this case, the difference between theory and experiment is probably related to rate saturation, the maximum firing rate already being near 200 Hz.* **d** *Effect of a $10\,cm/s$ water flow on the encoding of a dipole oscillating at $D = 1.2\,$cm by superficial neuromasts. The experimental firing rates are represented by blue dots (without flow) and the red dots (with flow). The free parameter is $A = 152$ and the instantaneous firing rate is $I = 34.2$ for the blue line (without flow) and $I = 40.8$ for the red line (with flow).*

41

The velocity potential is

$$\phi_\parallel(x,y,t) = 2a^3w\left\{\frac{X(t,x)}{[X(t,x)^2+(y-D)^2]^{3/2}} + \frac{X(t,x)}{[X(t,x)^2+(y+D)^2]^{3/2}}\right\}.$$

(3.14)

In this case, the velocity field in the x-direction becomes

$$v_x(x,t) = \frac{a^3w}{2}\frac{(2X(t,x)^2-D^2)}{[X(t,x)^2+D^2]^{5/2}}.$$

(3.15)

Due to the Bernoulli equation (3.5), we find

$$p(x,y,t) - p_0(t) = -\rho\left[\frac{1}{2}\left(\frac{\partial\phi}{\partial x}\right)^2 + \frac{\partial\phi}{\partial t}\right].$$

(3.16)

Since the second term dominates, the pressure difference between two consecutive pores is approximately

$$\Delta p(x,t) \approx \frac{\mathrm{d}}{\mathrm{d}x}\left.\frac{\partial\phi_\parallel(x,y,t)}{\partial t}\right|_{y=0}\cdot\delta,$$

(3.17)

where δ is the distance between two pores. Using (3.14) we arrive at

$$\begin{aligned}\Delta p(x,t) &= 2a^3w^2\delta\frac{\partial^2}{\partial^2 X}\frac{X(t,x)}{[X^2(t,x)+D^2]^{3/2}} \\ &= 6a^3w^2\delta\frac{X[2X^2(t,x)-3D^2]}{[D^2+X^2(t,x)]^{7/2}}.\end{aligned}$$

(3.18)

This field is *anti*symmetric (biphasic) in x. The difference between the velocity field and the pressure gradient at the pores of the canal lateral-line system is that the temporal derivative of the potential (3.14) implies a second spatial derivation of the velocity field (chain rule) in comparison result (3.10) we found earlier for the vibrating sphere.

3.2.1 Comparison Between Modeled and Measured Data

It is time to propose a transfer function for the activity pattern produced by a translating sphere moving parallel to the greatest axis of the fish, the x-axis. We will consider the response of both SNs and CN nerves for a sphere translating in the direction head to tail (the $+$ direction), or from tail to head (the $-$ direction).

The rate transfer function for SNs (velocity field) takes the form

$$r(x,t) = In + A * w * \frac{(2X(t,x)^2 - D^2)}{(X(t,x)^2 + D^2)^{5/2}} \, . \tag{3.19}$$

The multiplication of the constant A by w (the velocity of the sphere) is necessary to keep the sign of w. By contrast, the transfer function for a nerve innervating canal neuromasts is

$$r(x,t) = In + A\frac{X[2X^2(t,x) - 3D^2]}{[D^2 + X^2(t,x)]^{7/2}} \, . \tag{3.20}$$

Here, however, we need not multiply the constant A by w since the strength of the field is proportional to w^2 so that it can be included in A. Since the afferent nerves are either sensitive to water motion in the $+$ or the $-$ direction, we have to say that the firing rate function takes the form of an afferent sensitive to the $+$ direction

$$F(x,t) = \begin{cases} r(x,t) & \text{if } r(x,t) > 0 \,, \\ 0 & \text{if } r(x,t) < 0 \,, \end{cases} \tag{3.21}$$

For an afferent sensitive to the $-$ direction, it then takes the form of

$$F(x,t) = \begin{cases} 2In - r(x,t) & \text{if } r(x,t) < In \\ 0 & \text{if } r(x,t) > In \end{cases} \tag{3.22}$$

That is done to ensure that both nerves have an instantaneous firing rate of In and that the firing rate can decrease to zero. The experimental protocol for the translating sphere is described in Engelmann et al [46]. The result for SNs and CNs in the $+$ and $-$ directions is presented in Fig. 3.4.
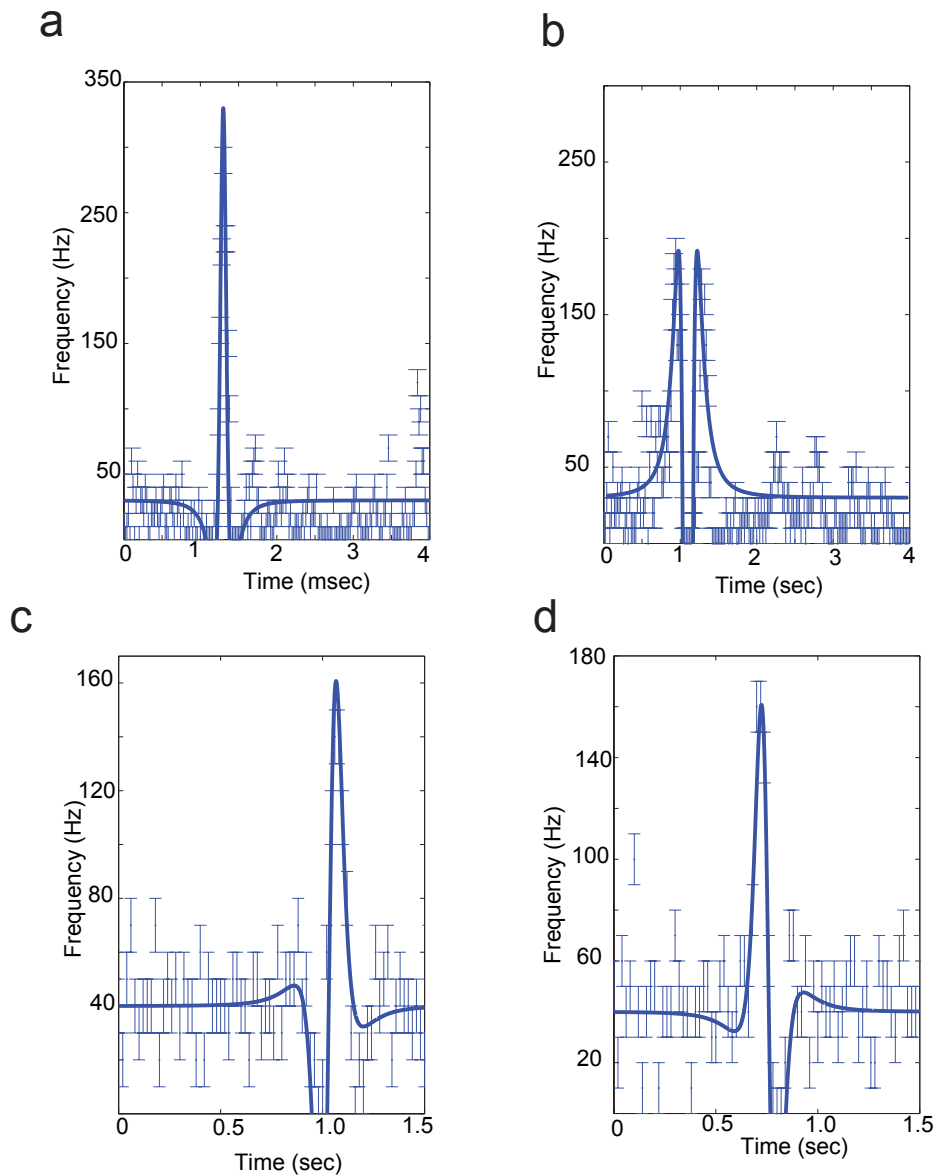
Figure 3.4: *Experimentally measured firing rates (indicated by blue vertical line, as error bars of ±10 Hz) at afferent nerves and theoretical predictions solid lines; cf ((3.21) and (3.22)) of the firing rate for a translating sphere for both SN and CN.* **a** *A neuronal response field of a SN for a translating sphere in the + direction (head to tail) at distance D = 1. cm from the skin of the fish, with instantaneous firing rate I = 40 and the free parameter A = 22 to fit the amplitude.* **b** *Similar to* **a** *but the sphere is translating in the − direction (tail to head).* **c** *A biphasic response of a canal neuromast for a translating sphere in the + at a distance D = 1 cm, I = 40 and A = 5400.* **d** *same as* **c** *but the sphere is translating in the − direction.*
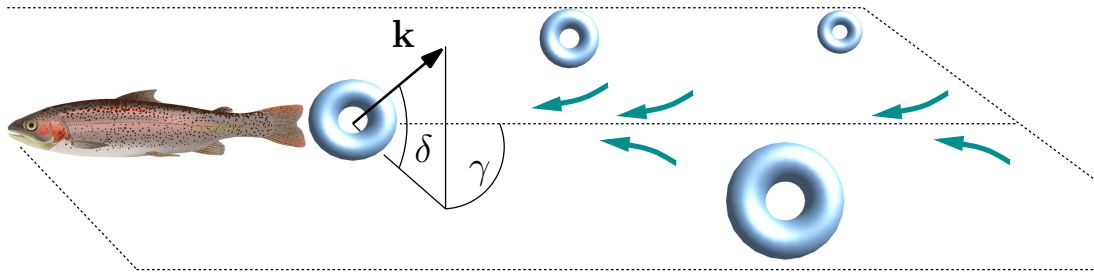
Figure 3.5: *A fish's wake consists of vortex rings originating from the tail beats with a velocity component (thick arrows) that compensates for the fish's displacement. Vector **k** describes the the orientation of a vortex. Picture due to Franosch et al [54].*

3.3 Wake Tracking and Detection of Vortex Ring

In the preceding two subsections, we have show that the lateral line of fish can encode simple stimuli well (vibrating sphere in section 3.1, and translating sphere in section 3.2). Here, we will show that the lateral-line system encodes and uses for prey capture the traces made by other fish when moving in the water while swimming. We have recently published a paper [54] using the mathematical framework we have developed in section 2.5.

In general, fish generate wakes when moving in the water. The wake of a discontinuous swimmer consists of ring vortices originating from the beats of the tail and a trailing wake that compensates the fish's displacement [66, 70]; see Fig. 3.5. By conservation of angular momentum, ring vortices are stable in incompressible fluids with low viscosity [95, §146], even under natural conditions [70]. In still water stability means: longer than one minute. The lateral drift of these rings is slow and tends to zero so that the wake structure only occupies a confined space [70]. Wake structures can thus serve as underwater traces and allow predators to detect their prey for a period of over a minute [69]. Catfish, for instance, simply track those wakes to locate their targets [120]. Artificially generated vortex rings that pass a fish laterally [21] as well as vortex rings that are part of a von Kármán vortex street [20] cause a neuronal response in the lateral-line system.

3.3.1 Comparison between Modeled and Experimental Data

Ring vortices can be described as vortex tubes with strength $\Gamma = \sigma \, |\omega|$ that is the product of their cross section σ and vorticity $|\omega|$. When a vortex tube becomes

thinner and its vorticity increases proportionally, the velocity field around it remains approximately the same. Thus, we model a vortex tube by a vortex filament that is the limit of a vortex of zero cross section and infinite vorticity so that its original vortex strength remains constant. To calculate the stationary velocity field of the vortex, we can ignore that this sequence of approximations leads to an infinite vortex propagation speed [95, §163]. To determine the time-dependent velocity field, we then simply assume that the vortex propagates with its original speed.

The vortex filament enclose the circular area $\mathcal{S}$. Outside a vortex filament, the flow is irrotational so that a flow potential exists. The flow potential of a vortex ring with normal vector $\mathbf{k} = (k_x, k_y, k_z)$ is [95, §150]

$$\phi_{\mathrm{v}}(\mathbf{x}) = \frac{\Gamma}{4\pi} \iint_{\mathcal{S}} (k_x \partial_{x'} + k_y \partial_{y'} + k_z \partial_{z'}) \frac{1}{|\mathbf{x} - \mathbf{x}'|} \, \mathrm{d}S' , \tag{3.23}$$

with $|\mathbf{x} - \mathbf{x}'| = \sqrt{x - x')^2 + (y - y)^2 + (z - z')^2}$ being the Euclidean norm of the vector difference between the integration variable $\mathbf{x}' \in \mathcal{S}$ and the point of observation $\mathbf{x}$. By convention, $\mathbf{k}$ points in the direction of the flow through the vortex. Comparison with a dipole potential $\nabla |\mathbf{x}|^{-1}$ reveals that ϕ_{v} is equivalent to the potential of a uniform distribution of dipoles lying in $\mathcal{S}$.

The detectors lie on the x- axis. The normal vector of the vortex ring $\mathbf{k}$ makes an angle δ with the x-y, plane while the projection of $\mathbf{k}$ in the x-y plane makes an angle γ with the z axis. For $\gamma = \delta = 0$, the normal vector points in positive x direction. Experimentally, the presentation of vortices was limited to vortexes passing the trunk of a fish laterally. Thus, here we just consider a vortex ring with normal vector, $\boldsymbol{k} = k_x$, then (3.23) becomes

$$\phi_{\mathrm{x}}(\mathbf{x}) = \frac{\Gamma}{4\pi} \iint_{\mathcal{S}} \partial_{x'} \frac{1}{|\mathbf{x} - \mathbf{x}'|} \, \mathrm{d}y' \, \mathrm{d}z' . \tag{3.24}$$

The propagation speed of a vortex in a fish's wake is slower than under experimental conditions and even tends to zero [70]. However, in the experimental cases the fish is fixed and the vortex ring propagates with slow velocity U in the x-direction. The velocity must be slow in order to avoid some convergence problems, please consult [54]). We then calculate the velocity field at the detector $y = D$ and $v_x = d\phi/dx$. The pressure difference at the pores $\Delta p(x,t)$ is given by applying (3.17). Because of the integral in (3.24), we have made all calculations numerically by using Mathematica. We can see easily that the rate $r(x,t)$ for SN is

$$r(x,t) = In + A * \frac{d\phi}{dx} , \tag{3.25}$$

and for CN

$$r(x,t) = In + A * \frac{d^2\phi}{dxdt} , \qquad (3.26)$$

where, as before, In is the instantaneous firing rate and A a parameter we fit. Then the transfer function for both polarities can be retrieved applying (3.21) (in the + direction), (3.22) (in the − direction).

In an idealized world, all neuromasts would be sensitive to flow parallel to the longest axis of the fish, since in the experiments the fish is fixed and the vortex is produced near the snout. We can expect four different neuronal response patterns: a first pattern for SNs sensitive to water motion in the + direction, a second pattern for SN sensitive in the − direction, a third one for CN sensitive in the + direction and the fourth one for CN sensitive in the − direction. The results presented in Fig. 3.6 show experimentally obtained patterns we can attribute to a SN sensitive in the + direction and a CN sensitive in the − direction. However, since we do not live in an ideal world, we cannot exclude that they come from SNs or CNs with a different axis of sensitivity (see for instance for CN *only* [54]). It was a great surprise for us to see that patterns produced by a pipette near the snout of a fish can be so well explained by this simple theory.
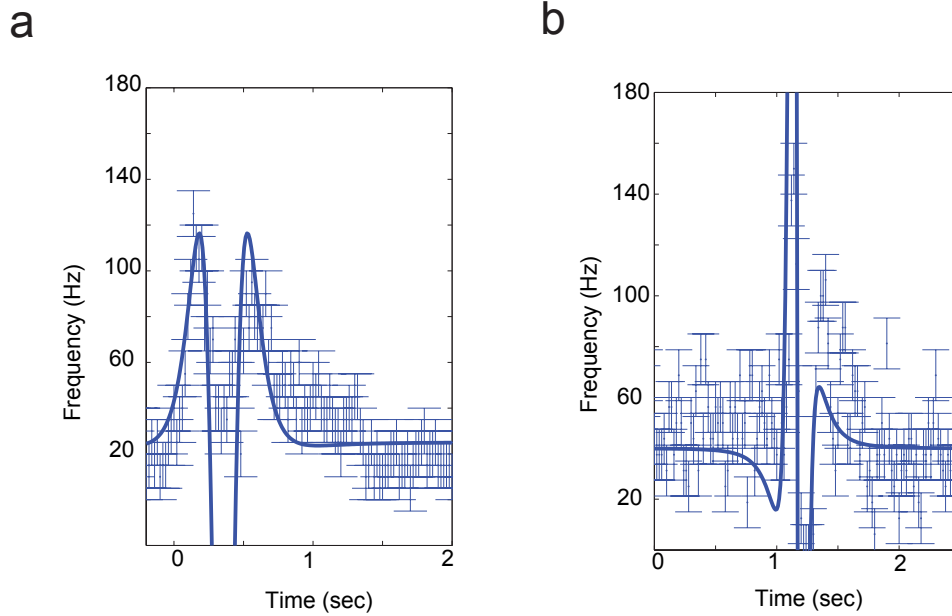
Figure 3.6: *Neuronal response ensuing from a canal neuromast, experimental results. The error bar ± 10 Hz represents time-dependent spike rates of a canal neuromast measured when a vortex with $\gamma \in \{0, \pi\}$ and $\delta = 0$ passed a fixed fish, averaged over ten time runs. As the vortex has approximately constant velocity, the recorded time-dependent data matches the nervous excitation pattern along the lateral line at a specific moment of time.* **a** *Response probably due to a SN fiber sensitive in the $+$ direction with $In = 25$ and $A = 58$.* **b** *Response probably due to a CN fiber sensitive in the $-$ direction with $In = 26.8$ and $A = 1200$.*

4. Response to Noise: Coding at High Precision in the Velocity Regime

Here we will show that SNs encode white noise well and that they are primarily sensitive to velocity. We will also extract the FI curve for SNs and show that over a wide regime they encode the stimulus linearly.

In Chap. 2, we discussed the hypothesis that boundary layer effects can be neglected for both CNs and SNs. For canal neuromasts the pressure within the boundary layer is constant (section 2.2.2). Our recent simulations on stimuli varying slowly in time, where the effect of the boundary layer can be seen as small fluctuations in time, show that the boundary layer does not influence the form of the signal measured at the detectors; see Fig 2.4. For these smooth patterns, the effect of the boundary layer can be neglected. In the present chapter, this result will be extended to the encoding of a white noise stimulus by the peripheral lateral-line system. Our previous study was based on the classical statement that the most efficient stimulus to superficial neuromasts is the velocity at the skin of the fish. Physiological evidence for this has been found and resulted in the assumption that superficial neuromasts function under conditions of low background flow [47] and section 3.1.2 . Moreover, the activity patterns at the afferent nerves are tightly linked to the water velocity profile at the detectors; see Figs 3.3, 3.4 and 3.5. However, a study of Kalmijn [87] has proposed that surface neuromasts are not *exactly* sensitive to velocity but that their response is better explained by a *fractional derivative* of the water velocity outside of the boundary layer. For an introductory text on fractional calculus the

reader is referred to Sokolov [134].

Analytically, we cannot predict what the velocity field within the boundary layer will be. The potential formulation for an ideal fluid does not hold anymore and the viscosity (see Chap. 2) adds a significant dissipative term to the velocity. It is hard to predict what the effect of this term on the behavior of the fluid is. The stimulus pattern, however, might be influenced. Jielof et al [84] were the first to study the biophysics of lateral-line detection, and they already noted a frequency dependency upon the boundary layer. Kalmijn [87] explained it was due to the fact that within the boundary layer the viscous force is not negligible, He made the *ansatz* that the actual form of the velocity field within the boundary layer will be more accurately explained by a fractional derivative of the stimulus motion. As we noted earlier (see section 2.2), the thickness of the boundary is defined as the zone around a cupula where the velocity field is < 99% of the velocity at infinity.

Outside the boundary layer, the inertial force dominates. The thickness of the boundary layer is frequency-dependent: the viscous force does increase faster with the stimulus frequency than the inertial force under the influence of a dipole stimulus. For example, the inertial force increases proportionally to the frequency whereas the viscous force increases with the frequency squared. Thus at low frequencies the cupula is driven by the velocity of the water deep within the boundary layer, which is proportional to a combination of inertial and the viscous forces of water volume. As the frequency increases, the boundary layer becomes thinner and the velocity driving the cupula approaches the velocity of the surrounding water. Since the SNs respond as a low-pass filter (i.e they respond up to a certain intensity and then saturate) to the external velocity, they are likely to encode peripheral stimuli as if they were in a mixed regime of velocity and acceleration.

According to Jielof et al [84], the difference between a purely velocity-driven response and a response due to both the inertial and the viscous force is only reflected in the phase of the response. As we are only interested in the firing rates, we hardly see any effect since the rate is an average computed over a time much longer than one oscillation. It might, however, have an effect on the precise timing of the spikes, and this is what we want to study here. To do so, we apply reverse-correlation using these technique, either the linear reverse correlation approach, or a covariance analysis that is not limited to a single filter. The advantage of the latter is that it does not a priori limit the number of stimuli that a neuron is responsive to. To our knowledge, this is the first study that quantifies the responses of the mechanosensory lateral-line afferents in the framework of an information-theoretical approach.

In this chapter, we will first present the experimental set-up, then we will discuss the relevance of stimulating the afferent with white-noise and how good the encoding

is. We will then discuss and show how we can retrieve the best linear reconstruction for the stimulus. After that, we will discuss the quality of the encoding and show the precision is really high. After this, we will show that the linear-model does not captures all the features of the system, and, therefore, justify the use of a covariant matrix approach. With this approach, we will show that two features are relevant. The first eigenvector can be understood as a velocity and the second as a filter for acceleration. However, we will show that the second feature does not seem to play an important role for spike production, and therefore we will come back to the classical picture that the stimulus to the SNs is $\propto \boldsymbol{v}_{\text{sph.}}$, the velocity of the stimulus, i.e the water outside the boundary layers.

4.1 Experimental Setup

Details regarding animal handling and recording can be found elsewhere[21, 48]. In short, the animals were restrained, anesthetized and fixed in a flow-tank, the posterior lateral line nerve was exposed close to its entry at the brain and single afferents were recorded using high impedance electrodes. The experiments were all performed in Bonn in the laboratory of Prof Horst Bleckmann by Dr . Jacob Engelmann and coworkers.

As hydrodynamic stimuli we used band-passed white noise to drive a vibrating sphere (6 mm diameter), which was placed 5-8 mm laterally to a recorded neuromast and vibrated parallel to the long axis of the fish. Stimuli were either one second in duration and were repeated 100 times (frozen noise), or consisted of 120 s of continuous noise. All stimuli had zero mean amplitude and a linear frequency range between 10 and 150 Hz, based on the power-spectra of the actual sphere-displacement. The stimulus was monitored online, using a gagging sensor (2804 sensor, 4810 amplifier, AD Technologies).Because of the non-linearity of the shaker used to drive the sphere, stimuli were adjusted to maintain a flat power spectrum between 10 and 150 Hz. Only cells with stable firing rates were analyzed.

Data of 33 afferents of 5 goldfish are included in this account. The majority of the afferents (19) were stimulated with frozen noise stimuli at 2 or 3 different amplitudes (0, -10 and -20 dB) and different cut-off frequencies. With the exception of the lowest intensity stimulation (-20 dB), afferents normally responded to the stimulus with an increase in discharge rate.

4.2 Encoding White Noise

The question we want to answer here is if the neuromasts in their spiking activity respond more to the velocity parallel to the greatest of the cupula $v_{\parallel} \propto \boldsymbol{v}_{\text{sph.}} \cdot \boldsymbol{n}$,

where $\boldsymbol{n}$ is the direction of the greatest axis of the cupula and $\boldsymbol{v}_{\text{sph.}}$ is the derivative of the position of the sphere $\boldsymbol{v}_{\text{sph.}} = d\boldsymbol{x}_{\text{sph.}}/dt$ or to some fractional derivative of order $1 < \alpha < 2$? The reader should note that $\alpha = 2$ is the acceleration of the sphere.

White noise stimuli, if the precision permits to encode them reliably, are interesting since they can easily be reconstructed. Most of the statistical methods are, however, based on the assumption that the transfer function between the stimulus and the spike response is linear. The effect of the non-linear term will be discussed in Sect. 4.5 and 4.6. The great advantage of white noise is, providing the linearity assumption holds, and the average of the stimulus is zero the Wiener expansion reduces exactly to the first Wiener kernel. The first Wiener kernel (for the linear assumption) can easily be computed, since in this case, the power spectrum (distribution of the frequency in the stimulus) of the noise will be constant in the frequency space and therefore its power spectrum will be flat. The reverse correlation will be of the form $R_{\text{ss}}(\tau) = \sigma^2 \delta(\tau)$. For a complete description of the computation of the *best* linear filter the reader is referred to [15, 60, 123] and Sec. 4.3. This holds even if the power spectrum is not completely flat (white noise with a cutting off frequency) [79]. The *filter* gives us the type of transformation (first derivative, second derivative, etc) needed to pass from the stimulus to the response. Its geometry therefore characterizes the feature of the stimulus that the neural response is sensitive to.

An exemplary response to frozen noise is shown in Fig. 4.1 a at the top. In all units recorded, the responses were highly reproducible. This was evaluated based on the spike-train synchrony [90] for 10 repetitions of the frozen noise, i.e., by computing the mean interspike interval (ISI) distance for all 90 pairs of spike trains.

In order to do so, we have to take the discrete series of spikes (each spike being a δ function)

$$S(t) = \sum_{i=1}^{M} \delta(t - t_i) \tag{4.1}$$

with t_1 to t_M denoting the series of time where the neuron spikes and M being the number of spikes, leading for each spike train to a series of 1 and 0, 1 denoting a spike at time t and 0 denoting no spike at time t.

To obtain a time-resolved measure of the firing rate of the spike trains $\{t_i^x\}$, we proceed as follows: the value of the current interspike interval is assigned to each time step,

$$x_{\text{ISI}}(t) = \min(t_i^x | t_i^x > t) - \max(t_i^x | t_i^x < t) \tag{4.2}$$

where $\min(t_i^x | t_i^x > t)$ is the time to the next spike and $\max(t_i^x | t_i^x < t)$ is the time before the previous spike, (ISI refers to the interspike interval). We then calculate it

for other spike trains $\{t_j^y\}$ (in order to compare). Second, the ratio between $x_{\text{ISI}}(t)$ and $y_{\text{ISI}}(t)$ is taken (in practice this is done only after every new spike in either time series) and the final measure is obtained after introducing a suitable normalization so as to obtain

$$
I(t) = \begin{cases} \frac{x_{\text{ISI}}(t)}{y_{\text{ISI}}(t)} - 1 & \text{if } x_{\text{ISI}} \le y_{\text{ISI}}(t) \\ -\left(\frac{y_{\text{ISI}}(t)}{x_{\text{ISI}}(t)} - 1\right) & \text{else}. \end{cases} \tag{4.3}
$$

For a graphical example, the reader is referred to Fig. 4.1 b. The measure becomes zero in the case of two identical spike trains and approaches 1 and -1, respectively, if the firing rate of the first (or second) train is big and the other small; see (4.3).

This value of $I(t)$ is calculated for every spike in every spike train, in order to discretize the function $I(t)$. The ISI distance between two spike trains is then evaluated as

$$
D_I^s = \sum_{i=1}^{M} |I(t_i)|. \tag{4.4}
$$

In order to get the variability of spike trains, we average this value for every trial and every spikes train. We then apply an analysis of variance (ANOVA-test) to the synchrony values obtained from the population of afferents under different stimulus conditions. Statistical analysis (SPSS version 12 and Matlab) is based on paired or unpaired tests (t-tests, Mann-Whitney U-test and Kruskal-Wallis test), depending on the distribution of the data. Figure 4.1a shows the frozen noise we used for the experiment, the raster plot for 5 consecutive responses to the stimulus and a histogram of the probability of having a spike in a bin of width 0.1 ms averaged over the five trials, Fig. 4.1b shows the interspike intervals and the ratio for two spike trains (top)(4.3). Finally, in Fig 4.1 c we show the averaged ISI-distance given by (4.4).

4.3   Linear Reconstruction of Spike Trains

The activity of a neuron at time t typically depends on the behavior of the stimulus over a period starting a few hundred milliseconds prior to t and ending perhaps 10 msec before. This kind of function can be expanded as a Volterra expansion [79]. For the case we consider, as given in [40], it takes the form of

$$
\begin{aligned}
s_{\text{est}}(t) &= s_0 + \int d\tau\, h(\tau) x(t - \tau) + \int d\tau d\tilde{\tau}\, h_2(\tau, \tilde{\tau}) x(t - \tau) x(t - \tilde{\tau}) \\
&\quad + \int d\tau d\tilde{\tau} d\widetilde{\tau}\, h_3(\tau, \tilde{\tau}, \widetilde{\tau}) x(t - \tau) x(t - \tilde{\tau}) x(t - \widetilde{\tau}) + \dots
\end{aligned} \tag{4.5}
$$
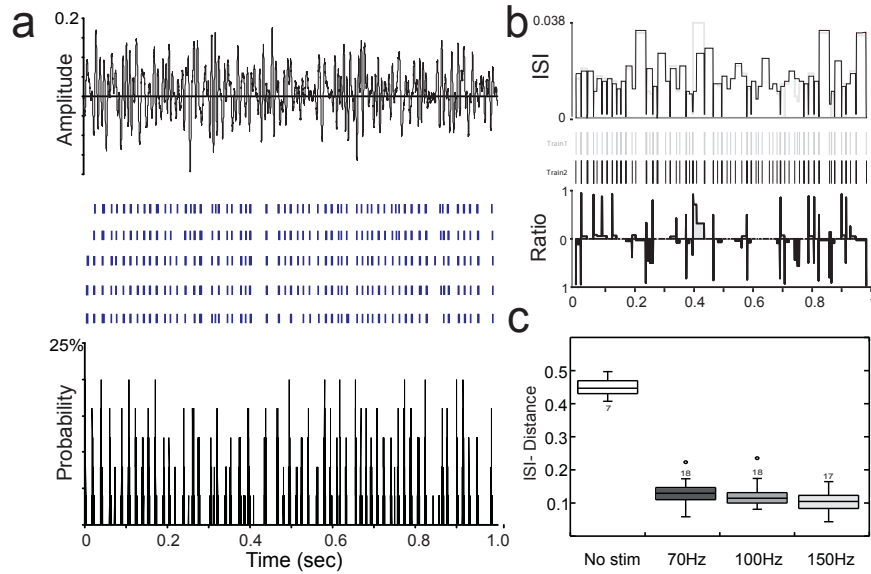
Figure 4.1: **a** *Response to a 1 second section of frozen noise is highly reproducible, as can be seen in the raster (middle) showing 5 consecutive responses to the stimulus (top) and the histogram (bottom, bin width 0.1 ms) of 10 consecutive responses.* **b** *ISI (interspikes interval)in response to two repetitions of the frozen noise presented in* **a***. The plot on the top is the interspike interval after each spike as given by (4.2) and the bottom figure represents the ratio as given by (4.3).* **c** *Mean variability (10 repetitions, 90 inter-trial combinations; see main text) obtained for the three cut-off frequencies (the power spectrum of the noise is roughly flat up to that frequency) and for ongoing activity. We note that variability was very low, indicating tightly locked responses from trial to trial. Spike-train synchrony of the response to the frozen noise was investigated based on a method introduced by Kreuz et al [90]. In consideration of the determination of variability between different spike trains, at all cut-off frequencies, spike train variability was significantly lower than spontaneous variability as indicated by the asterisks above the horizontal lines (LSD post-hoc test, $p < 0.05$).*

For causality reasons, the integral can be restricted to the positive domain of the function h, h being symmetric in τ. Wiener reformulated the Volterra expansion in such way that all terms were independent from each other by orthogonalizing them [79] Sect. 1 and 2. Since the stimulus is white noise, the average value of all odd-order correlations is zero, and the two-point correlation function takes the form

$$\langle x(t)x(t')\rangle = S_x \delta(t - t') \,. \tag{4.6}$$

Removing all the correlation between the terms the Wiener expansion takes the form (for Gaussian white noise)

$$y(t) = G_0 + G_1[x(t)] + G_2[x(t)] + G_3[x(t)] + \dots \tag{4.7}$$

where the individual terms of the expansion are given by [123] as

$$G_0 = 0 \tag{4.8}$$

$$G_1[x(t)] = \int_0^\infty d\tau_1 g_1(\tau_1) x(t - \tau_1) \tag{4.9}$$

$$G_2[x(t)] = \int_0^\infty d\tau_1 \int_0^\infty d\tau_2 g_2(\tau_1, \tau_2) x(t - \tau_1) x(t - \tau_2)$$
$$- S_x \int_0^\infty d\tau g_2(\tau, \tau) \tag{4.10}$$

$$G_3[x(t)] = \int_0^\infty d\tau_1 \int_0^\infty d\tau_2 \int_0^\infty d\tau_3 g_3(\tau_1, \tau_2, \tau_3)$$
$$\times x(t - \tau_1) x(t - \tau_2) x(t - \tau_3)$$
$$- 3S_x \int_0^\infty d\tau_1 \int_0^\infty d\tau_1 d\tau_2 g_3(\tau_1, \tau_1, \tau_2) \,. \tag{4.11}$$

The g_i are the Wiener kernel, the coefficient of the expansion, and are the only function of the time delays τ_i [123]. Since we make the assumption that the stimulus is white noise in this case, all frequencies are independent and (theoretically) the stimulus reconstruction based on the linear filter can be used to obtain a linear estimation of the reconstruction for the stimulus. We can then evaluate each term alone and in the case of Gaussian white noise, only the term $G_1[x(t)]$ does not vanish and it can be shown that [15, 123]

$$g_1(\tau) = \frac{\bar{r}}{S}\langle s(t_i - \tau)\rangle \,, \tag{4.12}$$

where $\bar{r}$ is the average firing rate of the neuron, S the power spectrum of the stimulus and s the firing train generating a spike (averaged over all samples of spikes). This term is often called the *spike triggered average* (STA). White-noise average is denoted by angular brackets $< \dots >$. That is the theory, in case of a noise *completely* white

(no frequency dependence). In the experiment, however, we use a band-pass white noise i.e., a noise that has a flat power spectrum up to an arbitrary cutoff frequency, [61, 142]. We now proceed as follows.

First, we subtract from the spike train the mean instantaneous firing rate (probability having one spike in a bin) and from the stimulus its mean value and define the spike train and the stimulus (with zero mean) as

$$x(t) = \sum_i \delta(t - t_i) - x_0 \qquad s(t) = s_0(t) - s_0 \qquad (4.13)$$

where x_0 is the mean instantaneous firing rate and s_0 the mean of the stimulus. We define the auto-correlation and cross-correlation function between the spike train and the stimulus by

$$R_{ss}(\tau) = \langle s(t)s(t+\tau) \rangle, \qquad (4.14)$$
$$R_{xx}(\tau) = \langle x(t)x(t+\tau) \rangle, \qquad (4.15)$$
$$R_{sx}(\tau) = \langle s(t)x(t+\tau) \rangle. \qquad (4.16)$$

A linear estimation of the spike train is therefore

$$s_{\text{est}}(t) = \int_{-\infty}^{\infty} d\tau \, h(\tau)x(t - \tau) \qquad (4.17)$$

for a square integrable function h. The filter h is chosen in such a way as to minimize the mean square error between the stimulus $s(t)$ and the estimate $s_{est}(t)$

$$\epsilon^2 = \frac{1}{T} \int_0^T dt[s(t) - s_{\text{est}}(t)] \qquad (4.18)$$

where T is the duration of the stimulation. The orthogonality principle implies that the optimal filter h satisfies the equation

$$R_{sx}(\tau) = (h \star R_{xx})(-\tau). \qquad (4.19)$$

This equation is solved through the Fourier transformation of h defined by

$$\hat{h}(\omega) = \int_{-\infty}^{+\infty} d\tau h(\tau) \exp(i\omega t) \qquad h(\tau) = \frac{1}{2\pi} \int_{-\infty}^{\infty} d\omega \hat{h}(\omega) \exp(-i\omega t). \qquad (4.20)$$

The Fourier transform of the autocorrelation and cross correlation function is $S_{ss}(\omega) = \hat{R}_{ss}(\omega)$, $S_{xx}(\omega) = \hat{R}_{xx}(\omega)$ and $S_{sx}(\omega) = \hat{R}_{sx}(\omega)$. We assume that the stimulus is bandwidth limited, i.e. that is $S_{ss}(\omega) = 0$ for $|\omega| \geq \omega_c$ where $\omega_c = 2\pi f_c$ is the cut-off frequency ($f_c = 70$, 100 or 150 Hz in the experiments). We assume the Fourier transform of the auto-correlation and the cross-correlation functions to be positive
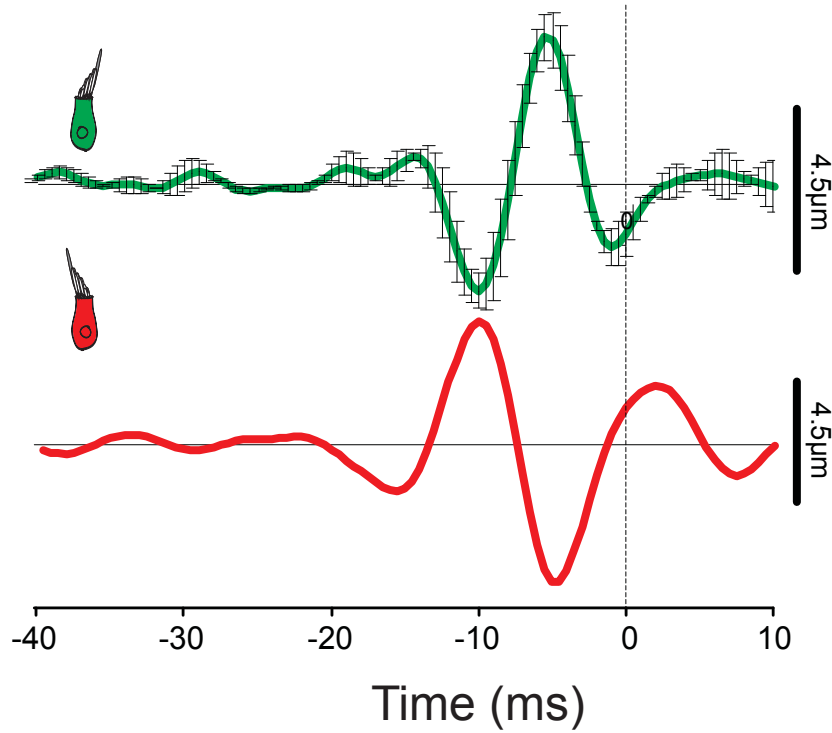
Figure 4.2: *Examples of 1-st order Wiener-kernels obtained from white-noise input in conjunction with appropriate averaging [60]. Due to directional sensitivity of the hair-cells, two opposite filters has been recovered. Error-bars indicates standard deviation.*

within the bandwidth of the noise [60]. By applying (4.19), we find that the optimal filter h in Fourier space is

$$\hat{h}(\omega) = \begin{cases} \frac{S_{sx}(-\omega)}{S_{xx}(\omega)} & -\omega_c \leq \omega \leq \omega_c \\ 0 & \text{else} \, . \end{cases} \tag{4.21}$$

The best linear filter, therefore, takes the form

$$h(t) = \int_{-f_c}^{f_c} df \frac{S_{sx}(-f)}{S_{xx}(f)} \exp\left(-2i\omega ft\right) . \tag{4.22}$$

All Fourier transforms are obtained using Bartlett windowing (256.0 ms window), see Matlab user guide. This filter accounts for both the statistics of the stimulus and the spike train. The quality of the reconstruction obtained by convolving the spike train with this filter was assessed based on the signal-to-noise measure [97]. Figure 4.2 shows the 1st-order Wiener kernels obtained. As expected for lateral-line

afferents, we have found two biphasic kernels, one being roughly the negative of the other. This reflects the presence of the two *oppositely* tuned populations of haircells within each neuromast. The *bi*phasic shape of the kernels is similar to what has been reported for several sensory systems [67, 142] so far and is normally associated with a velocity filter. This interpretation is based on the shape of the obtained filter: it resembles two delta functions of opposite sign, which will transform a stimulus in such a way that the result represents the velocity in the original stimulus as a function of time (the filter will approximate the first-derivative of the stimulus).

The noise containing the reconstruction is defined as $n(t) = s_{\mathrm{est}}(t) - s(t)$, where $S_{nn}(f)$ denotes the power spectrum of the noise and $S_{ss}(f)$ the power spectrum of the stimulus. The signal to noise ratio (SNR) is defined as

$$\mathrm{SNR}(f) = \frac{S_{\mathrm{ss}}(f)}{S_{\mathrm{nn}}(f)} \, . \tag{4.23}$$

Thus, the SNR is a measure of the amount of signal power present at a given frequency relative to the noise containing the reconstructions. No correlation between the stimulus and the reconstruction results in SNR = 1 for all frequencies, while correlations result in $\mathrm{SNR}(f) > 1$. The least-square error of the reconstruction takes the form

$$\epsilon^2 = \int_{-f_c}^{f_c} df \frac{S_{\mathrm{ss}}(f)}{\mathrm{SNR}(f)} \tag{4.24}$$

and assumes its maximal value for $\epsilon^2 = \sigma^2$, σ being the standard deviation of the stimulus itself when $\mathrm{SNR}(f) = 1$. The coding fraction is defined as

$$\gamma = 1 - \frac{\epsilon}{\sigma} \tag{4.25}$$

with ϵ^2 being the mean square error of the reconstruction and σ the standard deviation in the stimulus as a normalized measure, ranging between 0 when the reconstruction is not better than chance and 1 (when the reconstruction explains all the standard deviations of the stimulus).

4.4 Time or Rate Coding?

So far, our data have shown that SN afferents transmit information over a wide frequency range reliably; see Fig. 4.1. To address the issue of whether the afferents transmit information based on a rate code or a temporal code in which at least part of the information embedded in a spike train is contained in the timing of the spikes, we have compared the coding fraction obtained using the original spike trains to that obtained after a defined spike-time jitter was introduced [85, 125];
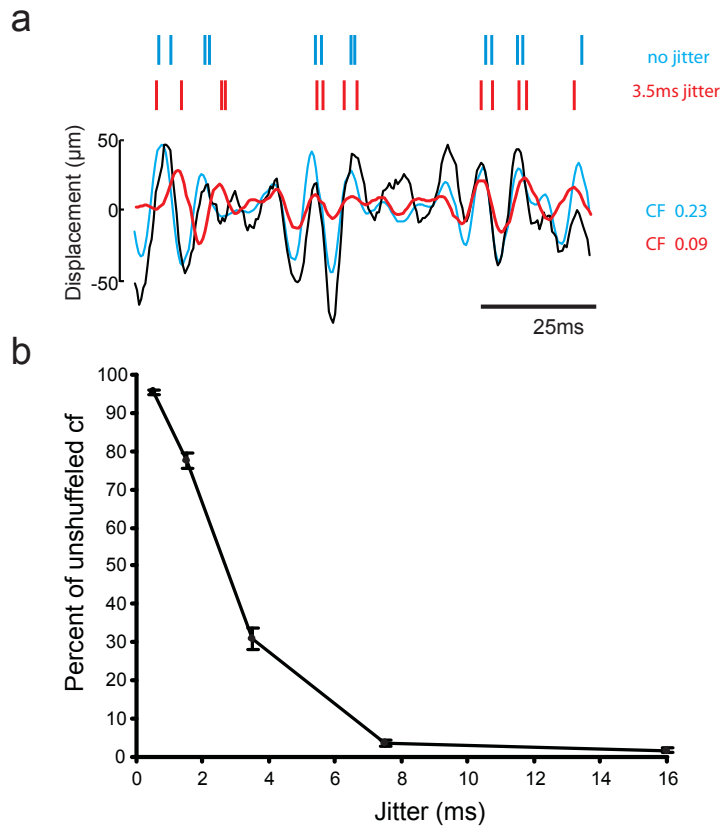
Figure 4.3: **a** *Exemplary original spike train (top) and the same train after a jitter (random Gaussian distribution with a mean of 3.5 ms) was applied (middle). The three traces at the bottom show the actual stimulus driving the neuronal response (black), the reconstructed stimulus based on the original spike train (blue) and the reconstruction based on the jittered spike train (red).* **b** *Mean effect of the introduction of spike-time jitter (coding fraction) on the stimulus reconstruction. Data are normalized with respect to the reconstruction quality obtained by using the original (un-jittered) spike train.*

see Fig. 4.3. Increasing the amount of jitter, we found a strong decrease in the stimulus reconstruction, as can be seen in the coding fraction cf. Fig. 4.3. The introduction of a mean jitter of 3.5 ms to the spike train was sufficient to reduce stimulus reconstruction by 70%. The introduction of spike-time jitter of similar time scale as the cut-off frequency of the stimulus resulted in a complete failure to reconstruct the stimulus. Thus, the temporal precision of the spikes is higher than the shortest timescale contained in the stimulus, reflecting the presence of a temporal code and hence the need for a high temporal precision in the primary afferents [40].

Figure 4.3 indicates that the detectors can encode fast changes in the stimulus. However, for a classical translating sphere, the change in the stimulus over such a short time scale will be rather moderate. We can therefore, expect that the effect of jitter will be moderate and that probably to produce any modification on the measured spike pattern unless we use a really large time jitter is low. However, these data here clearly show that neuromasts are extremely precise and can encode really fast change in the stimulus. The reliability combining a precise time-encoding is similar to the result of Mainen and Sejnowsky [99] and permits us to conclude that since the spike train are highly reproducible (the stochasticity due to the spike production can be neglected). Since the timing precision is high, the *instantaneous* probability of having a spike at a certain time can describe the firing pattern accurately.

4.5 Linearity of the Reconstruction

A question arises here: how good is a linear model to explain the reconstruction of the stimulus? How good is the *ansatz* that a linear reconstruction of the stimulus explains the behavior of the neuromast? Does the linear model really capture the essential features of the response or do we need something better? In order to quantify whether a single feature (velocity) of the stimulus is sufficient to explain the neuronal responses of superficial neuromasts, we have employed a general method originally introduced by Roddey et al. [124], which measures the performance of the optimal linear model with respect to the optimal performance theoretically achievable. In the previous section, we defined the error in the stimulus reconstruction as the part that can be reproduced by a linear reconstruction. Even the *best* non-linear model cannot reconstruct all from the stimulus since a certain part of it is noise. In reality, it is better to say that the stimulus is: stimulus = linear reconstruction + non-linear contribution + noise. The non-linear contribution term represents the part of the stimulus that can be explained by the best *non-linear* model, whereas the *noise* is a term that can be explained by any model on earth. It is true noise. What we try to achieve is a measure of how much of the theoretically achievable reconstruction is achieved by the minimal model, i.e.,

$$\text{Linearity} = \frac{\text{linear reconstruction}}{\text{linear reconstruction} + \text{non-linear contribution}} . \tag{4.26}$$

The signal-response coherence can be used to quantify the performance of the optimal linear model, while the response-response coherence gives an upper boundary to the performance of the optimal nonlinear model. Signal-response (SR) coherence,

in our case, was calculated over four stimulus repetitions and is given by [19, 124]

$$C_{\mathrm{SR}(f)} = \frac{\left| \frac{1}{4} \sum_{i=1}^{4} SR_i(f) \right|^2}{\frac{SS(f)}{4} \sum_{i=1}^{4} RR_i(f)} \tag{4.27}$$

and the response-response (RR) coherence is given by

$$C_{\mathrm{RR}(f)} = \frac{\left| \frac{1}{6} \sum_{i=1}^{4} \sum_{j<i} RR_{ij}(f) \right|^2}{\left[\frac{1}{4} \sum_{i=1}^{4} , RR_i(f) \right]^2} \tag{4.28}$$

where R_{ij} is the cross-spectrum (defined as the forward Fourier transform of the cross-correlation function 4.14) between the spike trains R_i and R_j.

A comparison between the signal-response coherence and the square root of the response-response coherence will thus quantify the performance of the best linear model with respect to the optimum performance theoretically achievable. Under the assumption that the first term of the Volterra series, and thus the first Wiener kernel, describes the stimulus-response transformation sufficiently well, we expect that the SR and the square root of the RR should closely resemble each other. This resemblance was quantified by the performance index $100 \times C_{\mathrm{RS}(f)}/\sqrt{C_{\mathrm{RS}(f)}}$, see [19, 124]. SR and RR were computed for four presentations of frozen noise.

In our case, both the response-response (RR) and signal-response (SR) coherence functions indicate that the system functions as a high-pass filter. The linear performance index (mean ratio SR/RR from 0 to 150 Hz) was 70.7 ± 13.5 ($n = 21$). This indicates that the optimal linear encoding model could capture 2/3 of the possible information contained in the spike train (Fig. 4.4). This is an idealized approximation, since this analysis is based on the comparison between the voltage driving the sphere and the neuronal response. Since the vibrator driving the sphere motion constitutes a high pass filter in itself, we expect a lower performance in the frequency range below 50 Hz, and hence it seems reasonable to investigate how well a linear model conveys information as compared to a model taking into account the effect of the non-linearity (see below). Calculating the frequency-specific coherence based on the reconstructed stimulus and the actually measured sphere displacement shows that the superficial neuromasts do respond to frequencies well above 100 Hz, including frequencies beyond the cut-off frequency of 150 Hz. Because of the steep
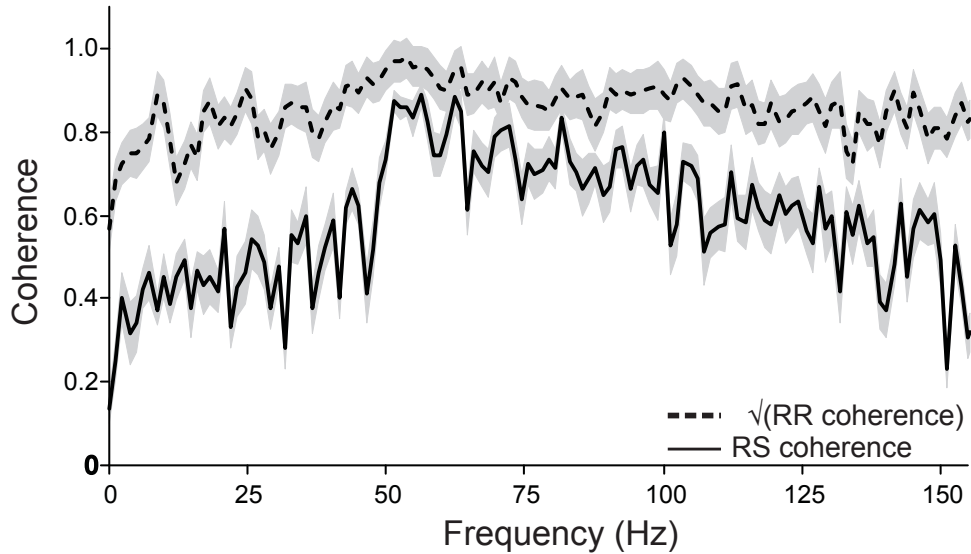
Figure 4.4: *Mean signal-response (solid line) and response-response (dashed line) coherence functions $(n = 21)$ for frozen noise stimulus. Signal-response coherence was high for a frequency range between 50 to at least 150 Hz and showed high-pass characteristics. Response-response coherence as a measure of the internal noise of the encoding was extremely high at all frequencies. The area between both functions indicates the amount of information not recovered by the optimal linear model achievable. Within $0 - 150$ Hz (the bandwidth of our stimulus), this is 30%. Grey-shaded areas give the standard-deviation errors of both functions*

attenuation at higher frequencies, theses frequencies could not be tested with the current setup. Nonetheless, these data show that superficial neuromasts are high-pass filters, which indicates that they respond to relatively fast signals, i.e. the velocity. the acceleration or a fractional derivative inbetween, of the surrounding water.

4.6 Estimating Nonlinearity Using a Covariance Matrix Analysis

As we show in Fig. 4.4, the spike triggered-average (STA) does not explain all the variance of the spikes we can theoretically retrieve, and the good agreement we show for the linear estimation probably overestimates the reality *somewhat*. It is therefore interesting to design a second set of experiments, where the afferent are stimulated by means of a continuous noise. Rather than a priori testing for only one best linear filter, we have used the covariance approach [14], which allows one to

directly illustrate which features of the stimulus give rise to a spike and if there is more than one such feature in the stimulus.

To determine which features contained in our stimuli are causing the afferents to fire, we have used a method based on the eigenvectors and eigenvalues of the covariance matrix of the spikes. This method, proposed by Brenner et al. [14], is based on the application of the principal component analysis (PCA) [43, 118] to the matrix representing the fluctuation around the average as defined by de Ruyter et al [137].

In order to construct the covariance matrix, the experimental collaborators in Bonn recorded the occurrence time $\tau(t_{spike})$ of every spike and selected the stimulus history *before* each spike, $S(\tau) = S(t_{spike} - \tau)$. From that, they calculated the spike-triggered average (STA) by averaging all stimulus histories $S(\tau)$. Next the covariance matrix of the fluctuations around the average as defined by Brenner et al [14] was computed,

$$
\begin{aligned}
C_{\mathrm{spike}}(\tau, \tau') &= \langle s(t_{\mathrm{spike}} - \tau) \cdot s(t_{\mathrm{spike}} - \tau')\rangle \\
&\quad - \langle s(t_{\mathrm{spike}} - \tau)\rangle \cdot \langle s(t_{\mathrm{spike}} - \tau')\rangle \\
&= C_{\mathrm{Prior}}(\tau, \tau') + \Delta C(\tau, \tau'),
\end{aligned}
\tag{4.29}
$$

where $C_{\mathrm{Prior}}(\tau, \tau') = \langle s(t_{\mathrm{spike}} - \tau)\rangle \cdot \langle s(t_{\mathrm{spike}} - \tau')\rangle$ is the covariance matrix of the stimulus itself and the latter equality defines the matrix $\Delta C(\tau, \tau')$.

To resolve which features of the Gaussian stimulus relate to the spiking of the afferents, the distribution of stimuli not related to spiking (called the prior distribution) was subtracted [14] from the covariance matrix $\Delta C(\tau, \tau') = C_{\mathrm{spike}} - C_{\mathrm{prior}}$. This approach reveals stimulus features where the variance is altered in comparison to the prior.

Following diagonalization of ΔC, the eigenvalues were used to estimate the relevance of the 200 eigenvectors obtained. Since we subtracted the prior stimulus distribution from the covariance matrix,all the eigenvalues near zero correspond to an eigenvector for which the variance is not different from the total stimulus variance. Hence, such eigenvectors (we use the term *feature* synonymously) do not relevantly contribute to the spiking process. The relative importance of the eigenvectors was investigated based on their eigenvalues. Eigenvalues measure the variance difference of each eigenvector with respect to the prior distribution.

The importance of the features was evaluated based on their eigenvalues. Since the first two eigenvectors account for 84% of the total variance (see Fig. 4.5), we restrict our presentation to these two most prominent eigenvectors. In all cells, the
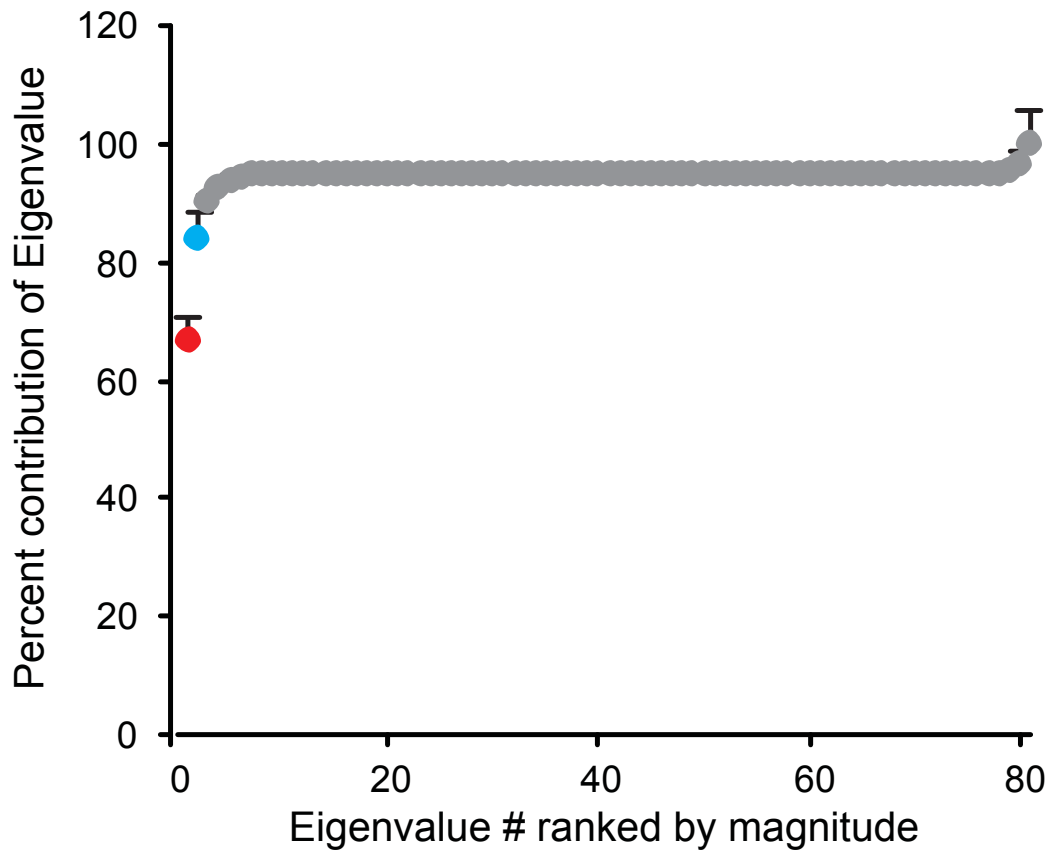
Figure 4.5: *Cumulative contribution of the eigenvalues. The first two eigenvalues on average account for 84% of the variance of the response of the afferent. Error bars have been indicated.*

eigenvector of highest eigenvalue was very similar to the STA (see inset in Fig. 4.6). In the few cases where a second eigenvector of strong eigenvalue was recovered ($n = 3$), this second feature always resembled the first derivative of the STA (Fig. 4.6c, f).
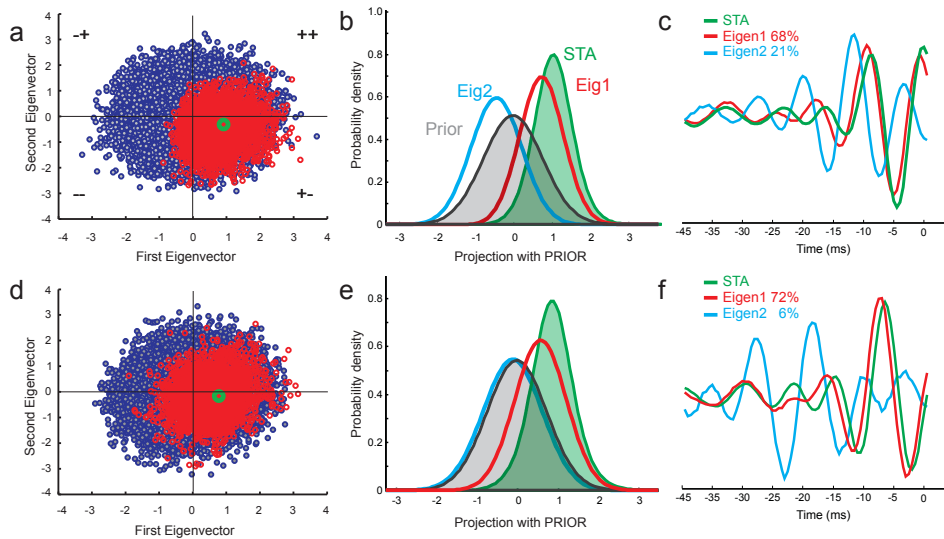
Figure 4.6: **a-f** *Example of the two dominant responses found by the eigenvector analysis. Afferents either showed a single dominant contribution to the spiking that was characterized by one eigenvector similar to the spike triggered average) STA (bottom row), or by two eigenvectors of significant contribution (top row). In the latter case, the first eigenvector resembled the STA, while the second eigenvector resembled the first derivative of the STA.* **a** *and* **d** *Scatter plot of the projection of the first and second eigenvector on the spike timing ensemble (STE) distribution (red dots). Each dot represents the x- and y-coordinate obtained from the dot-product of the stimulus preceding a spike with the first and second eigenvector. The blue circles represent the projection of the prior distribution with the first two eigenvectors, and the small green circle shows the projection between the STA and the eigenvectors.* **b** *and* **e** *Probability distribution of the STE projected onto the STA (green) and the first two eigenvectors (red and blue).* **c** *and* **f** *Comparison of the STA (green) to the two eigenvectors. Color code as in* **b** *and* **e**. *The relative contribution strength of eigenvectors one and two is indicated in the legend.*

4.7 Extraction of the FI Function

In this section, we want to extract FI (firing frequency of the afferents function of the intensity of the stimulus) based on the instantaneous firing rate from the spike-triggered average (STA). To relate the STA as well as eigenvectors to the input-output relation of the afferents, we have estimated the probability of spiking, $P(\text{spike})$, related to the similarity of the stimulus to a given feature (STA, eigenvector). Similarity of the actual stimuli to the features was measured by the linear projection of feature and stimulus. Throughout what follows we define for two stochastic events A and B, the *conditional* probability $P(A|B) = P(AB)/P(B)$ to be the probability of A *given* that B occurs as well; hence $P(B) > 0$. The conditional probabilities $P(\text{spike}|\text{stimulus})$ were derived from the spike-triggered ensemble projected onto the STA $P(\text{STA}|\text{stimulus})$ and for the joint projection $P(E_1|\text{stimulus})$ of the first eigenvector E_1. In order to do so, one has to use

$$P(\text{spikes}|\text{stimulus}) = \frac{P(\text{stimulus}|\text{spike}) \times P(\text{spikes})}{P(\text{stimulus})} \, . \tag{4.30}$$

The FI function is then constructed in the following way explained *in extenso* elsewhere [14, 67, 133].

- First, we take the stimulus vector (SV). The stimulus has to have a 0-mean in order to work properly. We segregate the stimulus in bins of 5 ms. We then keep 40 ms for the analysis. These vectors constitute our STE (spike timing ensemble).

- Then we take the dot product of SV with E_1 or the STA. This is a measure of the similarity between both vectors (see Fig. 4.7a in blue STE with E_1 in red with STA). The dot product between the STA and E_1 is on average about 0.8 meaning that the STA is really similar to E_1.

- Then we bin theses values to get a probability distribution $P(S|\text{spike})$ conditioned on the occurrence of a spike.

- To normalize the distributions, we have to multiply the values obtained in the last step by the probability $P(\text{spike})$ (4.30). This probability is equal to the probability of having a spike over the complete time. The normalized curves are shown in Fig 4.7.

- Then we take a random stimulus vector of the same duration and construct the dot product of theses vectors with E_1 or STA. In our case, we took all segments that did not start with a spike and defined this group of vectors as the prior. We checked that the distribution was altered when we chose the vector randomly.

- We take the dot product of these vectors (not conditioned on spikes) with E_1 or the STA.

- This gives us the similarity (S) of all parts of the vector.

- Bin these S values to get a probability distribution P(S). P(S) is the probability distribution of how similar the stimulus vectors are to E_1 or to the STA. The comparison between the prior and the STA is given in black in Fig 4.7a and b.

- By applying the Bayes theorem (4.30) we can then find the FI function. The FI function obtained this way is presented for one cell in Fig. 4.7 c and on average in Fig. 4.8.

The great advantage of the method we present here is to extract the FI function for the afferents from a stimulus varying rapidly so that we can avoid any effect on the distribution due to adaptation at the detector level. It is interesting to see (in Fig 4.8) that the FI function we obtain is linear over a really great range (the data were fit from SD 0 to 3). The physical meaning of the x-axis,i.e.,its dimension, is not intuitively clear, though. In all publications where this method has been applied [14, 67, 133] it is given in units of the standard deviation of the prior (meaning standard deviation of the stimulus). If the firing response of the afferent increases linearly with the intensity of the stimulus we can assume that the scaling between the standard deviation of the prior and the stimulus intensity (the displacement of the sphere) is linear. We have decided to present our FI-function in terms of the standard deviation of the prior and extend the relation between this measure and the stimulus amplitude to the text. In this way, we avoid potential errors that occur if some non-linearity is present in the distribution of the sphere displacement.

4.8 Conclusion

In this chapter we have shown that neuromasts can follow a white noise stimulus in a precise manner (Fig. 4.1) and can even act as a single spike encoder (Fig. 4.3). We then applied a Wiener reconstruction technique and showed that the linear filter is a *velocity* filter (Fig. 4.2). We have also shown that the linear model is fairly good for explaining the spike production at the afferent nerve (Fig. 4.4). Using a covariance matrix approach, we extracted the important non-linear feature and showed that only the first two eigenvectors seem to have a significant effect on spike production (Fig. 4.5). The first eigenvector has the shape we expect for a velocity filter, whereas the second eigenvector has the shape of an acceleration filter (Fig. 4.6). However, the contribution of the second eigenvector on spike production seems to be rather moderate; see for instance Figs. 4.6b and e, where we cannot really see the role of this eigenvector in spike generation.

Moreover, the coherence (Fig. 4.4) does not show the frequency dependency that Kalmijn [87] proposed. In fact, in Fig 4.4 we see that the best non-linear model $\sqrt{RR}$
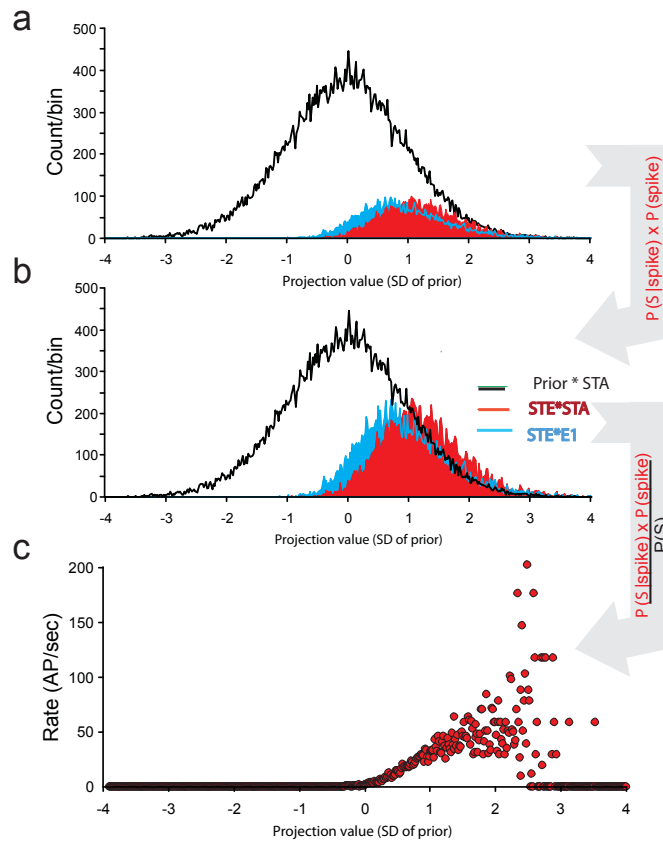
Figure 4.7: *Construction of FI (firing-rate function of the stimulus intensify) functions.* **a** *The distribution of the dot-product values obtained between the stimulus segments (40ms length) not conditioned in spiking (prior) with the spike triggered average (STA) is shown in red. The values we have obtained show a measure of similarity to the STA and are scaled in units of standard deviation of the distribution. The bin width for all distributions shown is set to 5-percent of standard deviation/bin. We note that this Prior distribution is Gaussian with zero mean. Similarly treated distributions for the dot-product values between the stimulus segments preceding spiking (spike-triggered ensemble) and the STA (red) and the dominant first eigenvector (blue) are shown as well. We note the high degree of overlap between both distributions.* **b** *Same as in A following a normalization of the distributions conditioned on the spikes in such a way that each bin is multiplied by this probability (see formula on right-hand side).* **c** *Construction of an FI-like relation based on the ratio between the prior distribution and the distribution conditioned on spiking. In the example shown, the STA distribution was used and a fairly similar linear FI would have been obtained using the E_1 distribution. This FI function relates the probability distribution of the prior to the conditioned distribution. Thereby we obtain a measure of how much spiking of the cell is increased/decreased with respect to the probability distribution of the prior.*
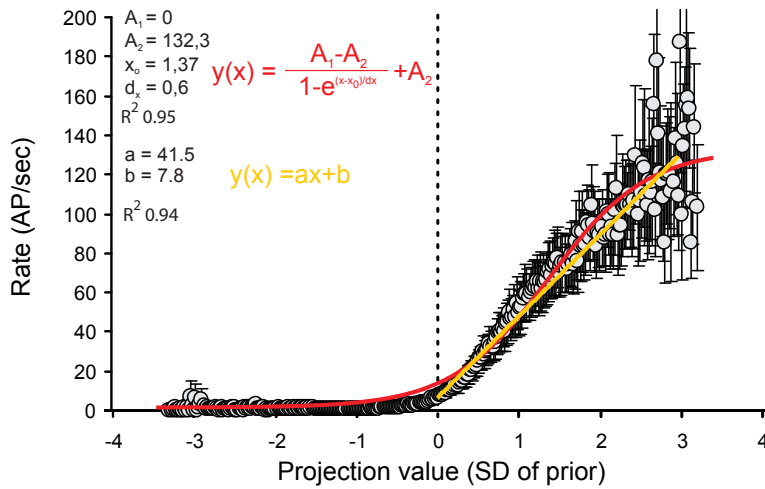
Figure 4.8: *Construction of the mean FI (firing rate function of the stimulus intensity) function. We also show that a sigmoidal fit explains well $R^2 = 0.95$, where R^2 is the coefficient of determination, the FI curve. Furthermore, a linear fit explains the data as well as the sigmoidal fit in the linear range of the detectors with $R^2 = 0.94$. It confirms the linear transfer function we use for the firing rate in the rest of this dissertation. As we explain in the text, the x-axis is always expressed in terms of standard deviation of the prior.*

captures about 80 % over the complete range of frequency contained within the white noise. The performance of the best linear model seems to be frequency-dependent and performs best between 50 to 90 Hz and is equally bad for lower or higher frequency; see Fig 4.4. If, however, the frequency dependence proposed by Kalmijn had been true, the performance would have been different. The linear encoding should have performed best to encode the lowest frequencies and failed to explain the higher frequency, since the shape of the STA is similar to what we can expect if the system encodes velocity. It is not what we observe here.

Finally, we have extracted the FI function based on the STA and shown that the firing rate increases linearly with the increase of the frequency of the stimulus, again confirming the assumption used in this thesis that the transfer function between the stimulus intensity and the activity at the afferents can be modeled linearly; see Figs. 4.7 and 4.8.

5. Localization: Determining Distance Perpendicular to the Detectors

In this chapter, we propose a simple mechanism for 3-dimensional (3-D) distance determination based on the width of the stimulation pattern that, as we will show, encodes the distance perpendicular to the detectors. We will show that the cue is robust and is, to a great extent, independent of the form of the fish or the form of the object generating stimulus.

Retina and lateral-line detectors face a similar problem. In both cases, the sensory system faces a two-dimensional image of 3-D reality. The depth must, therefore, be extracted from some cues present in this two-dimensional picture. Hydrodynamic images are, to some extent, comparable to visual images. With increasing distance, images become blurred [98, 115, 116] and this can be used in monocular vision for distance determination. In contrast to visual images, however, hydrodynamic images lack a lens adjusting the focus. Consequently, hydrodynamic images get wider with increasing distance while visual images in fact get smaller as the distance increases.

5.1 Distance Determination by SNs

How can fish determine the position of *small* sources?

Surface neuromasts are most sensitive to the water velocity (change) flowing in

the direction of their primary axis. For a vibrating sphere, the velocity is zero at the two points where fluid motion reverses; see Fig 3.2. For the benefit of the reader, we reproduced this figure here and indicated the distance between the zeros and maxima on this picture, 5.1).

For a translating or vibrating sphere near SNs [56] and a vibrating sphere near CNs [38] the distance Δ between the two zeros (or the two maxima/minima) is a measure of the distance between object and fish. In this section, we extend these ideas and in essence show that Δ is *proportional to* the distance between the lateral line and a *vibrating* sphere for SNs for an axis of vibration parallel as well as perpendicular to the skin of the fish.

5.1.1 Velocity Parallel to the Fish Body

In the case of oscillation parallel to the lateral-line, the velocity in the x-direction is given by (3.2). In view of $\mu(t) = 2\pi\omega s a^3 \sin(\omega t)$, the velocity oscillates with frequency f, i. e., angular frequency $\omega = 2\pi f$, around a maximum value of

$$v_{x-\max}(x, y = D) = \frac{\omega a^3 s \left(2x^2 - D^2\right)}{\left(x^2 + D^2\right)^{5/2}}. \tag{5.1}$$

Equation (5.1) has two zeros. The distance between the two zeros, which we will denote by $\Delta_\parallel$, is

$$\Delta_\parallel = \sqrt{2}\, D\,. \tag{5.2}$$

Thus, the distance between the zeros of the velocity field is proportional to the distance D of the sphere to the skin *and does not depend on any other parameter.*

5.1.2 Velocity Perpendicular to the Fish Body

For a sphere oscillating *perpendicularly* to the skin, the velocity field is given by (3.4). The amplitude of this flow field along the lateral line has two maxima separated by a zero. The distance between the maxima equals the distance D between the lateral line and the oscillating sphere

$$\Delta_\perp = D\,. \tag{5.3}$$

On the trunk of the fish, SN occurs in two main orientations with respect to the axis of highest sensitivity [129]. One orientation is sensitive to flow in the x-direction (Fig. 5.1) and the other orientation is sensitive to flow perpendicular to

the x-direction (although much fewer neuromasts are sensitive to this direction). In the former case, the pattern of activity at the SN afferent nerves is characterized by three peaks of the evoked discharge-rate that are separated by a change in the sign of the water velocity (*triphasic* response, see Fig. 5.1, in red) while, in the latter case, there are two consecutive peaks of the evoked discharge-rate again separated by a change of direction of the water, *biphasic* response, see Fig. 5.1 in blue, [33, 126]. The meaning is that the depth of the curve is proportional to the distance between the maximum in both direction. The distance can also be determined linearly by taking the depth of the curve at any constant relation (half of the maximal intensity, etc.); see for instance Fig. 5.5. It is interesting to see that the above results are similar to those derived by [38] in the context of *CNs*.

5.1.3 Determination of the Direction of the sphere

Since, in reality, stimuli are not always moving *parallel* or *perpendicular* to the the line of detectors. We can ask us, how this mechanism works when the sphere has an arbitrary axis of motion in respect to the orientation of the detectors.

The potential for an *arbitrary* axis of vibration (or translation) in the xy-plane making an angle α with the x-axis is $\phi(x, y, t) = \phi_\|(x, y, t) \cos \alpha + \phi_\perp(x, y, t) \sin \alpha$. Franosch et al [56] have shown that for a translating (or a vibrating) sphere the angle α can be determined from the zeros and the maxima and minima in the flow field. This is possible for *any* α.

Real fish, however, may use a special behavioral strategy based on the zeros, since the latter are easily detectable. In experiments on blind mottled sculpins, it was observed that fish frequently approach the source in steps [25, 27, 130]. First they align themselves parallel to the axis of the sphere motion where $v(x)$ is an even function of the position; see Fig. 5.1. Second, they approach the sphere frontally. These two steps are repeated at increasingly close distances until the fish is close enough for a strike. Based on this approach behavior, we assume that the fish measures the position of a vibrating sphere when the trunk lateral line is *parallel* to the direction of vibration. This behavioral mechanism solves the problem of angle determination. Often the fish just needs one estimation before performing the strikes [34]. This is in agreement with the mechanism we propose here and shows that often fish do not need to re-estimate the distance. Sherryl Coombs and co-worker [37] also proposed another interesting mechanism. This mechanism, however, is good for mottled sculpin only since it uses the large pectoral of these fish.

Angle determination algorithms for angles near 0 and $\pi/2$ have been proposed previously [38, 56]. In addition, Franosch et al [56] have also presented a relation
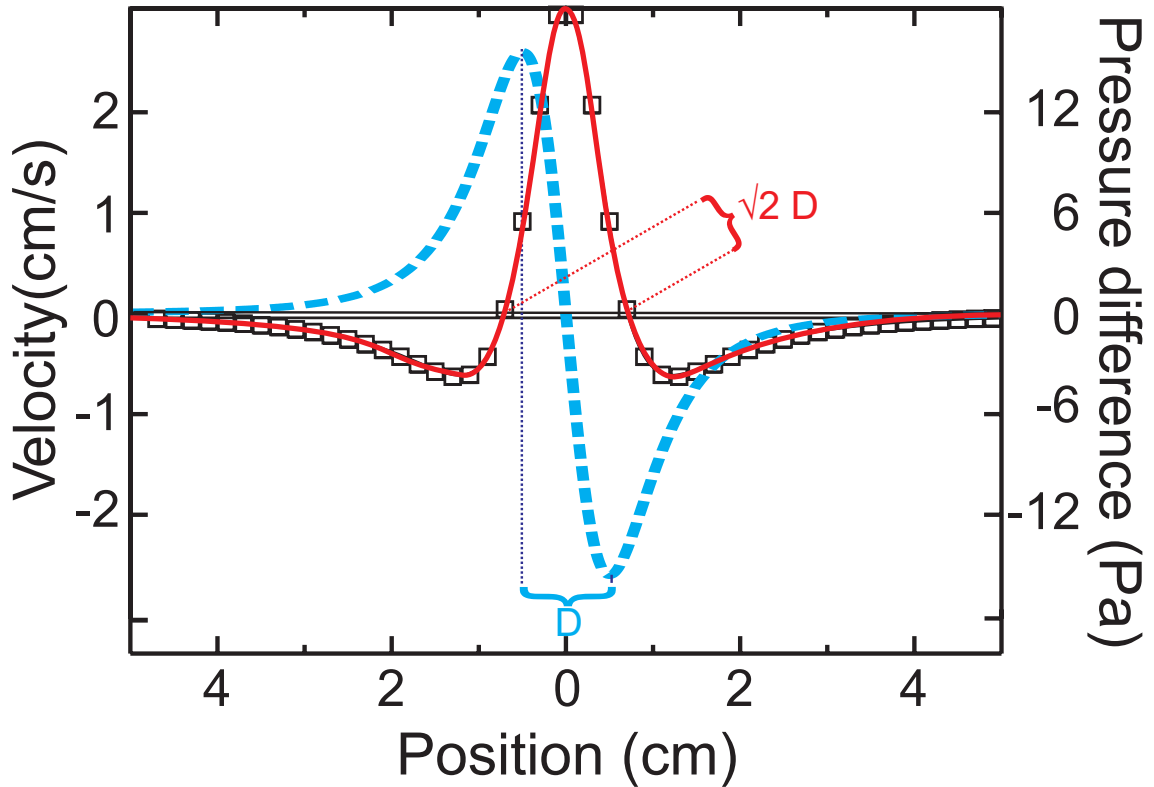
Figure 5.1: *Amplitude of the velocity v_x near the skin of the fish in dependence upon the x-position. The stimulus is an oscillating sphere at $D = 1$ cm from the skin. The sphere is oscillating either parallel (solid line, cf. 3.2) or perpendicularly (dashed line, cf. 3.4) to the line of detectors and thus generates either a triphasic or a biphasic response. The distance between the zeros is $\sqrt{2}D$ for the parallel condition and the distance between maximum and minimum is D for the perpendicular condition. The squares represent the pressure difference. The velocity field and pressure difference field are proportional to each other; cf. 3.9. This figure is a reproduction of figure 3.2.*

valid for any angle. At the moment, however, it is difficult to select a universal mechanism that fish use. We therefore limit ourselves to the case of a stimulus moving in *parallel* or *perpendicularly* to the skin of a fish [37].

5.1.4 Structure of this Chapter

The rest of this chapter will extend the result we present in this section. We will show that this mechanism for distance determination is *robust*. First, by showing that it is also applicable to CNs with a finite inter-pore distance (Sect. 5.2), and for distance determination in a *3-D*-world (Sect. 5.3). We will also show that the mechanism holds for a lateral-line with a curvature (Sect. 5.4) and how fast it converges to the *flat*-fish case. In section 5.5, we will verify our theoretical calculations with experimental data. The following sections will show that this mechanism is also applicable to a translating sphere (Sect. 5.6) and it is in a great extend *in*dependent of the form of the fish (Sect. 5.7). The last section (5.8), will show that the linearity will be preserved in the medulla even if the afferent project with a large dendritic arborization. All together, it means that the depth of the curve is a reliable cue enabling fish to estimate the distance of an object perpendicular to its skin.

5.2 Distance Determination by CNs

Canal neuromasts are sensitive to the pressure difference between two adjacent pores. We are therefore interested in the pressure field and will show analytically that the pressure difference distribution along the lateral line canal has a form *identical* to that of the the velocity field (Fig. 5.1). The pressure between two adjacent pores is given by 3.9.

Again, the distance between the zeros $\Delta_\parallel$ is proportional to the distance D of the sphere. A mathematical expression for the distance between the zeros can be found by equating 3.10 to zero and then keeping only the terms linear in δ, since $\delta \ll x$ and $\delta^2 \ll \delta$. This leads to

$$-2D^6 + 6D^2x^4 + 4x^6 = 0 \,. \tag{5.4}$$

The above equation has two real-valued zeros $x = \pm D/\sqrt{2}$. Hence $\Delta_\parallel = \sqrt{2}\,D$, which corresponds to what we have shown before for the velocity field governing the response of SNs. This means that, for distance determination, both SNs and CNs function by means of the same mechanism.

5.3 Three Dimensions

Up to now, we just have considered a flat fish, but real fish live in a *3-D* world, and also occupy the z-axis. There is evidence [82] that fish can use their lateral line not only to detect a source in a *horizontal* plane, but also to determine the source's *elevation*, i.e., its z-component. Anatomical data show that both SNs and CNs are organized orthogonally to each other [130]. In the following we also show how fish could compute the *3-dimensional* position of a dipole from their lateral-line data.

For a dipole at position $(0, D_y, D_z)$, we get

$$\phi_\parallel (x, y, z, t) = -\frac{\mu (t)}{4\pi} \left\{ \frac{x}{[x^2 + (D_y - y)^2 + (D_z - z)^2]^{3/2}} \right.$$
$$\left. + \frac{x}{[x^2 + (D_y + y)^2 + (D_z - z)^2]^{3/2}} \right\}. \tag{5.5}$$

Simplifying the anatomy of the lateral line, we assume two lines of receptors arranged perpendicularly to each other along the x and z axis (with $y = 0$), so as to get

$$v_x = \frac{\mu (t)}{2\pi} \frac{2x^2 - [(D_y)^2 + (D_z - z)^2]}{\left[x^2 + D_y^2 + (D_z - z)^2\right]^{5/2}}. \tag{5.6}$$

Since we are interested in the velocity along the line of receptors on the x-axis, we set z to zero and calculate the distance between the zeros as

$$\Delta_{3D} = \sqrt{2}(D_y^2 + D_z^2)^{1/2} \tag{5.7}$$

For the line of receptors along the z-axis we find

$$v_z = \frac{\mu (t)}{2\pi} \frac{3x(D_z - z)}{[x^2 + D_y^2 + (D_z - z)^2]^{5/2}}. \tag{5.8}$$

If $x \neq 0$ (i.e. the line of detectors is not at $x = D_x = 0$), then there is one point with zero velocity on the z-axis at $z = D_z$.

Fish may then determine the position of a dipole in three dimensions as follows:

- The x-position D_x of the dipole is between the two zeros of v_x.

- The z-position D_z is at the zero of v_z.

- The y-position is calculated with 5.7.

We have done the above calculation for receptors sensitive to velocity, i.e., SNs. For CNs the same calculation applies since we have already shown through 3.9 that the pressure difference distribution along the canal lateral line has an identical form to that of the velocity field. It shows that our 2-D mechanism can be transformed easily so has to hold for object localization in *three* dimensions for both SNs and CNs.

5.4   Lateral Line with Curvature

So far, we have modeled the lateral-line system as a straight line. Strictly speaking, this may be, and in general is, incorrect since a fish body is practically always curved. We have therefore applied our method to a curved surface in order to analyze the effect of curvature on the relationship between the zeros of the velocity field and pressure difference field. Because of the curvature, the relation between the distance $\Delta_\parallel$ of the zeros and the distance to the sphere becomes non-linear. We note, however, that this relation is always *independent* of dipole strength, frequency or size which means that the distance to the sphere can, nevertheless, be computed from the distance between the zeros. We will also quantify the effect of curvature for two real goldfish.

To get an estimate of the natural degree of curvature, we have measured the shape of two goldfish (6.5 and 10 cm long). Assuming the fish is axially symmetric with respect to the x-axis, we have used a polynomial to fit the geometry of the fish. Let us assume that $Y(x)$ is the distance of the fish's skin from the x-axis. As shown in Fig. 5.2, a polynomial of degree three of the form $Y(x) = ax^3 + bx^2 + cx + d$ can already fit the experimental data. Table 5.1 shows the coefficients.

The dipole is at distance D from the fish's skin and at x-position X_0. At X_0, the skin is at a distance $Y_0 := Y(X_0)$. For a sphere oscillating parallel to the tangent to the (now curved) line of detectors, the velocity potential at a position (on the skin of the fish) $(x, Y(x))$ is

$$
\phi_\parallel(x, y = 0, t) \;=\; \frac{-\mu(t)}{4\pi} \left\{ \frac{x - X_0}{\left\{ [x - X_0]^2 + [Y(x) - D - Y_0]^2 \right\}^{3/2}} \right.
$$
$$
\left. + \frac{x - X_0}{\left\{ [x - X_0]^2 + [-Y(x) + D + Y_0]^2 \right\}^{3/2}} \right\} . \tag{5.9}
$$
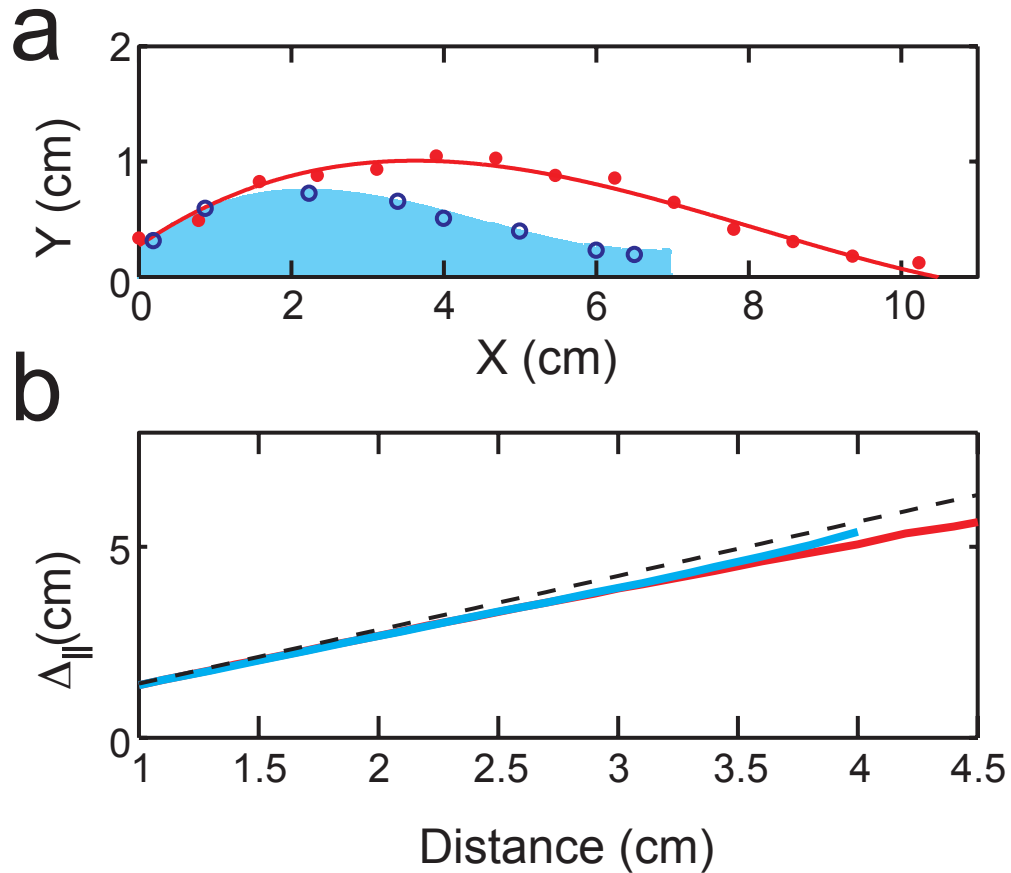
Figure 5.2: **a** *Experimental measurement of the curvature and, thus, of the radius of curvature of two real goldfish (open circle 6.5 cm long, filled circle 10 cm long). The solid line represents a polynomial fit to the data; see Table 1 for the coefficients.* **b** *The theoretical distance $\Delta_{\parallel}$ between the zeros in the velocity field for the two goldfish as a function of the distance D to the sphere. The black dashed line is the approximation $\Delta_{\parallel} = \sqrt{2}\,D$ valid for a straight lateral line. There is only a small difference between both fish. Moreover, (5.13) shows that $\Delta_{\parallel}$ only depends on the distance to the stimulus and not on stimulus amplitude or frequency.*

Length of the fish (cm)	a	b	c	d
6.5	0.012	0.16	0.53	0.22
10	0.0033	0.08	0.45	0.27

Table 5.1: *Polynomial fit through $ax^3 + bx^2 + cx + d$ for the radius of curvature of two real goldfish. Figure 5.2 shows that such a polynomial of degree 3 already fits the experimental data quite well.*

The distance $r(x)$ between the point at position x on the lateral line and the center of the oscillating sphere is

$$r(x) = \left\{ [x - X_0]^2 + [D - Y(x) + Y_0]^2 \right\}^{1/2} . \tag{5.10}$$

With the definition

$$R(x) := \left\{ [x - X_0]^2 + Y^2(x) \right\}^{1/2} , \tag{5.11}$$

the velocity field at the fish's skin ($y = 0$) is

$$
\begin{aligned}
v_x(x,t) &= \frac{1}{R(x)} \left. \frac{\partial \phi_\parallel(x,y,t)}{\partial x} \right|_{y=0} \\
&= \frac{1}{R(x)} \left\{ \frac{\partial \phi_\parallel[x,Y(x),t]}{\partial x} + \frac{\partial \phi_\parallel[x,Y(x),t]}{\partial Y} \frac{\mathrm{d}Y(x)}{\mathrm{d}x} \right\}_{y=0} \\
&= \frac{\mu(t)}{4\pi R(x) r^5(x)} \left\{ 2[x - X_0]^2 - [D - Y(x) + Y_0]^2 \right. \\
&\quad \left. + 3[x - X_0] \, [D - Y(x) + Y_0] \, [\mathrm{d}Y(x)/\mathrm{d}x] \right\} .
\end{aligned}
\tag{5.12}
$$

The zeros of the velocity field follow from $v_x(x,t) = 0$ and therefore from

$$
\begin{aligned}
0 &= 2 \, [x - X_0]^2 - [D - Y(x) + Y_0]^2 \\
&\quad + 3 \, [x - X_0] \, [D - Y(x) + Y_0] \, [\mathrm{d}Y(x)/\mathrm{d}x]
\end{aligned}
\tag{5.13}
$$

The distance between the two *real* zeros (x_+ and x_-) along the fish's skin is

$$\Delta_\parallel = \int_{x_-}^{x_+} \sqrt{1 + |\mathrm{d}Y(x)/\mathrm{d}x|^2} \mathrm{d}x . \tag{5.14}$$

Figure 5.2 b shows that the difference in $\Delta_\parallel$ between the two goldfish is negligible. Figure 5.4a compares the theory developed above with experimental results.

In the case of a dipole oscillating *perpendicularly* to the line of detectors, we proceed in the same way except that we focus on the difference between the maxima of the velocity amplitude instead of the zeros. Since, the field is biphasic.

The velocity field on the skin of the fish is

$$
\begin{aligned}
v_x(x,t) &= \frac{-\mu(t)}{4\pi R(x) r^5(x)} \left\{ 3 \, [x - X_0] \, [D - Y(x) + Y_0] \right. \\
&\quad \left. + r^2(x) - 9 \, [x - X_0] \, [D - Y(x) + Y_0] \right\} .
\end{aligned}
\tag{5.15}
$$

The distance $\Delta_\perp$ between the maxima of the velocity amplitude follows from $\mathrm{d}v_x/\mathrm{d}x = 0$. The zeros of the velocity field, i. e., $v_x(x,t) = 0$, do not depend on $\mu(t)$, and

therefore the distance D to the dipole is just a function of the distance to the source and the form of the fish body. As noted above, this relation is non-linear, but the deviation from a linear relation is minimal and probably suffices for a fish to either catch or avoid an object.

5.4.1 Convergence of the Curved Model

Another interesting question concerns the rate at which the predictions of the model describing now a curved fish body converge to those of a straight line as the body curvature vanishes. In order to answer this question, we assume an arc of radius R at a distance D to an oscillating dipole. For a dipole oscillating parallel to the tangent to the curved line of detectors, the velocity potential is

$$\phi_\|(R, \theta, t) = \frac{-\mu(t)}{4\pi} \frac{R\sin\theta}{[R^2\sin^2\theta + (D + R - R\cos\theta)^2]^{3/2}} , \quad (5.16)$$

where R is the radius of the lateral line, $(0, D)$ the position of the dipole, and θ is the angle between the radius and the y-axis. The velocity in θ-direction (perpendicular to r) is

$$v_\theta(R, \theta) = -\frac{\mu(t)}{2\pi} \frac{2(D + R)^2\cos\theta + R(D + R)[\cos(2\theta) - 5]}{2[(D + R - R\cos\theta)^2 + R^2\sin^2, \theta]^{5/2}} \quad (5.17)$$

so that $v_\theta = 0$ results in

$$2(D + R)^2\cos\theta + R(D + R)[\cos(2\theta) - 5] = 0 . \quad (5.18)$$

Solving (5.18) explicitly for θ we find as real solutions

$$\begin{aligned}
\theta_\pm &= \mp\arccos\left[\frac{(D^2 + 2DR + 2R^2)}{2R(D + R)}\right. \\
&\left. - \frac{(D^4 + 4RD^3 + 20R^2D^2 + 32R^3D + 16R^4)^{1/2}}{2R(D + R)}\right] .
\end{aligned} \quad (5.19)$$

For small curvature, R is large. Focusing on the immediate surroundings of a dipole we assume θ is small and develop the expression in (5.18) into a Taylor series near $\theta = 0$,

$$2D^2 - (D + 2R)^2\theta^2 + \mathcal{O}(\epsilon^4) = 0 , \quad (5.20)$$

and find the solutions $\theta_\pm = \pm\sqrt{2}D/(D + 2R)$ and hence $\Delta = (\theta_+ - \theta_-)R = 2\sqrt{2}\,DR/(D + 2R)$. Since $D + 2R \approx 2R$ for large R, we recover $\Delta = \sqrt{2}\,D$. Plotting $\Delta_\| = R(\theta_+ - \theta_-)$, we see from Fig. 5.2 that for a curvature near $R = D = 1$ cm the distance between the zeros is almost D, whereas for a straight lateral line the limit approaches $\sqrt{2}\,D$.

The same kind of solution is applicable for the *antisymmetric* (*bi*phasic) field (that means that one half of the pattern is a reverse image of the other half), see Fig. 5.1. In this case, the velocity potential is

$$\phi_\perp(R,\theta,t) = \frac{-\mu(t)}{4\pi} \frac{D + R(1 - \cos\theta)}{\{(R\sin\theta)^2 + [D + R(1 - \cos\theta)]^2\}^{3/2}} \,.\tag{5.21}$$

The maxima/minima of the velocity v_θ are at

$$\theta_\pm = \pm \frac{D\sqrt{2(2D + 3R)}}{\sqrt{2D^3 + 16RD^2 + 37R^2D + 24R^3}} \,.\tag{5.22}$$

The Taylor series takes the form of

$$(-8D^4 - 12RD^3) + (4D^4 + 32RD^3 + 74R^2D^2 + 48R^3D)\,\theta^2 = 0\,.\tag{5.23}$$

Figure 5.3 shows the dependency of the distance between the zeros of the velocity or the maxima of the velocity and the distance of the stimulus. The distance $\Delta_\perp$ converges a bit faster to D than $\Delta_\|$. The calculations above show how a fish can localize objects in front of its mouth or eyes where curvature is of great importance.

5.5   Comparison with Experimental Data

We now turn to the question of whether, and how, the distance to the sphere is unambiguously encoded in the distance between the zeros or the maxima in the discharge pattern of the afferents. Since our model shows that the factor governing the linear relationship between sphere distance D and Δ depends on the orientation of the neuromasts, we will first present the results obtained by pooling data from afferents with identical orientations. For "triphasic" fibers, Fig. 5.4a shows the dependence of the distance $\Delta_\|$ between the zeros of the velocity field upon the distance D to the sphere. For "biphasic" fibers, Fig. 5.4b shows the dependence of the distance $\Delta_\perp$ between the amplitude maxima upon D.

A linear fit of the data shows that there is a correlation between the distance to the sphere and the distance between the phase reversals for the case of triphasic receptive fields with $\Delta_\| \approx 1.13\,D$ ($R^2 = 0.96$). The slope of this fit is significantly larger than 1 and smaller than $\sqrt{2}$. The model including the curvature of the fish explains the measured data better (probably because it changes the distance to the object a little). The obtained slope is thus in agreement with the two values predicted by a *linear* model for both SNs and CNs. It is important to note that neuronal data for this analysis were not sorted by neuromast type (CN or SN) but only by the orientation of the neuromasts (triphasic or biphasic receptive field).
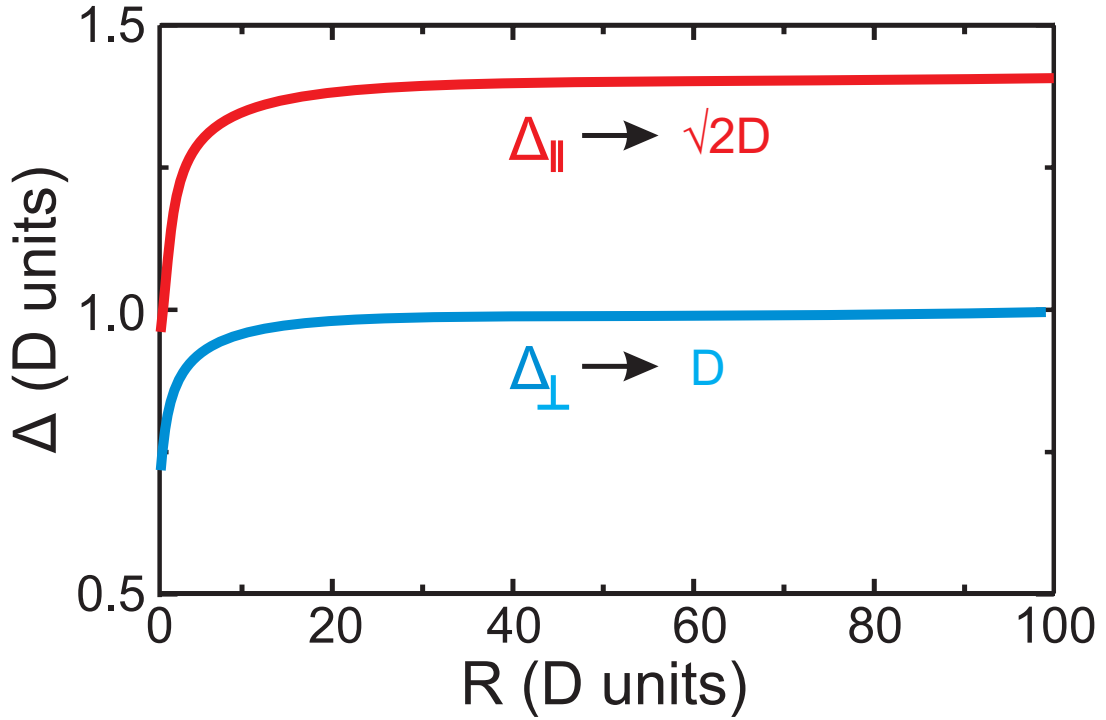
Figure 5.3: *Effect of decreasing curvature R^{-1} as the radius of curvature R becomes large so that $R^{-1} \rightarrow 0$. The distance $\Delta_\parallel$ between the zeros of the velocity field converges to $\sqrt{2}D$ (red line) for a parallel direction of oscillation of the sphere. In case of perpendicular oscillations the distance $\Delta_\perp$ between the maxima in amplitude of the velocity field converges to D (blue line).*

Since the linear relation between Δ and D is just an approximation valid for a *flat* fish, we also show the theoretical results in the case of a *real* fish. For the biphasic case, $\Delta_\perp = 1.02\,D$, which is not significantly different from the slope 1.0 given by (5.3).

We did not attempt to separate CNs and SNs here. The physiological data confirm the results shown in Fig. 5.1, i.e., both the velocity and the pressure difference between the pores present the distance of the sphere in the *same* manner. This was further confirmed when we analyzed the receptive fields of triphasic SNs and CNs separately (Fig. 5.4). There is no significant difference in the slope for the Cs and the SN populations.
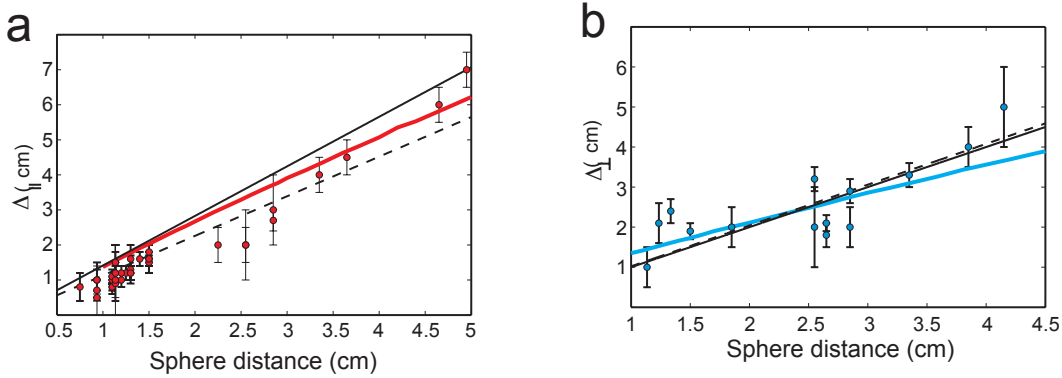
Figure 5.4: **a** *Distance $\Delta_{\parallel}$ between the zeros of the velocity field as a function of sphere distance for afferents with triphasic receptive fields. Error bars show standard deviations in y-direction. The standard deviation in x-direction is 0.1 cm. The thick solid line is the theoretical prediction for the curved 10 cm long goldfish; cf. and (5.13). The dashed line is the predicted result for a straight lateral line; cf. (5.2). The solid line is the best linear fit of the measured data $1.13D$. The data agree well with the theoretical prediction for the curvature effect. **b** Distance $\Delta_{\perp}$ between the maxima in amplitude of the velocity field as a function of sphere distance for afferents with biphasic receptive fields. The thick solid line is the theoretical prediction for the curved 10 cm long goldfish. The dashed line is the predicted result for a straight lateral line (5.3). The straight line $1.02\,D$ is the best linear fit to the measured data.*

5.6 Determining Distance to a Translating Sphere

We have discussed the case of translating spheres in section 3.2. The velocity field of a translating sphere resembles that of an oscillating dipole. What we developed earlier can, therefore, also be applied to such naturalistic stimuli. However, to calculate the pressure difference between the pores, one needs to perform a second spatial derivative. That is, we have to check if the distance between the maxima is still linear as in (3.14),

$$\Delta p(x,t) = 6a^3 w^2 \delta \frac{X[2X^2(t,x) - 3\,, D^2]}{[D^2 + X^2(t,x)]^{7/2}} \; . \tag{5.24}$$

where $X(t,x)$ is the position of the sphere function of its initial position x and the time t. The pressure difference field is again antisymmetric in x and the distance between the maximum and the minimum is $\Delta_{\perp} \approx \sqrt{1.21}\,D$. Hence, a simple linear encoding of the distance between fish and object may well hold for a translating sphere too.

5.7 Effect of Prey Form on Distance Determination

It has been shown that the form of the *prey* (object to be detected) is encoded in the signal up to one body length of the prey [131]. That is usually a really short distance if we consider a prey much smaller then the predator. However, the issue is whether the form of the object has an effect on distance determination in depth.

The velocity potential (in prolate ellipsoidal coordinates) of an ellipse of greater axis a and eccentricity e moving parallel to its greater axis (z, to respect the common definition of the prolate ellipsoidal system) is, [95, §105],

$$A \;=\; \frac{Ua}{\left(\frac{1}{1-e^2} - \frac{1}{2e}\log\frac{1+e}{1-e}\right)} \tag{5.25}$$

$$\phi \;=\; A\mu\left(\frac{\xi}{2}\log\frac{\xi+1}{\xi-1} - 1\right). \tag{5.26}$$

The *prolate ellipsoidal* coordinate system [95, §103] is a 3-dimensional orthogonal system defined as

$$x \;=\; a\cos\theta\cosh\eta = a\mu\xi\,, \tag{5.27}$$

$$y \;=\; \varpi\cos\omega\,, \tag{5.28}$$

$$z \;=\; \varpi\sin\omega\;\text{and} \tag{5.29}$$

$$\varpi \;=\; a\sin\theta\sinh\eta = a(1-\mu^2)^{1/2}(\xi^2-1)^{1/2}\,. \tag{5.30}$$

The surface $\xi = $ constant, $\mu = $ constant are confocal ellipsoids and hyperboloids of two sheets, respectively, the common foci being the points $(\pm a, 0, 0)$. The value of ξ may range from 0 to ∞, while μ lies between ± 1. The coordinates μ, ξ, ω form the prolate ellipsoidal system. We have to specify that the *prolate ellipsoidal* coordinate system differs from the *prolate spheroidal* since the cross section is an ellipse and not a circle.

We parametrize a line of detectors at $y = D$, $x = 0$ and z varying from -5 to 5. The velocity parallel to the detector is given by applying the chain rule

$$v_z = \frac{d\phi}{dz} = \frac{\partial\phi}{\partial\mu}\frac{d\mu}{dz} + \frac{\partial\phi}{\partial\xi}\frac{d\xi}{dz}\,. \tag{5.31}$$

For the CNs the pressure gradient is given by

$$\Delta p_z \approx \frac{d}{dz}\frac{d\phi}{dt} = U\frac{d^2\phi}{d^2 z}\,. \tag{5.32}$$

To be able to compare the shape of the velocity or pressure difference-field at the *receptors* we normalize the intensity of the velocity or ΔP since decreasing the eccentricity e also decrease the volume of the object. We then compare the velocity or the pressure difference field for a sphere ($e = 1$) and for an ellipse with $e = 0.3$ at one and two body lengths of the prey, see Fig. 5.5. The form has a noticeable effect at one body length, but we are not able to see this effect at two body length.

We now consider the question of what effect the form of the fish may have on distance determination. In order to do that we calculate the distance between the zeros (for the velocity field) or the distance between the maximum and minimum (pressure difference) and normalize it

$$\% \, \mathrm{Error} = 100 * \frac{\Delta_{\mathrm{sphere}} - \Delta_{\mathrm{ellipse}}}{\Delta_{\mathrm{sphere}}} \, . \tag{5.33}$$

Figure 5.6 shows the error determination based on the maxima (CNs) presents a relative error that is important at one body length of the prey but negligible at two. The error based on the zeros (SNs) is already negligible at one body length. It is interesting to note that we observed that fish has a tendency to overestimate the distance to a prey [83]. That will be the case if the fish uses the mechanism we present here, but learns to base its estimation on a perfect sphere.

5.8 Integration

If we want the above kind of mechanism to be useful to a fish, the linear dependency on depth of the curve should be preserved (for future analysis) or extracted in the brain. One solution (using in vision for instance) is that the neural encoding preserves the scaling (intensity, size, brightness) of the stimulus. These parameters can then be extracted to give the animal important cues about its environment. There is evidence that lateral-line afferents have a large central arborization in the medial ovtavolateral line nucleus of the medulla. Hence,, a high degree of convergence is to be expected [10].

Moreover, as we noted earlier, there is no evidences of recurrent connectivity between the cells on a same layer in the medulla (personal communication Jacob Engelmann). It is, therefore, of interest to look at what will happen with the linearity of the relation encoded at the periphery, when many individual fibers reach a single medullary neuron.

In order to analyze this question in more detail, we postulate a Gaussian distri-
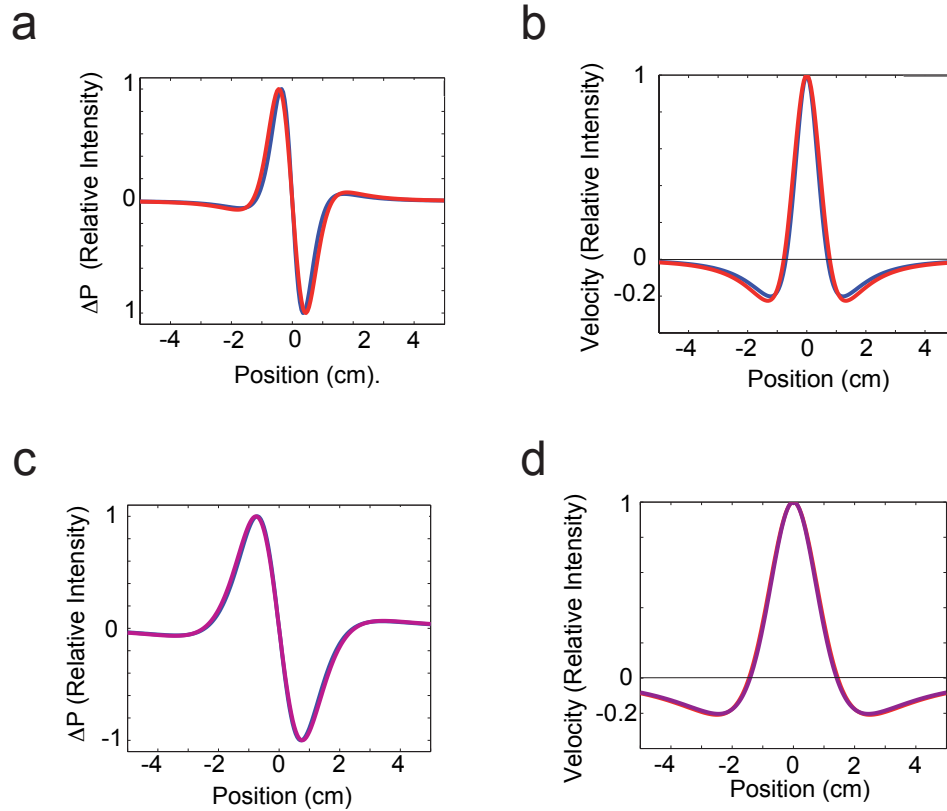
Figure 5.5: *Comparison of the stimulus on a straight line of velocity or pressure-difference detectors as a consequence of a sphere of diameter $a = 1$ cm (red) and an ellipse of greater axis 1 cm and eccentricity $e = 0.3$ (blue) **a** pressure-difference (CN) for the sphere/ ellipse at 1 cm, **b** velocity for the sphere at 1 cm, **c** pressure-difference (CN) for the sphere/ ellipse at 2 cm and **d** velocity for the sphere at 2 cm. At 1cm there is small difference between the velocity/pressure difference produced by a sphere and an ellipse **a** and **b** (blue and red line) at 2 cm however there is really little difference between the two distances **c** and **d** (blue and red line coincide)*

Figure 5.6: *Error in distance determination for a translating ellipse and a translating sphere based on maximum and minimum (CNs) or the zeros (SNs) function of the eccentricity of the ellipse at a distance $D = 1\,\mathrm{cm}$ (one body length of the prey, blue line), $D = 2\,\mathrm{cm}$ (two body length 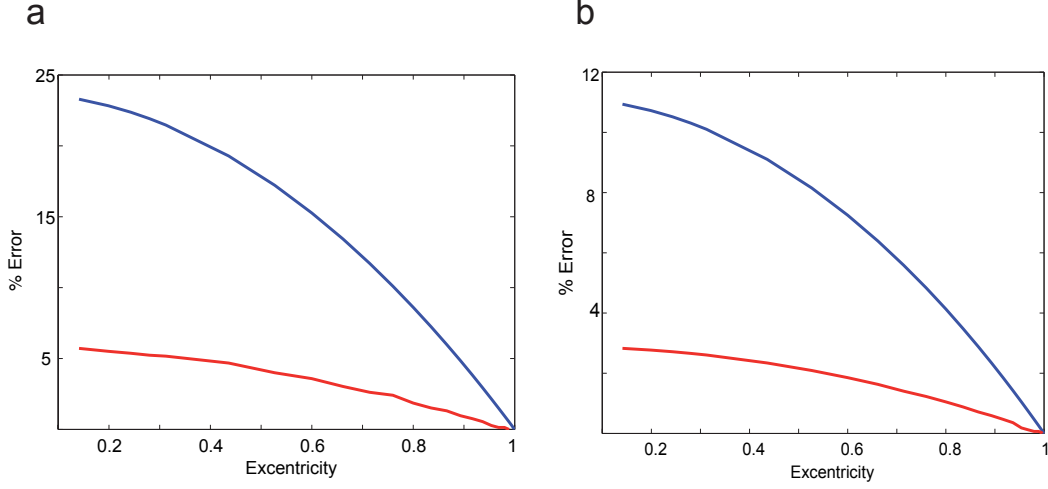of the prey, red line), **b** error in the maxima (CNs) as we see here the error at one body length is not negligible, but at a distance $D = 2\,\mathrm{cm}$ it is. **b** Error in the distance determined by means of the distance between the zeros (SNs); here the error is already negligible at one body length.*

bution of weights between a medullary neuron and its afferents

$$J(x_i, x_j, \sigma, J_0) = J_0 \exp\left(-\frac{[x_i - x_j]^2}{\sigma^2}\right), \tag{5.34}$$

where x_i represents the detector, x_j the neuron in the medulla, J_0 is the maximum intensity of the weight, and σ^2 is the variance of the weight distribution. We again use a linear approximation to the firing rate of the afferent and of the medullary neurons. The activity of the neurons in the medulla becomes

$$F_{\mathrm{Medulla}}(x_i, x_j, \sigma, A, J_0, D) = A \sum_{x_i} J(x_i, x_j, \sigma, J_0) * \frac{(D^2 - 2x_i^2)}{(x_i^2 + D^2)^{(5/2)}} \tag{5.35}$$

(for a sphere vibrating parallel to the receptors).

Here, x_i, x_j, J_0 and σ are as explained earlier, A is a transfer constant between the firing rate and the vibration of the sphere, and D is the distance of the sphere
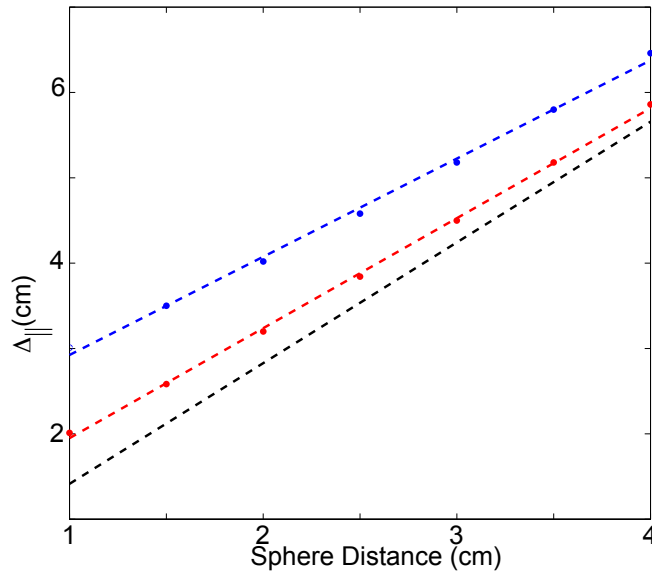
Figure 5.7: $\Delta_{||}$ *Distance between the zeros of a triphasic receptive field for a medulla cell receiving input from all afferent of a lateral-line of length $10\,cm$ and a distance between the detectors of $\delta = 2\,mm$ as a function of the sphere distance D. The dashed black line is the theoretical prediction for the afferent field $y = \sqrt{2}D$, dots are distance between the zeros determined numerically (red dots $\sigma = 2$, blue dots $\sigma = 10$). The blue and red dashed lines are a numerical fit through the points. For the blue points the fit is $y = 0.49x + 0.56$ and for the red one $y = 1.02x + 0.96$. As we see, a linear approximation based on $\Delta_{||}$ for distance determination is valid even if σ, the depth of the central arborization of the afferent in the MON, is large.*

perpendicular to the detectors. We then use a line of detectors of length $10\,cm$ with a distance between the detectors of $\delta = 2\,mm$ and determine the distance between the zeros numerically for two different connectivity pattern (one with $\sigma = 2$ and the other with $\sigma = 10$), as we can see in Fig. 5.7 graphically. We can therefore that even if distance between the zeros may become larger due to a large central arborization in the MON, it nonetheless remains linear.

6. Aquatic Imaging: Map Formation in the Lateral-Line System

In this chapter we show how in the torus a fish can create a retinoscopic representation of the water motion around its body with the help of the visual system.

Little is known about central physiology of hydrodynamic stimuli in fishes; for examples see [7, 10, 12, 13, 16, 32] and section 1.3 of this dissertation. One major problem is the lack of experimental recordings in the mechanosensory pathway for a single species. The few data come from a mix of recordings on trout or goldfish, and some data concerning the projection of the afferent nerves to the medulla are from zebrafish. Because of the great variety of species, a great variability in brain structures and sensory systems can be found [16, 112]. Variations in the organization of the brain of fishes are closely related to functional specializations. In this chapter, we will introduce a minimal model in order to understand some *general principles* leading to the formation of a retinoscopic map in the torus of fishes. Our aim is to produce a minimal model enabling a fish to encode the direction of the water motion around its body in a somatotopic way.

Sensory information is very often processed by means of a neuronal map. A neuronal map is an array of neurons in which neighboring neurons respond to sensory input in an organized way; for a example, the position of a visual stimulus. Quite often, this input is organized according to the topography of the retinal input cells

(retinoscopic organization). This is due to the fact that the retina projects directly to the optic tectum (OT, or its mammalian counterpart, the superior colliculus) [140].

Several anatomical, behavioral, and physiological studies have demonstrated the existence of central lateral-line maps in a double somatotopic way (afferents and output cells). However, the demonstration of the existence of true somatotopic organization within the medulla has failed. There is evidence that toral cells receive input from flow insensitive medulla neurons,probably receiving input from CN afferents, map the position of a moving object (in the experiment a sphere) into a somatotopic map [45, 119]. We will also show that the data for flow sensitive (probably receiving input from SNs) units presented in [119] are in favor of a somatotopic encoding of *water motion*. Water motion due to a translating sphere stimulates SN afferents sensitive to both directions and in a way similar to the findings of Plachta et al [119].

Multimodal maps, i.e. maps responding to different sensory modalities, are frequent in brains. A general feature of multimodal maps is that all sensory modalities are spatially aligned. There are several examples, e.g,. the map alignment in the optic tectum of rattle snakes [72, 110], where infrared and normal vision come together with audition. For a multimodal representation to be useful the signal for each sub-modality must be calibrated with the others. Ultimately, all sensory input must be used to generate (motor) responses. All maps must therefore be in proper alignment with each other. This alignment is not present at birth and should therefore be learned [89, 136]. For many animals it has been shown that visual input is guiding the integration of multiple senses. A really interesting case is that of the clawed frog, *Xenopus laevis*. Where the signals seem to guide the formation of a map of surface waves (lateral-line input). One reason why the visual system might have a *universal* teaching role through multi-sensory integration is that the retina is intrinsically ordered as a map, and active waves spreading over the retina were found in the embryo of many species [143].

In the optic tectum of fish, there exists a coherent sensory representation of the input from the somato-sensory (lateral-line), visual, auditory, and (for electric fish) electric senses [9]. There is also evidence in the torus that some cells sensitive to a mechano-sensory input will also respond to auditory stimuli. The projections between torus and optic tectum (OT) are topographically matched [138, 139]. This means that the lateral-line map in the torus and the multi-modal map in the optic tectum should have an organization compatible with each other and be organized in a retinoscopic way. The OT map has a form similar to the image produced on the retina [78].

A major question arising here is how somatotopic maps can emerge in the torus if there is no or little organization in the medulla. It has already been shown that the visual system of the clawed frog *Xenopus laevis* can teach the lateral-line to form a map of water wave directions in the torus of the frog [55]. In other work of Friedel et al. [58, 59] it has been shown how the visual and the auditory map can become compatible with each other by means of a plasticity rule modifying the synapses of the auditory connections of the barn owl . They also show that the map is best with an inhibitory teacher signal and not an excitatory signal. It is interesting to see that the feedback from the *tectum opticum* to the torus semi-circularis is believed to be at least in part inhibitory. Vanegas et al [139] describe it as a signal exciting the few neurons at the exact position of the stimulus and inhibiting the other neurons around it.

6.1   Model

The basic question is how a fish can learn a coherent representation in the torus (see Fig. 6.1). However, the input is not the water motion nor the activity of the afferents, but the activity of the cells in the medulla. Our first task is, therefore, to model this input. In order to perform our task, we will apply the theory we have developed in the previous chapters of this dissertation.

6.1.1   From Water Motion to Medulla cells: the Detectors

The fish is modeled as an ellipse of long axis $a_{\text{fish}} = 6$ cm and short axis $b_{\text{fish}} = 1.5\,\text{cm}$. The angular distance between each detector is kept constant and the position in cartesian coordinates of the ith detector is given by $x_i = a_{\text{fish}} \cos \theta_i$ and $y_i = a_{\text{fish}} \sin \theta_i$ where i is the index of the detector and goes from 0 to $N = 180$ (number of detectors). The angular distance between two adjacent detectors is given by $\delta\theta = 2\pi/N$ and the angular position of the ith detector is therefore $\theta_i = i\delta\theta$. All parameters regarding the biophysical situation are given in table 6.1.

The stimulus is a translating sphere of radius $r = 0.5$ cm. It moves on an elliptic trajectory with axes $a_{\text{sph}} = 7$ cm and $b_{\text{sph}} = 1.5$ cm, and with a continuous velocity of $U = 10$ cm/s. The initial position of the sphere in cartesian coordinates is $X = a_{\text{sph}} \cos \theta_0$ and $Y = b_{\text{sph}} \sin \theta_0$, the initial position θ_0 of the sphere is chosen randomly for each learning trial. The position of the sphere is updated at each time step $\delta t = 1$ ms, for a learning trial of duration $T = 200$ ms. The trajectory of the
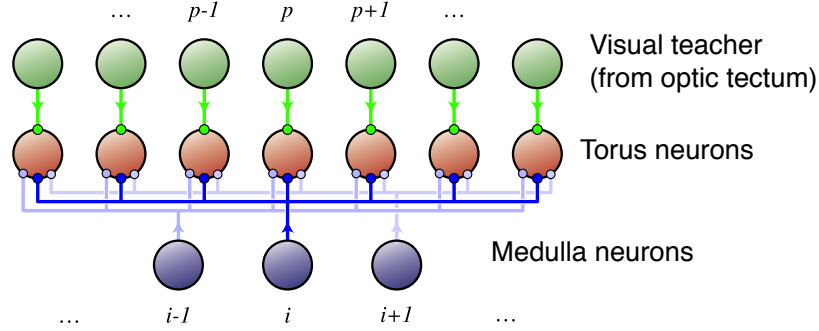
Figure 6.1: *The minimal model for the formation of a map within the torus (image modified after [59]). The medulla cells receive an input from the afferent nerves (connecting a neuromast) projected to the torus semi-circularis. In order to produce a map compatible with the retinal representation, a signal from the optic tectum modifies the connection between the cells in the tectum and the medulla. Since the input of the torus does not come from the detector, we first model how the water displacement at the detectors is encoded in the medulla.*

sphere at each time step is approximated by the following algorithm

$$\theta = \cos^{-1} X(t)/\{a_{\text{sph.}}\sqrt{[X(t)/a_{\text{sph.}}]^2 + [Y(t)/b_{\text{sph.}}]^2}\} \qquad (6.1)$$

$$\delta X = -a_{\text{sph.}}U\sin\theta/\sqrt{(a_{\text{sph.}}\sin\theta)^2 + (b_{\text{sph.}}\cos\theta)^2}$$

$$\delta Y = b_{\text{sph.}}U\cos\theta/\sqrt{(a_{\text{sph.}}\sin\theta)^2 + (b_{\text{sph.}}\cos\theta)^2} \qquad (6.2)$$

$$X(t+\delta t) = X(t) + \delta X$$
$$Y(t+\delta t) = Y(t) + \delta Y \,.$$

The trajectory resulting from this algorithm is not an exact ellipse, but a spiral. However, since our time steps (δt) are small and the learning trial is much shorter than the time that the sphere needs to make one revolution around the fish, we can neglect this error. The direction of the sphere motion in one time step is ($\delta X, \delta Y$). By applying the result of sections 3.2, 5.4.1 and [95, §92] the velocity potential (VP) becomes

$$\phi(X, Y, x_i, y_i) = \frac{Ur^3}{2}\frac{(x_i - X)\delta X + (y_i - Y)\delta Y}{\sqrt{[(x_i - X)^2 + (y_i - Y)^2]}^3} \,. \qquad (6.3)$$

In the case of SNs, the velocity parallel to the axis of maximum sensitivity of the

cupula becomes

$$
\begin{aligned}
v_{\theta_i} &= \frac{\mathrm{d}\phi}{\mathrm{d}\theta_i} \\[2mm]
v_{\theta_i} &= \frac{\partial\phi}{\partial x_i}\frac{dx_i}{d\theta_i} + \frac{\partial\phi}{\partial y_i}\frac{dy_i}{d\theta_i} \\[2mm]
\frac{\mathrm{d}\phi}{\mathrm{d}x_i} &= a^3 U \left\{ \frac{2\left[X(t) - x_i\right]^2 - \left[Y(t) - y_i\right]^2}{\sqrt{\left[(x_i - X)^2 + (y_i - Y)^2\right]}^5}\delta x \right. \\[2mm]
&\quad \left. + \frac{3\left[X(t) - x_i\right]\left[Y(t) - y_i\right]}{\sqrt{\left[(x_i - X)^2 + (y_i - Y)^2\right]}^5}\delta y \right\} \\[4mm]
\frac{\mathrm{d}\phi}{\mathrm{d}y_i} &= a^3 U \left\{ \frac{2\left[Y(t) - y_i\right]^2 - \left[X(t) - x_i\right]^2}{\sqrt{\left[(x_i - X)^2 + (y_i - Y)^2\right]}^5}\delta y \right. \\[2mm]
&\quad \left. + \frac{3\left[X(t) - x_i\right]\left[Y(t) - y_i\right]}{\sqrt{\left[(x_i - X)^2 + (y_i - Y)^2\right]}^5}\delta x \right\} \\[2mm]
v_{\theta_i} &= \frac{\mathrm{d}\phi}{\mathrm{d}x_i}\delta x_i + \frac{\mathrm{d}\phi}{\mathrm{d}y_i}\delta y_i
\end{aligned}
\tag{6.4}
$$

where

$$
\begin{aligned}
\delta x_i &= -a_{\text{fish}}\sin\theta_i / \sqrt{(a_{\text{fish}}\sin\theta_i)^2 + (b_{\text{fish}}\cos\theta_i)^2} \\
\delta y_i &= b_{\text{fish}}\cos\theta_i / \sqrt{(a_{\text{fish}}\sin\theta_i)^2 + (b_{\text{fish}}\cos\theta_i)^2}
\end{aligned}
$$

and the direction of the cupula axis of sensitivity is $(\delta x_i, \delta y_i)$, since it is sensitive to the water motion *parallel* to the fish body. For CNs, the pressure difference between the pores is

$$
\Delta p \approx \left(\frac{dv_{\theta_i}}{dt}\right) \cdot \delta,
\tag{6.5}
$$

where δ is the distance between two pores. In our case, δ varies a bit (since we keep the angle between the detectors fixed) but we can easily determine it numerically. The velocity and the pressure difference for the parameters we give in Table 6.1 is presented in Fig. 6.2. The variation in stimulus intensity is due to the fact that the sphere is translated on an ellipse so that the distance to the neuromast is *not* constant.

The resulting firing rate is given by the theory we have developed in section 3.2. Due to the linearity of the FI function (section 4.7), we can say that the firing rate for SNs takes the form (see for instance section 3.2)

$$
\begin{aligned}
r_{v_\theta}(x_i, y_i, X, Y) &= In + A \cdot v_\theta(x_i, y_i, X, Y) \tag{6.6} \\
r_{\Delta p}(x_i, y_i, X, Y) &= In + B \cdot \Delta P(x_i, y_i, X, Y), \tag{6.7}
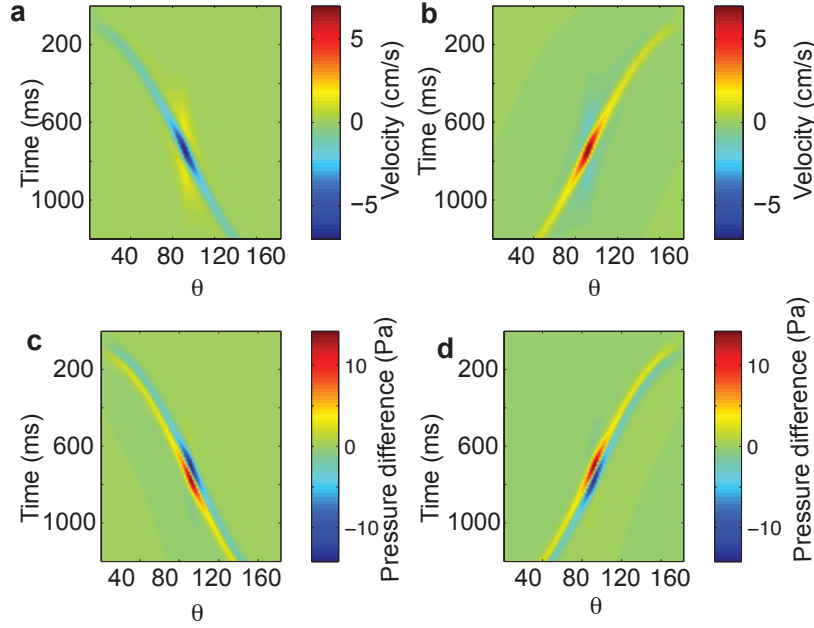\end{aligned}
$$

Figure 6.2: *Velocity parallel to the axis of maximum sensitivity of a SN cupula (**a,b**) and pressure difference between two adjacent CN pores (**c, d**). **a** Velocity parallel to the skin of an elliptic fish due to sphere translating at 10 cm/s on an elliptic trajectory (6.4). The sphere is translating from head to tail and in **b** from tail to head. The difference in stimulus intensity is due to the fact that on an elliptic trajectory the distance between the fish and the sphere is not constant. The parameters are given in Table 6.1. **c** Pressure-difference at the pores of the canal lateral-line system for the same translating sphere. The sphere is translating from head to tail in **c** and from tail to head in **d**.*

where In is the instantaneous firing-rate, A and B are parameters we fit and $r_{v\theta}$ is the firing rate for an afferent nerve innervating SNs and $r_{\Delta p}$ for an afferent nerve innervating CNs, in doing so, we can define the firing rate at the afferents in the $+$ direction (counter clockwise)

$$F(\mathbf{x}, t) = \begin{cases} r(\mathbf{x}, t) & \text{if } r(\mathbf{x}, t) > 0 \,, \\ 0 & \text{if } r(\mathbf{x}, t) < 0 \,, \end{cases} \quad . \tag{6.8}$$

For an afferent sensitive to the $-$ direction, the firing rate then takes the form of

$$F(\mathbf{x}, t) = \begin{cases} 2In - r(\mathbf{x}, t) & \text{if } r(\mathbf{x}, t) < In \,, \\ 0 & \text{if } r(\mathbf{x}, t) > In \end{cases} \tag{6.9}$$

where $r(\mathbf{x}, t)$ is either $r_{v\theta}(x_i, y_i, X, Y)$ or $r_{\Delta P}(x_i, y_i, X, Y)$.
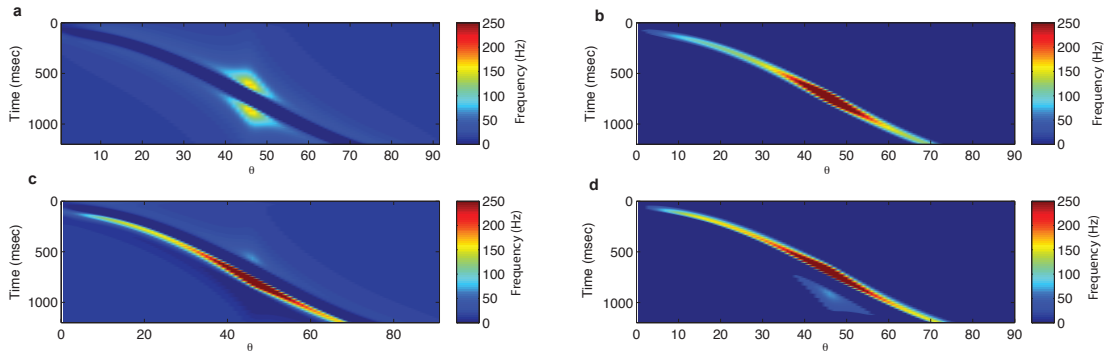
Figure 6.3: *Response of the afferent fiber to a sphere moving at 10 cm/s from head to tail.* **a** *response of a SN afferent sensitive to the water motion in the head to tail direction,* **b** *response of a SN afferent sensitive to water motion in the tail to head direction.* **c** *Response of a CN afferent sensitive to water motion in the head to tail direction and* **d** *in the tail to head direction.*

6.1.2 From Water Motion to Medulla Cells: the Medulla

As we noted earlier, the information between canal and superficial neuromasts is carried by different nerve fibers [50, 104, 105, 107]. Developmental studies on the zebrafish (*Danio rerio*) and tracing studies in goldfish *carassius auratus* [92] have shown that the afferents project to the medulla in a crude somatotopic manner. The position of the neuromasts along the antero-posterior axis (from head to tail) of the fish is represented by the central projection of the afferents [3, 64]. There is also evidence that fibers innervate hair cells of on average two and up to five consecutive neuromasts. When an afferent innervates more than one neuromast, the innervated neuromasts are nearly always consecutive, as expected if somatotopy is encoded in the system [107]. The fibers innervate *exclusively* hair cells of the *same* polarity [50, 107]. It is still unclear whether the information of differently tuned haircells is maintained in the projection pattern of the afferents i.e., if the orientation selectivity is maintained. However, maintaining this information would be beneficial for computational tasks like determining flow directions. That the afferents project separately in the MON is therefore a prediction of this model. There is also evidence that the input from the the CNs and SNs is processed, at least in part, separately [119].

Roots of the lateral-line nerves enter the ipsilateral brainstem and bifurcate into ascending and descending branches that terminate in the medial octavolateralis nucleus (MON) [11, 23, 100, 135] ; see for instance Fig. 1.3b that we have reproduced here for the convenience of the reader as Fig. 6.4, though there is probably a weak preservation of a somatotopy within the medulla [92]. The model we present here

can work without it if the detectors project in a somatotopic way to the medulla and there is no recurrent connectivity within the medulla,

$$
\begin{aligned}
r_{\mathrm{med}+}(\mathbf{x}, t) &= \int_0^t ds \{ C \cdot F_+(\mathbf{x}, t) \cdot \exp[-(t-s)/\tau_{\mathrm{exc}}] \\
&\quad -D \cdot F_-(\mathbf{x}, t) \cdot \exp[-(t-s)/\tau_{\mathrm{inhi}}] \} \quad (6.10) \\
r_{\mathrm{med}-}(\mathbf{x}, t) &= \int_0^t ds \{ C \cdot F_-(\mathbf{x}, t) \cdot \exp[-(t-s)/\tau_{\mathrm{exc}}] \\
&\quad -D \cdot F_+(\mathbf{x}, t) \cdot \exp[-(t-s)/\tau_{\mathrm{inhi}}] \} \quad (6.11)
\end{aligned}
$$

The integral over the past is important in the medulla for the inhibitory dynamics, since the firing rate becomes

$$
F(\mathbf{x}, t) = \begin{cases} r(\mathbf{x}, t) & \text{if } r(\mathbf{x}, t) > 0, \\ 0 & \text{if } r(\mathbf{x}, t) < 0, \end{cases} \quad (6.12)
$$

The careful anatomical study of the MON [100] shows that it is a three-layer network where inhibition plays an important role, the first two layers having inhibitory and excitatory synapses. The third layer has only excitatory synapses. There is also a small feed-back from the optic tectum (OT) directly to the MON. However, a clear somatotopic organization in the medulla cannot be proven. Within the MON these exists a great variability of responses. We do not attempt to make a full model of the medulla, since the same pattern occurs in several other animals where the first level of projection is understood to be for signal improvement only. What we need is a simple model reproducing a realistic input to the torus. To this end, we model directional cells in the medulla receiving input from the afferent nerves. One direction excites the medulla neuron and the opposite inhibits it, the time constant of the inhibitory synapse being longer than the excitatory one ($\tau_{exc} = 6\,\mathrm{ms}$ and $\tau_{inh} = 30\,\mathrm{ms}$). This model seems to explain well the pattern activity of two types of response already seen in the midbrain of fish, see for instance Figs. 4 and 6 in [45] and compare it with Fig. 6.4a (SN) for Fig. 4 (flow sensitive unit) and with Fig. 6.4 b for Fig. 6 (flow insensitive unit). There is a third type of cell in the medulla showing activity when there is no stimulus and being inhibited in the presence of a stimulus. We have not tried to model them here. One explanation for their behavior might be that these cells are involved in the production of the inhibitory signals.

6.2 Learning

Learning in neural networks takes place by changing the strength of connectivity between neurons. This assumption was first formulated by Donald Hebb[77]:
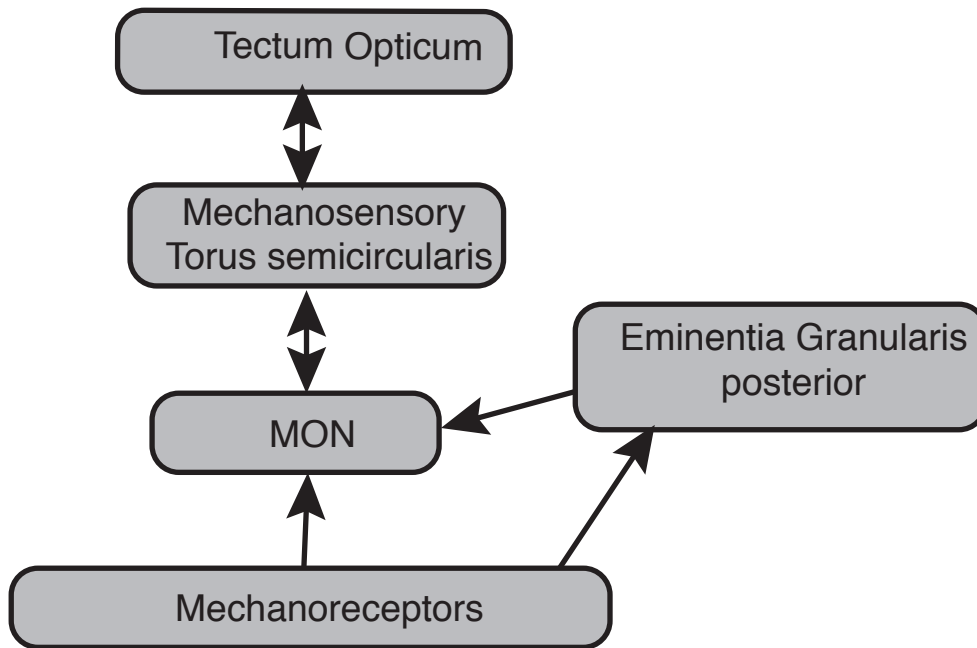
Figure 6.4: *Schematic view of the projection of the lateral line in the brain of teleost fish. The mechanoreceptors project by means of at least three different nerves in the medial octavolateralis nucleus (MON) of the metencephalon. Some afferents also terminate in the Eminentia Granularis posterior. The cell of the MON will project bi-directionally into the lateral portion of the Torus semicircularis and also bi-directionally into the deep layer of the Tectum opticum. Lateral-line information will also be processed from the torus and the tectum opticum to higher brain areas (picture redrawn from a sketch of Jacob Engelmann).*

Figure 6.5: *Response of medulla neurons receiving input from SNs (**a**,**b**) and from CNs (**c**, **d**) to a moving sphere as a function of time. **a** The medulla neuron (6.12) receives its excitatory input from afferent fibers sensitive to a water motion from head to tail. **b** from tail to head. The parameters are given in Table 6.1. **c** The medulla neurons receive their input from canal lateral-line afferents sensitive from head to tail **c** and from tail to head **d**. The stimulus is a translating sphere moving from head to tail on one side of the fish.*
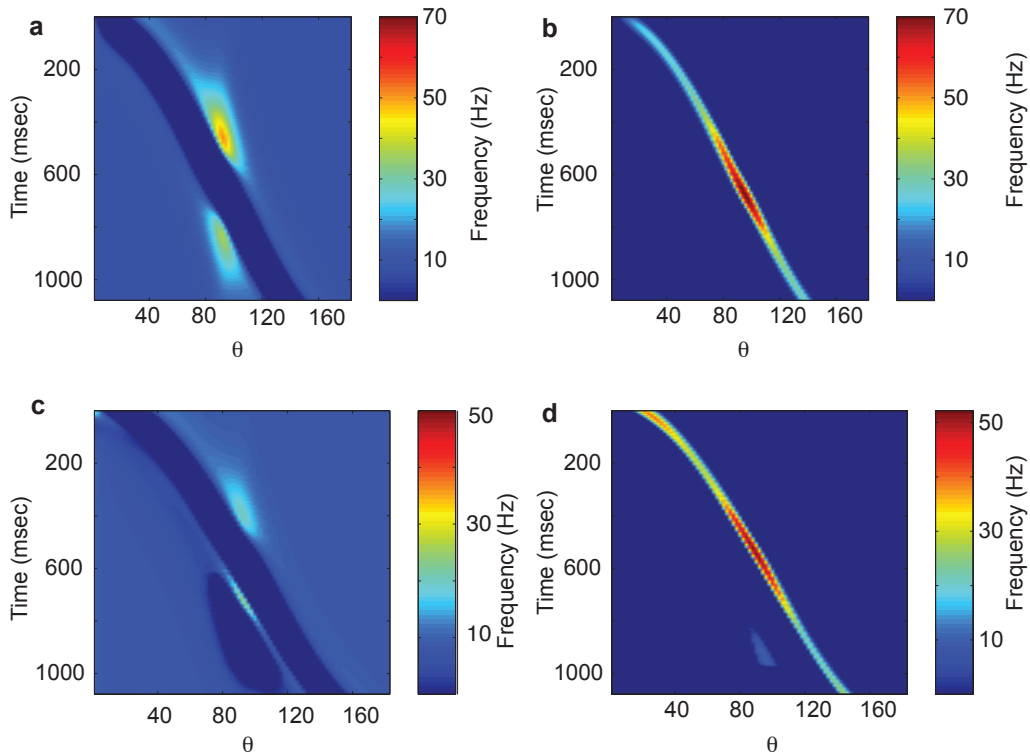
When an axon of cell A is near enough to excite cell B and repeatedly or persistently takes part in firing it, some growth process or metabolic change takes place in one or both cells such that As efficiency, as one of the cells firing B, is increased.

The biophysical process of learning goes beyond the goal of this PhD thesis. The reader is therefore referred to elsewhere[40, 63, 79]. In the last two decades, a lot of experimental evidence of Hebbian mechanisms at the single cell level has been found and is briefly reviewed in [1]. It is clear that relative timing plays a critical role in determining the sign and amplitude of the changes in synaptic efficacy produced by activity. Changes in synaptic strength involve both transient and long-lasting effect. Changes that persist for tens of minutes or longer are generally called long-term potentiation (LTP) and long-term depression (LTD). Synaptic plasticity occurs

Parameters	Values
Number of detectors N	180
Great axis of the elliptical fish a_{fish}	6 cm
Small axis of the elliptical fish b_{fish}	0.5 cm
Constant flow U	10 cm/s
Great axis of the elliptical trajectory of the sphere $a_{\text{sph.}}$	7 cm
Small axis of the elliptical trajectory of the sphere $b_{\text{sph.}}$	1.5 cm
Sphere radius r	5 mm
Instantaneous firing rate of the afferent In	15 Hz
Transfer parameter for the firing rate of SNs A	100
Transfer parameter for the firing rate of CNs B	6
Transfer parameter for the firing rate of medulla excitatory synapses C	20
Transfer parameter for the firing rate of medulla inhibitory synapses D	10
Time membrane constant for excitatory synapses τ_{exc}	10 ms
Time membrane constant for inhibitory synapses τ_{inhi}	40 ms

Table 6.1: *Default parameters for the biological input to the learning algorithm.*

only if the difference in pre- and post-synaptic spike time falls within a window of 50 ms. That means this kind of learning needs a great temporal precision. We have shown that this precision exists in the lateral line system of fish, see for instance Fig. 4.3. The form of the window can vary according to the system. We do not have experimental measurements on the connection between the medulla and the torus . Here we use a classical learning window coming from a similar system, the retinotectal synapses in the clawed frog *Xenopus laevis* [144]. It has been shown [59], however, that the exact geometry of the window does not strongly influence the learning process in the case of tuning of sensory input for multi-modal integration. The shape of the learning windows is given by

$$W(s) = \begin{cases} w^+ \frac{|s|}{(\tau^+)^2} \exp[-|s|/\tau^+] & s < 0\,, \\ w^- \frac{|s|}{(\tau^-)^2} \exp[-s/\tau^-] & s \geq 0\,. \end{cases} \tag{6.13}$$

Normally, simulating the spike dependence of synaptic plasticity requires a spiking model. An approximation, however, can be constructed by means of an *instantaneous* firing rate. This approximation will be most adequate if the neuron fires reliably and the time precision of the activity is highly reliable as well. I think it is the case here, since we can see in Fig. 4.1 that the response of the neuron to a frozen noise is highly reliable and that the coding fraction is easily destructed by a time jitter; (Fig. 4.3), meaning that the neuron encodes the stimulus precisely, that a stochastic process (single event, spike production) is not that important and a continuous rate

based on the instantaneous probability of having a spike at time t can explain the behavior rather well.

In the present case, the effect of pre- and postsynaptic timing can be incorporated into a synaptic timing, which can then be included in a synaptic modification rule. The average learning rule is therefore given by

$$
\begin{aligned}
\langle \Delta J_i \rangle \;\; = \;\; & \eta \int_{t}^{t+\mathcal{T}} \mathrm{d}t' \left[w^{\mathrm{in}} \langle S_i^{in} \rangle (t') + w^{\mathrm{out}} \langle S^{out} \rangle (t) \right] \\
& + \eta \int_{t}^{t+\mathcal{T}} \mathrm{d}t' \int_{t-t'}^{t+\mathcal{T}-t'} \mathrm{d}s \, W(s) \\
& \times \langle S_i^{\mathrm{in}}(t'+s) S^{\mathrm{out}}(t') \rangle \, .
\end{aligned}
\tag{6.14}
$$

If we consider our assumption stated earlier that the neuron responds reliably to the stimulus without having to integrate it over its past history, we can, as it has been done implicitly [40], say

$$
\langle S_i^{\mathrm{in}}(t'+s) S^{\mathrm{out}}(t') \rangle = S_i^{\mathrm{in}}(t'+s) S_j^{\mathrm{out}}(t') \, .
\tag{6.15}
$$

6.2.1 The Model with a Teacher

The synaptic weights between the medulla and the torus are set randomly between 0 and J_{max}. This means that we do not want any organization in the connection between the medulla and torus before learning. It is expected that some kind of (genetically?) rough somatotopy exists in the medulla. However, even if people look for it there is no proof of it (private communication of Horst Bleckmann and Jacob Engelmann). Here we consider the worst case in that the weight has to reorganize from a completely random distribution. Without the help of a teacher, the map will be based on the position of the detectors on the fish body. There is evidence that the visual signal will excite a few cells and inhibit the other cells. Inhibition has been shown to be very reliable for sensory tuning [59]. Then excitation seems to play a role since the map existing in the brain (as we will discuss later) does not seems to encode the position of the object in retina coordinates, but the place where the fish feels the water motion on its body. Since we need the teacher input to be zero far away from the position of the sphere (in order to permit theses weights to converge to zero during the learning and not to stay unchanged), we model the visual input by means of a mexican-hat wavelet of the form

$$
VT(\,\theta) = A_{vis} \left[1 - \frac{(\theta - \theta_{\mathrm{vis}})^2}{\sigma_{\mathrm{vis}}^2} \right] \exp \left[-\frac{(\theta - \theta_{\mathrm{vis}})^2}{\sigma_{vis}^2} \right]
\tag{6.16}
$$

$\theta_{\mathrm{vis}} = \cos^{-1}(x/a)$ being the visual angle of the object and θ the relative position of the cell in the torus map. The visual teacher is strong enough to saturate the cell

that it stimulates. The total input to the torus cell therefore takes the form of

$$S_i^{in} = \sum J_{(\theta_i, \theta_j)} F_{\text{Med}}(\theta, t) + VT(\theta) \,. \tag{6.17}$$

We are, however, putting a saturation condition $S_i^{in} = 250$ if $S_i^{in} > 250$, and the firing rate cannot become negative either.

Parameters	Values
Number of simulations	1 000 000
σ_{vis} width of the visual teacher	5°
x_{eyes}	$3\sqrt{2}\,\text{cm}$
y_{eyes}	$\pm 0.354\,\text{cm}$
η	10^{-4}

Table 6.2: *Default parameters for the learning algorithm.*

The simulations run in the following way. A moving sphere at a certain position and in a certain direction $(+, -)$, randomly chosen, is presented to the fish for 200 ms. The weights are then updated. The parameters are presented in Table 6.2.

6.3   Results and Discussion

The learning algorithm presented in the previous section enables a fish to reconstruct the somatotopic input coming from cells receiving input from CNs and SNs. The weight before learning is presented in Fig. 6.6a. After learning, the weight stabilizes to a certain value, as shown in Fig. 6.7, and it fits well the visual angle, Fig. 6.6b. The stimulation of the neurons by either flow-sensitive or flow-insensitive medulla input neurons gives rise to a somatotopic map respecting the visual geometry. The result is also consistent with the one presented by Plachta et al [119]. Our conclusion however is a bit different from that. They argue for somatotopy and a directional map for flow-insensitive units, but not for flow-sensitive ones. Both simulation and modeling lead to another conclusion. The map in the torus seems to encode *water motion* at the detectors but not the position of the object. That agrees with the function of the lateral line. The lateral line does not just encode the position of moving objects but it is also used in schooling, rheotaxis, and to follow vortex wakes. The position of the object does not enable the fish to record the information of such different sources in the same map. Spatially encoding the water disturbance at a certain position on the fish body, however, does.

The existence of a lateral-line map in the torus of fish [45, 119] is clear. It is also clear that in the optic tectum there is a map of cells sensitive to many

modalities (mechanosensory, auditory, visual and electric) [9] and that this map shows a retinoscopic geometry [78]. In the OT, the visuo-tectal topography in the goldfish *Carassius Auratus* is fairly linear. The point is 1 degree. in the visual field represents $8 - 20\mu$m on the tectal surface [139]. This means, however, that encoding an angle is not the natural coordinate for lateral-line detection. The natural coordinate system will be the position on the skin. In these coordinates, the position of the center of the excitation pattern will not change if we move the sphere perpendicular to the skin. However, the width of the curve and its intensity will. In retina coordinates the position of the angle will vary if we move the stimulus in direction perpendicular to the skin of the fish. It has already been shown that the response of the multimodal OT cell to a different modality will be different [9]. This agrees well with the geometry of the map we find here, showing that usually the same cell will fire roughly for the same position, but because of the form of the lateral-line stimulus not always.

The results of Catania et al [18], are also in good agreement with our theoretical model. They observed that the mechanoreceptors of the tentacle snakes *Erpeton tentaculus* are used to detect objects and that the map of the stimulus in the OT is in register with the visual representation, meaning that the response fields in the OT of both sub-modalities roughly match each other.
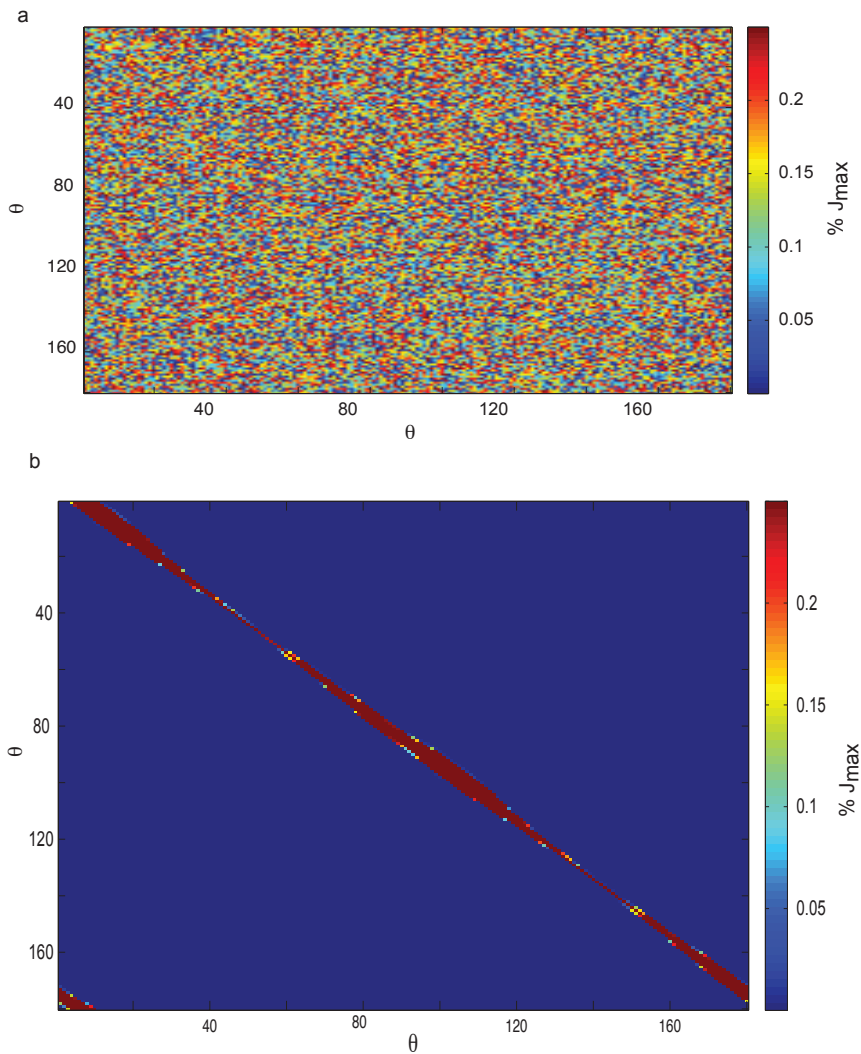
Figure 6.6: **a** *Synaptic weight distribution between medulla and Torus semicircularis before learning. The weights between the medulla neurons are set randomly between 0 and $J_{max} = 0.3$.* **b** *Connectivity between torus and medulla cells after learning. The medulla cells receive input from the afferent nerves (connecting the neuromasts) projected to the torus semi-circularis. In order to produce a map compatible with the retinal representation, a signal from the optic tectum modifies the connection between the cell in the tectum and the medulla. Since the input of the torus does not come from the detector, we have first modeled how the water displacement at the detectors is encoded in the medulla.*
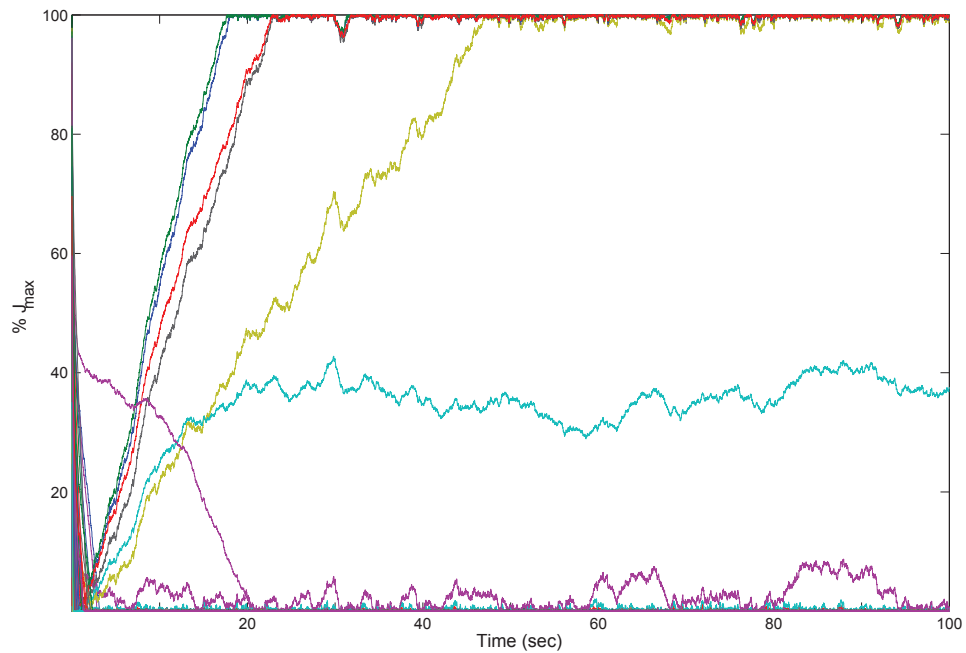
Figure 6.7: *Weight convergence during learning. A learning session was composed of trials of duration 0.2 sec for a complete session of 100 sec. At each trial the weights of the cells were modified according to the time-dependent plasticity rule given by (6.14). Different colors indicate the synaptic change of efficacies on different cells*
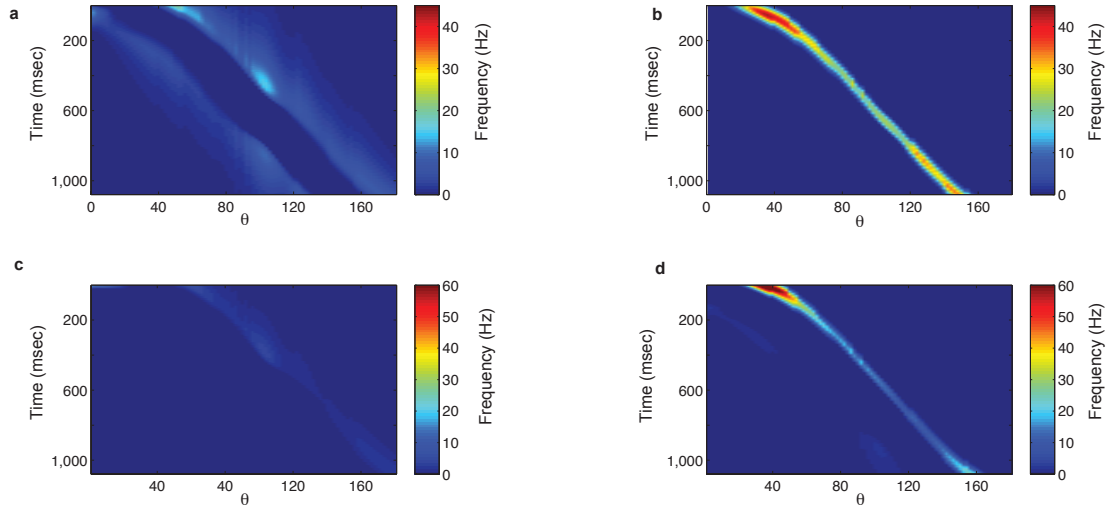
Figure 6.8: *Response of torus neurons as a function of time receiving their input from flow-sensitive medulla cells (most probably innervated by SNs) (**a**,**b**) and from flow-insensitive cells mostly probably innervated by CNs (**c**, **d**). The stimulus is a translating sphere moving from head to tail on one side of the fish. The vertical axis is the time axis while the horizontal one indicates the angular position of the neuromast on the fish body. **a** The torus neuron (6.12) receives its excitatory input from medulla cells sensitive to a water motion from head to tail; **b** from tail to head. The parameters are given in table 6.1. **c**. The torus neurons receive their input from medulla cells getting innervated by cells sensitive from head to tail **c** and from tail to head **d**.*

7. Discussion and Conclusion

In this chapter, we will try to put this thesis into a more general context in the research done in neuroscience, ethology and computational neuroscience. We will also propose new research paths for lateral-line research.

In view of the multifaceted aspects of our results, we will first list the major results of the present dissertation and then discuss them from a historical perspective. The discussion will be divided into two major parts: we will first discuss the results regarding the *encoding* followed by the results regarding the *decoding*. Throughout this dissertation and hence also throughout what follows we discuss the response of the lateral-line afferent nerves to a variety of stimuli and how this response is possibly integrated in the brain of teleost fishes. Finally, we will briefly propose new research paths for lateral-line research.

7.1   Main Results of this Dissertation

The results of this dissertation can be split into two categories. We have first studied the *encoding* performed by the lateral-line neuromasts and the firing pattern at the afferent nerves. Our main purpose was to show that the boundary-layers and the form of the fish do not influence the firing pattern of the afferent nerves and that we can model the activity at the neuromast by mean of the Euler equation and a straight line of detectors. In terms of *decoding*, we have also shown that the distance perpendicular to the line of detectors is available to the fish through a simple mechanism based on the distribution of the simulation pattern on the fish body and

that the linearity of dependence upon the distance between the maxima/minimum or zeros of the velocity (or pressure) field is preserved even if the afferent nerves project to the MON with a large dendritic arborization. We have then studied the integration of the signal from the afferents to the optic tectum have shown that we can reproduce the activity of the neurons in the medulla and the torus by means of a learning rule based on STDP.

In chapter 1, we reviewed the biological knowledge available about the lateral-line from the periphery towards its integration in the fish brain.

In chapter 2, we set a physical and a mathematical framework for the rest of the dissertation, showing that the pressure in the boundary layers stays constant and that the stimulation pattern is not really affected by the turbulence present in the boundary layer (sect. 2.2) In the same chapter, using the formalism suggested by Hassan [73, 74, 75, 76] and based on theoretical work done by Keller and coworkers [62, 68] we showed that the form of the fish body does not influence the stimulation pattern; see Fig. 2.6.

In chapter 3, we proposed a *minimal* model based on a straight line of detectors and the Euler equation at the detectors. We showed that this leads to a coherent representation fitting well the experimental data for a variety of stimuli: a dipolar stimulus (sect. 3.1), a translating sphere (sect. 3.2) and even wakes produced by other fish while swimming (sect. 3.3). We also showed that surface neuromasts (SN) may encode a stimulus well even in presence of a background flow (Fig. 3.3 d).

Chapter 4, is devoted to the study of the SN's response to a band-pass white noise. In this chapter, we showed that the response of SN to a white noise stimulus is highly reproducible (Fig. 4.1) and that incorporating a small jitter to the response has *huge* impact on the coding fraction (Fig. 4.3). We interpreted it by saying that the neuromasts have a small membrane integration time and that the firing rate is high enough so that the stochasticity due to spike production would not play an important role. We then reconstructed the Wiener filter and showed that the filter has the shape of a *velocity* filter. Using PCA (principal component analysis) applied to the covariance matrix, we found that the spike production is driven by two independent modes: the first is again a velocity filter and the second is an acceleration filter but its effect on spike production seems to be rather moderate; see Fig. 4.6. We finally constructed the instantaneous (without adaption) FI (firing frequency of the afferent function of the intensity of the stimulus).

In chapter 5, we showed that the distance algorithm based on the "depth" of the curve (minima and maxima, or zeros) is robust to curvature, that it converges to the straight-fish case rather slowly, but since most fish are almost straight, the

effect is not that big. We checked this with data coming from real fish. We also showed that the form of the object *to be detected* has a really small effect on distance determination. Moreover, we showed that this scaling is preserved in the brain even if the afferent central arborization in the medial octavolateral-line nucleus of the medulla is large.

Chapter 6 is devoted to integration and map formation. We argue that the available experimental data are in favor of a retinotopic map in the torus of fish, and show that by easy modelling and STDP learning through a visual teacher we can adjust the lateral-line stimulus onto a retinotopic grid. Our modeling is in accordance with experimental work of Engelmann and Plachta [45, 119].

7.2 Encoding

Lateral line analysis has a long history culminating in a first review by Sven Dikj-graaf [42]; see also the great collection of essays in [32], in particular those by Kalmijn and Hassan, the detailed mathematical analysis of Hassan [73, 74, 75, 76], and Bleckmann's succinct monograph [10] combining biological data and physical understanding.

There are also several studies addressing questions similar to those analyzed here, starting with [71] and [126], continuing with [33] and most recently, [56] and [38]. Though Coombs et al. [25, 26, 27, 28, 29, 30, 31, 33, 37] have analyzed an impressive collection of data, we are facing several, partially inconsistent, conclusions. The inconsistency is mainly due to the fact that these authors have not analyzed the *physics* of the problem in sufficient detail. Their insight, however, that only the near flow field can communicate outside information to the lateral line has certainly stimulated a lot of recent work including the present dissertation.

All previous studies were based on the classical statement that the most efficient stimulus to superficial neuromasts is the velocity at the skin of the fish. Physiological evidence for this has been found and resulted in the assumption that superficial neuromasts (SN) only function in conditions of low-background flow [47].The result of Fig. 3.3d shows this is not quite the case. SNs can encode well a nearby dipole even in a flow of 10 cm/s and even if the flow significantly increases the firing of the cells. We have used the same algorithm to show that the neuromasts can precisely encode the water disturbance created by a vibrating sphere and even wakes left behind by other fish while swimming. We were also interested in how lateral-line neuromasts follow a band-pass white-noise. We showed that lateral-line neuromasts can follow white noise in a really reproducible way (see Fig. 4.1) and also that time

jitter will rapidly break the encoding of SNs (see Fig. 4.3). That means that our results are similar to the one of Mainen of Sejnowsky [99]. To us, however it means that the detector can follow the stimulus well and that stochasticity due to spike production is negligible. The level of activity can, therefore, be explained by the instantaneous spiking probability.

A study by Kalmijn [87] propose that surface neuromasts are not exactly sensitive to velocity but to a mixed signal of velocity and acceleration (fractional derivative). By applying information-theoretical approaches to the lateral line system, we try to solve these partially contradictory results. To do so, we apply reverse correlation using either the linear reverse correlation approach, or a covariance analysis that is not limited to a single filter. The advantage of the latter is that it does not a priori limit the number of stimuli that a neuron is responsive to. To our knowledge, this is the first study that quantifies the responses of the mechanosensory lateral-line afferent nerves in the framework of an information-theoretical approach.

In order to answer the question if SNs respond to velocity alone, we used the covariance analysis. Similarly to several other studies [14, 67, 133], we found a maximum of two relevant eigenvectors (but see [49] for more complex examples) where the second eigenvector resembled the derivative of the spike triggered average (STA). While the first eigenvector clearly resembled the STA, the meaning and relevance for information processing of the second eigenvector is less obvious. One hypothesis [39] as to why the second eigenvector is the derivative of the STA is that time jitters can induce additional relevant eigenvectors (with derivative-like structure and significant eigenvalue-level.) if they are on a similar temporal scale as the features of the eigenvectors themselves. For the lateral-line afferent nerves, we have shown that spike-time jitter of 3.5 ms decreases the stimulus reconstruction by 70%. This is a much shorter time scale than that of the eigenvectors. Hence, it is unlikely that intrinsic jitter is the cause of the occurrence of eigenvectors that are the first derivative of the STA. On the other hand, it has also been proposed [5, 6] that the presence of a second eigenvector similar to the first derivative of the first one is an intrinsic property of the Hodgkin Huxley equation making neurons sensitive to a mix of velocity and acceleration.

In the case of SNs, however, another hypothesis is that SNs are sensitive to a mix of velocity and acceleration [84, 87] because they are driven by the water velocity within the boundary layer. Jielof et al. [84] were the first to study the biophysics of lateral-line detection and they already noted a frequency dependency of the boundary layer. Kalmijn [87] explained it was due to the fact that within the boundary layer the viscous force is not negligible. The viscous term is proportional to the negative pressure gradient and, therefore, the acceleration. The thickness of the boundary is defined as the zone around a cupula where the viscous force constitutes above

one percent of the net force acting on the cupula [128]. Outside the boundary layer the inertial force dominates. The viscous force (proportional to acceleration) does increase faster with the stimulus frequency than the inertial force; when applying a dipole stimulus, for example, the inertial force increases proportionally to the frequency whereas the viscous force increases with the square of the frequency. Thus at low frequencies the cupula is driven by the velocity of the water deep within the boundary layer, which is proportional to a combination of the velocity and the acceleration of water volume. As frequency increases, the boundary layer becomes progressively thinner and the velocity driving the cupula approaches the velocity of the surrounding water. Since the SNs respond as a low-pass filter to the external velocity, they are likely to encode peripheral stimuli in a mixed regime of velocity and acceleration. The second vector we found seems to encode acceleration. Our conclusion is however that this vector does not play an important role regarding spike production; see Fig. 4.6.

7.3 Decoding

The work on encoding shows how lateral-line detectors encode water motion. However, a more important question still remains: How can a fish use this kind of signal to get information about its environment? In this respect, the present dissertation focuses on two problems. First, we study a mechanism based on the depth of the stimulation field on the fish to determine the distance perpendicular to the detectors and, second, we construct a model to show the lateral-line can produce a map of the water motion around a fish body that is compatible with the multimodal map existing in the optic tectum.

Franosch et al [56] were the first to unequivocally show that the distance between the zeros or between maxima and minima of the velocity field encodes the spatial distance D between an aquatic stimulus and fish. In particular, the distance between *characteristic* lines of the velocity field on the fish body scales with D with a prefactor of order 1. If, for instance, fish would encode the distance D to a prey by the distance between maxima and minima of the near flow field, scaling with D, then they need to be able to *detect* both maximum and minimum. If however D is too large, exceeding one fish length, then the information is incomplete. Encoding D is no longer possible, and hence, distance determination in higher brain centers is no longer possible either. These aspects concerning the maxima and minima would hold equally well for the two zeros of the dipolar velocity field; see below. Moreover, natural explanation of the "short" range of the lateral-line system as "about one fish length" in fact justifies a criterion that has been known to biological tradition for a long time[71, 126] and it has meanwhile been confirmed theoretically [131]. Though the above theoretical evidence was quite compelling, physiological evidence for a *precise* estimate in terms

of the near-flow field was still missing.

Here it is important to specify to the readers that the minimum refers to a maximum in the opposite direction to that of the maximum. To *feel* opposite directions, there are two distinct populations of hair cells that are innervated with two different axons; cf. Fig. 1.1c.

Analyzing extracellular receptor potentials (ERPs), also called microphonic potentials, which arise from the collective mechano-transduction of hair cells in single neuromasts, Ćurčić-Blake and van Netten [38] have shown that the above criterion of zeros of the velocity field scaling with D indeed holds for ERPs, thus providing a first experimental confirmation of this theoretically attractive idea. On the other hand, their interpretation of the ERP data in terms of a wavelet read-out is questionable since it is unclear why, and how, fish should use such a complicated mathematical procedure. Things also work simply and straightforwardly in biological terms, a key result of the present dissertation. We have also proven that this scaling holds even if the object to be detected is not exactly circular and that the approximation becomes really good as soon as the prey is at one *prey length* distance or more.

We have also seen that the linear relation is preserved even if the afferent central arborization in the medial octavolateral-line nucleus of the medulla is large. It has already been shown for the case of electric fish that the depth and the maximum can be extracted by neural nets [96]. Since the distance between the maxima or the zeros are just points that already scaled, any other scaled point (1/2 of the maximum intensity, as in the case of electric fish) will be scaled linearly with distance. We therefore show here that the mechanism can be well integrated in the brain. This scaling is, to a large extent independent of the form of the *prey*; see Figs. 5.5 and 5.6.

In the next to last chapter, we try to give a coherent framework leading to the production of maps in the torus of fishes. The lateral-line detectors are spread all over the body of the fish. As we say in the introduction, but repeat for reasons of clarity and the benefit of the reader, developmental studies on the zebrafish (*Danio rerio*) and tracing studies in goldfish *Carassius auratus* [92] show that the afferent nerves project to the medulla in a crudely somatotopic manner. The position of the neuromasts along the antero posterior axis (from head to tail) of the fish is represented in the central projection of the afferent nerves [3, 64]. There is also evidence that fibers innervate hair cells of, on average, two and up to five, consecutive neuromasts. When an afferent innervates more than one neuromast, the innervated neuromasts are nearly always consecutive, as expected if somatotopy is encoded in the system [107]. The fibers innervate *exclusively* hair cells of the *same* polarity [50, 107]. It is still unclear whether information of differently tuned haircells is

maintained in the projection pattern of the afferent, i.e., if the orientation selectivity is maintained. Our results show clearly that maintaining this information would be beneficial to computational tasks such as determining flow directions.

Electrophysiologically, the response of the medulla cells is rather unclear. Cells seem to answer to a specific place and to be directional, i.e., just answering to the flow in one direction. As we noted earlier, the afferent nerves project to the medial octavolateralis nucleus (MON) in a double somato-topic way. Inhibition seems to play an important role in the MON and no recurrent connectivity has been found yet (Engelmann, private communication). It is unclear if a true somatotopy exists in the medulla. Some studies point out the existence of crude somatotopy for some species [11, 135] but it is really crude. A suitable hypothesis explaining all this would be that cells migrate over a subset preset by genetics. Here, we show that learning does not need any somatotopic organization in the MON since the weights between the MON and the torus were set randomly at the beginning. The key criterion according to our modelling is that the afferent sensitive to one direction excites the cells, whereas the afferent sensitive to the other direction inhibits them. This connectivity pattern is in accordance with the electrophysiological results [48, 92, 93, 101].Even in the afferent cells answer to many different stimuli in the medulla, they seems to exist answering *only* to a translating or to a vibrating sphere. One hypothesis is that cells answering to a vibrating sphere may be sensitive to the position of the center of mass of the stimulation. The present work does not have the ambition to give a complete overview of the huge variety of responses existing, and probably much more experimental work should be performed in order to understand well the response of the cells in the medulla (for that see the next section 7.4). For other animals, such as the clawed frog *Xenopus laevis*, that map the direction of surface waves, an organized map emerges only in the torus [24, 57].

In the optic tectum, the cells are multimodal and respond to visual, mechanosensory, and auditory stimuli [9]. The projections between torus and optic tectum are topographically matched [138, 139]. This means that the lateral-line map in the torus and the multi-modal map in the optic tectum should have an organization compatible with each other. The possibility of tuning multimodal maps by means of a visual teacher has already been studied [39, 58, 59]. The later two studies show that an inhibitory signal from the visual system seems to be the most robust teacher. In the case of the visual feedback from the optic tectum to the torus, its seems to be a bit different as there is evidence that the signal excites the cell at the position of the sphere and will inhibit the others around it. We therefore use a Mexican hat wavelet as the teacher function rather then a Gaussian one. This can help the learning mechanism since the lateral-line signal is much lower and less clear than the visual signal. The visual field of fish is large. One can expect that fish are able to cover the complete 360°. This compatibility between the signal coming from

mechanosensory (lateral-line-like) detectors and vision in the torus and the optic tectum has also been observed for the mechanoreceptors on the appendage of the tentacle snake *Erpeton tentaculatus* [18]. The work shows that a tentacle snake uses its appendage to detect objects with mechanosensors and that the map in the optic tectum fits well the visual representation, meaning that the fields of the response modalities approximately match each other, i.e,are similar to what has been observed in the case of the electric fish which we discussed earlier [9].

7.4 Future Paths

I think the work of this dissertation mathematically describes and explains, what happens at the afferent nerves. I think, with the actual knowledge we have, the most important aspect is to work *precisely* on how the information is integrated into the neural circuit. One way will be to focus on a single species. In this regard, the zebra fish (*Danio rerio*) is the most suitable animal since its physiology, neuroanatomy, and genetics are well known. In this regard, it will be very important to characterize the response of the cells in term of the water motion at the detectors and not in terms of object position as it was often done [94]. It will also be important to determine the local connectivity. As I have shown in this dissertation the key point is that the lateral-line map in the torus seems to map the water motion at the detectors and not the position of the object itself. I therefore suggest that future efforts should in particular combine the hydrodynamics due to water disturbance at the detectors with the response of the cells in the brain. That can only be done by combining electrophysiology with flow measurement of the stimulus through particle image velocimetry and a theoretical analysis of hydrodynamics flow.

Bibliography

[1]   Abbott, LF & Nelson, SB (2000) Synaptic plasticity: Taming the beast, Nat Neurosci **3** 1178–1183.

[2]   Acheson, DJ (1990) *Elementary Fluid Dynamics* (Clarendon Press, Oxford).

[3]   Alexandre, D & Ghysen, A (1999) Somatopy of the lateral line projection in larval zebrafish, Curr Opin Neurobiol **96** 7558–7562.

[4]   Anderson, E, McGillis, W, & Grossenbaugh, M (2001) The boundary layer of swimming fish, J Exp Biol **204** 81–102.

[5]   Aguera y Arcas, B & Fairhall, AL (2003) What causes a neuron to spike?, Neural Comput **15** 1789–1807.

[6]   Aguera y Arcas, B, Fairhall, AL, & Bialek, W (2003) Computation in a single neuron hodgkin and huxley revisited, Neural Comput **15** 1715–1749.

[7]   Atema, J, Fay, RR, Popper, AN, & Tavolga, WN (editors) (1988) *Sensory Biology of Aquatic Animals* (Springer, New York).

[8]   Bartels, M, Münz, H, & Claas, B (1990) Representation of lateral line and electrosensory systems in the brain of axolotl *Ambystoma mexicanum*, J Comp Physiol A **167** 47–356.

[9]   Bastian, J (1982) Vision and electroreception: Integration of sensory information in the optic tectum of the weakly electric fish *Apteronotus albifrons*, J Comp Physiol **147** 287–297.

[10]   Bleckmann, H (1994) *Reception of Hydrodynamic Stimuli in Aquatic and Semiaquatic Animals* (Fischer, Stuttgart).

[11]   Bleckmann, H (2006) The lateral line system of fish, in T Hara & B Zielinsky (editors), *Fish Physiology. Sensory System Neuroscience*, pp. 411–453 (Elsevier, Amsterdam).

[12]   Bleckmann, H (2008) What is the nature of multisensory interaction between

octavolateralis sub-systems?, J Comp Physiol A **194** 145–158.

[13] Bleckmann, H, Weiss, O, & Bullock, TH (1989) Physiology of lateral line mechanoreceptive region in elasmobranch brain, J Comp Physiol A **164** 459–474.

[14] Brenner, N, Bialek, W, & de Ruyter van Steveninck, R (2000) Adaptative rescaling maximizes information transmission, Neuron **26** 695–702.

[15] Broer de, E & Kuyper, P (1968) Trigered correlation, IEEE Trans Biomed Eng **15** 169–179.

[16] Buttler, AB & Hodos, W (2005) *Comparative Vertebrate Neuroanatomy* (John Wiley and Son, Hoboken).

[17] Campenhausen, C, Riess, I, & Weissert, R (1981) Detection of stationary objects by the blind Cave Fish *Anoptichthys jordani* (Characidae), J Comp Physiol A **143** 369–374.

[18] Catania, KC, Leitch, DB, & D, Gauthier (2010) Function of the appendages in the tentacled snakes (*Erpeton tentaculatus*), J Exp Biol **213** 359–367.

[19] Chacron, MJ (2006) Nonlinear infromation processing in a model sensory system, J Neurophysiol **95** 2933–2946.

[20] Chagnaud, BP, Bleckmann, H, & Hofmann, MH (2007) Kármán vortex street detection by the lateral line, J Exp Biol **209** 753–763.

[21] Chagnaud, BP, Bleckmann, H, & J, Engelmann (2006) Neural response of goldfish lateral line afferent to vortex motion, J Exp Biol **209** 327–342.

[22] Chorin, AJ & Mardsen, JE (editors) (1990) *A Mathematical Introduction to Fluid Mechanics* (Springer, New York).

[23] Claas, B & Münz, H (1981) Projection of lateral line afferents in a teleost brain, Neurosci Lett **23** 231–235.

[24] Claas, B., Münz, H., & Görner, P. (1993) Reaction to surface waves by *Xenopus laevis* Daudin. Are sensory systems other than the lateral line involved?, J. Comp Physiol **172(6)** 759–765.

[25] Conley, RA & Coombs, S (1998) Dipole source localization by mottled sculpin. iii. orientation after site-specific, unilateral denervation of the lateral line system, J Comp Physiol **183(3)** 335–344.

[26] Coombs, S (1994) Nearfield detection of dipole sources by the goldfish (*Carassius aurus*) and the mottled sculpin (*Cottus bairdi*)., J Exp Biol **190(3)** 109–129.

[27] Coombs, S (1999) Signal detection theory, lateral-line excitation patterns and prey capture behaviour of mottled sculpin, Animal Behavior **58** 421–430.

[28] Coombs, S, Braun, CB, & Donovan, B (2001) The orienting response of lake michigan mottled sculpin is mediated by canal neuromasts., J Exp Biol **204** 337–348.

[29] Coombs, S & Conley, RA (1997) Dipole source localization by mottled sculpin. I. approach strategies, J Comp Physiol **180(4)** 387–399.

[30] Coombs, S & Conley, RA (1997) Dipole source localization by the mottled

sculpin. II. the role of lateral line excitation patterns, J Comp Physiol **180(4)** 401–415.

[31] Coombs, S, Finneran, JJ, & Conley, RA (2000) Hydrodynamic image formation by the peripheral lateral line system of the Lake Michigan mottled sculpin, *Cottus bairdi*, Phil. Trans. R. Soc. Lond. B **355(1401)** 1111–1114.

[32] Coombs, S, Görner, P, & Münz, H (editors) (1989) *The Mechanosensory Lateral Line: Neurobiology and Evolution* (Springer, New York).

[33] Coombs, S, Hastings, M, & Finneran, J (1996) Modeling and measuring lateral line excitation patterns to changing dipole source locations, J Comp Physiol A **178(3)** 359–371.

[34] Coombs, S & Janssen, J (1990) Behavioral and neurophysiological assessment of lateral line sensitivity in the mottled sculpin, *Cottus bairdi*, J Comp Physiol A **167** 557–567.

[35] Coombs, S, Janssen, J, & Webb, JF (1988) Diversity of lateral line systems: evolutionary and functional considerations, in J Atema, RR Fay, AN Popper, & WN Tavolga (editors), *Sensory Biology of Aquatic Animals*, pp. 267–294 (Springer, New York).

[36] Coombs, S, Mogdans, J, Halstead, M, & Montgomery, J (1998) Transformation of peripheral inputs by the first-order lateral line brainstem nucleus, J Comp Physiol A. **182** 609–626.

[37] Coombs, S & Patton, P (2009) Lateral line stimulation pattern and prey orientation behavior in the Lake Michigan mottled sculpin *Cottus Bairdi*, J Comp Physiol A **195(3)** 279–297.

[38] Ćurčić-Blake, B & van Netten, SM (2006) Source location encoding in the fish lateral line canal, J Exp Biol **209** 1548–1559.

[39] Davison, AP & Frégnac, Y (2006) Learning cross-modal spatial transformation through spike timing dependent plasticity, J. Neurosci. **26** 5604–5615.

[40] Dayan, P & Abbott, LF (2001) *Computational and Mathematical Modeling of Neural Systems* (MIT Press, Cambridge).

[41] Denk, W, Holt, JR, Shepherd, GMG, & Corey, DP (1995) Calcium imaging of single stereocilia in hair cells: localization of transduction channels at both ends of tip links, Neuron **15** 1311–1321.

[42] Dikjgraaf, S (1962) The functioning and significance of the lateral line organs, Biol Rev **38** 51–105.

[43] Ding, C & He, X (2004) K-means clustering via principal component analysis, in *International Conference on Machine Learning* (Banff).

[44] Eatock, RA, Richard, FR, & Popper, AN (editors) (2006) *Vertebrate Hair Cells* (Springer, New York).

[45] Engelmann, J & Bleckmann, H (2003) Coding of lateral line stimuli in the goldfish midbrain in still and running water, Zoology (Jena) **107** 135–151.

[46] Engelmann, J, Hanke, W, & Bleckmann, H (2002) Lateral line reception in still and running water, J Comp Physiol A **188** 513–526.

Bibliography

[47] Engelmann, J, Hanke, W, Mogdans, J, & Bleckmann, H (2000) Hydrodynamic stimuli and the fish lateral line, Nature **408(6808)** 51–52.

[48] Engelmann, J, Kröther, S, Bleckmann, H, & Mogdans, J (2003) Effects of running water on lateral line responses to moving objects, Brain Behav Evol **61** 195–212.

[49] Fairhall, AL, Burlingame, A, Naramishan, R, Harris, R, et al. (2006) Selectivity for multiple stimulus feature in retinal ganglion cells, J Neurophysiol **96** 2724–2738.

[50] Faucherre, A, Pujol-Marti, J, Kawakami, K, & Schier-López, H (2009) Afferent neurons of the zebrafish lateral line are strict selectors of hair-cell orientation, PLOS One **4** 1–12.

[51] Flock, Å (2004) The lateral line organ mechanoreceptors, in W Hoars & D Randall (editors), *Fish physiology, vol 5*, pp. 241–263 (Academic, New York).

[52] Flock, Å & Wersäll, J (1962) A study of the orientation of the sensory hair of the receptor cells in the lateral line organ of sh, with special reference to the function of the receptors, J Cell Bioll **15** 19–27.

[53] Flock, Å & Wersäll, J (1965) Transducing mechanisms in the lateral line canal organ, Cold Spring Harb Symp Quant Biol **30** 133–145.

[54] Franosch, JMP, Hagedorn, HJA, Goulet, J, Englemann, J, et al. (2009) Wake tracking and the detection of vortex ring by the canal lateral line of fish, Phys Rev Lett **103** 0781 021–0721 024.

[55] Franosch, JMP, Lingenheil, M, & van Hemmen, JL (2005) How a frog can learn what is where in the dark, Phys Rev Lett **95** 078 106.

[56] Franosch, JMP, Sichert, AB, Suttner, MD, & van Hemmen, JL (2005) Estimating position and velocity of a submerged moving object by the clawed frog and fish - a cybernetic approach, Biol Cyb **93** 231–238.

[57] Franosch, JMP, Sobotka, MC, Elepfandt, A, & van Hemmen, JL (2003) Minimal model of prey localization through the lateral-line system, Phys Rev Lett **91** 1581 011–1581 014.

[58] Friedel, P (2008) *Sensory Information Processing Detection, Feature Extraction and Multimodal Integration*, Phd thesis, Technische Universität München, München.

[59] Friedel, P & van Hemmen, JL (2008) Inhbition, not excitation is the key to multimodal sensory integration, Biol Cybern **98** 597–618.

[60] Gabbiani, F & Koch, C (1998) Principles of spike train analysis, in O. Ottoson (editor), *Method in Neuronal Modeling: From Synapses to Networks*, pp. 313–360 (MIT Press, Cambridge).

[61] Gabbiani, F, Metzner, W, & Koch, C (1996) From stimulus encoding to feature extraction in weakly electric fish, Nature **384**.

[62] Geer, J F (1975) Uniform asymptotic solutions for potential flow about a slender body of revolution, J Fluid Mech **67** 131–147.

Bibliography

[63] Gerstner, W & W, Kistler (2002) *Spiking Neuron Models* (Cambridge University Press, Cambridge).

[64] Ghysen, A & Dambly-Chaudière, C (2004) Development of the zebrafish lateral line, Curr Opin Neurobiol **14** 67–73.

[65] Goulet, J, Engelmann, J, Chagnaud, BP, Franosch, JMP, et al. (2008) Object localization through the lateral line system of fish: theory and experiment, J Comp Physiol A pp. 1–17.

[66] Gray, J (1933) Studies in animal locomotion III The propulsive mechanism of the whitting(*Gadus Marlangus*), J Exp Biol **10** 391–402.

[67] Gussin, D, Benda, J, & Maler, L (2007) Limits of linear rate coding of dynamic stimuli by electroreceptor afferents, J Neurophysiol **97** 2917–2929.

[68] Handelsman RA, Keller JB (1967) Axially symmetric potential flow around a slender body, J Fluid Mech **28** 131–147.

[69] Hanke, W & Bleckmann, H (2000) The hydrodynamic trail of *Lepomis gibbosus* (centrarchidae), *Colomesus psittacus*(Tetraodontidae) and *Thysochromis ansorgii* (Cichlidae) investigated with scanning particle image velocimetry, J Exp Biol **207** 1585–1596.

[70] Hanke, W, Brcker, C, & Bleckmann, H (2000) The ageing of the low-frequency water disturbance caused by the swimming goldfish and its possible relevance to prey detection, J Exp Biol **203** 1193–1201.

[71] Harris, GG & Bergeijk, JD (1966) Evidence that the lateral line organ responds to near-field displacements of sound sources in water., J Acous Soc Am. **34(1)** 1831–1841.

[72] Hartline, PH, Kass, L, & Loop, MS (1978) Merging of modalities in the optic tectum: Infrared and visual integration in rattlesnakes, Science **199** 1225–1229.

[73] Hassan, ES (1985) Mathematical analysis of the stimulus for the lateral line organ, Biol Cybern **52(1)** 23–36.

[74] Hassan, ES (1992) Mathematical description of the stimuli to the lateral line system derived from a three dimensional flow field analysis. I. the case of moving in open water and of gliding toward a plane surface, Biol Cybern **66** 443–452.

[75] Hassan, ES (1992) Mathematical description of the stimuli to the lateral line system derived from a three dimensional flow field analysis. II. the case of gliding alongside or above a plane surface, Biol Cybern **66** 443–452.

[76] Hassan, ES (1993) Mathematical description of the stimuli to the lateral line system derived from a three-dimensional flow field analysis. III. the case of an oscillating sphere near the fish, Biol Cybern **69** 523–538.

[77] Hebb, DO (1949) *The Organization of Behaviour: A Neuropsychological Theory* (John Wiley & Sons, New York).

[78] Heiligenberg, W & Rose, GJ (1987) The optic tectum of the gymnotiform electric fish, eigenmannia: labeling of physiologically identified cells., Neuroscience **22** 331–340.

Bibliography

[79] Hemmen, JL van (2001) Theory of synaptic plasticity, in F Moss & S Gielen (editors), *Handbook of Biophysics , Vol. 4.*, pp. 771–783 (Elsevier, Amsterdam).

[80] Howard, J & Hudspeth, AJ (1988) Compliance of the hair bundle associated with gating of mechanoelectrical transduction channels in the bullfrogs saccular hair cell., Neuron **1** 189–199.

[81] Hudspeth, AJ, Chloe, Y, Metha, AD, & Martin, P (2000) Putting ion channels to work: mechanoelectrical transduction, adaptation, and amplification by hair cells., Proc Nat Acad USA **97** 11 765–11 772.

[82] Janssen, J, Coombs, S, Hoekstra, D, & Platt, C (1992) Feeding and orientation of mottled sculpin *Cottus bairdi* (scorpaemiformes:Cottidea), Copeia pp. 485–492.

[83] Janssen, J & Corcoran, J (1998) Distance determination via the lateral line in the mottled sculpin, Copeia pp. 657–661.

[84] Jielof, R, Spoor, A, & de Vries, H (1952) The microphonic activity of the lateral line, J Physiol (London) pp. 116–137.

[85] Jones, LM, Depireux, DA, Simons, DJ, & Keller, A (2004) Robust temporal coding in the trigeminal system, Science **304** 1986–1990.

[86] Jørgensen, JM & Flock, Å(1973) The ultrastructure of lateral line sense organs in the adult salamander *Ambystoma mexicanum*, J Neurocytol **2** 133–142.

[87] Kalmijn, AJ (1988) Hydrodynamic and acoustic field detection, in J Atema, RR Fay, AN Popper, & WN Tavolga (editors), *Sensory Biology of Aquatic Animals*, pp. 83–130 (Springer, New York).

[88] Kanter, M & Coombs, S (2003) Rheotaxis and prey detection in uniform currents by Lake Michigan mottled sculpin (*Cottus bairdi*), J Exp Biol **206** 59–60.

[89] Knudsen, EI (2002) Instructed learning in the audtory localization pathway of the barn owl, Nature **417** 322–328.

[90] Kreuz, T, Haas, JS, Morelli, A, & Abarbanel HDI, Politi, A (2007) Measuring spike train synchrony, J Neurosci Methods **165** 151–162.

[91] Kroese, AB & Netten, SM van (1989) Sensory transduction in lateral line hair cells, in S Coombs, P Görner, & H Münz (editors), *The Mechanosensory Lateral Line: Neurobiology and Evolution*, pp. 285–298 (Springer, New York).

[92] Kröther, S (2002) *Influence of Running Water on the Responses of Brainstem Lateral Line Units of Goldfish,* Carassius Auratus*, and the Rainbow Trout,* Oncorhynchus Mykiss, Phd thesis, Universität Bonn, Bonn.

[93] Kröther, S, Mogdans, J, & Bleckmann, H (2001) Brainstems lateral line response to sinusoidal wave stimuli in the goldfish, *Carassius auratus* in still and running water, J Exp Biol **104** 153–166.

[94] Künzel, S (2010) *Characterization of Brainstem Lateral Line Neurons in Goldfish* Carassius auratus*: Frequency Selectivity, Spatial excitation Patterns and Flow Sensitivity*, Phd thesis, Universität Bonn, Bonn.

[95] Lamb, HP (1932) *Hydrodynamics* (Cambridge University Press, Cambridge), 6

edition.

[96] Lewis, JE & Maler, L (2001) Neural population codes and the perception of object distance in weakly electric fish, J Neurosci **21** 2842–2850.

[97] Machens, CK, Stemmler, MB, Prinz, P, Krahe, R, et al. (1997) Representation of acoustic communication signals by insect auditory receptor neurons, J Neurosci **21** 3215–3227.

[98] Maher, G (1997) The use of image blur as a depth cue, Perception **26** 1147–1158.

[99] Mainen, ZF & Sejnowsky, T (1995) Reliability of spike timing in neocortical neurons, Science **268** 1503–1506.

[100] McCormick, CA (1989) Central lateral line mechanosensory pathway in bony fish, in S Coombs, P Görner, & H Münz (editors), *The Mechanosensory Lateral Line: Neurobiology and Evolution*, pp. 341–364 (Springer, New York).

[101] Mogdans, J & Kröther, S (2001) Brainstems lateral line response to sinusoidal wave stimuli in the goldfish, *Carassius auratus*, Zoology **104** 153–166.

[102] Montgomery, JC, Baker, CF, & Carton, AG (1997) The lateral line can mediate rheotaxis in fish, Nature **389** 960–963.

[103] Munk, A (editor) (2002) *Grundstudium Biologie Zoologie* (Fischer, Berlin).

[104] Münz, H (1979) Morphology and innervation of the lateral line system in Sarotherodon niloticus (L.) (*Cichlidea, Teleostei*), Zoomorphology **93** 73–86.

[105] Münz, H (1985) Single unit activity in the peripheral lateral line system in *Sarotherodon niloticus* l., J Comp Physiol A **157(4)** 555–568.

[106] Münz, H (1989) Functional organization of the lateral-line periphery, in S Coombs, P Görner, & H Münz (editors), *The Mechanosensory Lateral Line: Neurobiology and Evolution*, pp. 285–298 (Springer, New York).

[107] Nagiel, A, Ardó, D, & Hudspeth, AJ (2008) Specificity of afferent synapses onto plane-polarized hair cells in the posterior lateral line of the zebrafish, J Neuroscience **28** 8442–8453.

[108] Netten, SM van (2006) Hydrodynamic detection by cupulae in a lateral line canal: functional relations between physics and physiology, Biol Cyb **94** 1–19.

[109] New, JG, Alborg-Fewkes, L, & Khan, AN (2001) Strike feeding behavior in the muskellunge, Esox masquinongy: contributions of the lateral line and visual sensory systems, J Exp Biol **204** 1207–1221.

[110] Newman, EA & Hartline, PH (1981) Integration of visual and infrared information in bimodal neurons of the rattlesnake optic tectum, Science **213** 789–791.

[111] Nieuwenhuys, R (1982) An overview of the organization of the brain of actinopterygian fishes, Amer Zool **22** 287–310.

[112] Nieuwenhuys, R & Meek, J (1998) Holostean and telosts, in R Nieuwenhuys (editor), *The Central Nervous System of Vertebrates, 3 Volume*, pp. 759–937 (Springer, New York).

[113] Northcutt, RG (1989) The phylogenetic distribution and innervation of the

craniate mechanoreceptive lateral lines, in S Coombs, P Görner, & H Münz (editors), *The Mechanosensory Lateral Line: Neurobiology and Evolution*, pp. 17–78 (Springer, New York).

[114] Northcutt, RG (1992) Distribution and innervation of lateral line organs in the axothol, J Comp Neurol **325** 95–123.

[115] O'shea, RP, Blackburn, SG, & Ono, H (1994) Contrast as a depth cue, Vis Res **34** 1595–1604.

[116] O'shea, RP, Govan, DG, & Sekuler, R (1997) Blur and contrast as pictorial depth cues, Perception **26** 599–612.

[117] Patridge, BL & Pitcher, TJ (1980) The sensory basis of fish schools: relative roles of lateral line and vision, J Comp Physiol A **135** 315–325.

[118] Pearson, K (1901) On lines and planes of closest fit to systems of points in space, Philosophical Magazine **2** 559–572.

[119] Plachta, DTT, Hanke, W, & Bleckmann, H (2003) A hydrodynamic topographic map in the midbrain of goldfish *Carassius auratus*, J Exp Bio **206** 3479–3486.

[120] Pohlmann, K, Grasso, FW, & Breithaupt, T (2001) Tracking wakes: The nocturnal predatory strategy of piscivorous catfish, Proc Natl Acad Sci USA **98** 7371–7374.

[121] Pozrikidis, C (editor) (1997) *Introduction to Theoretical and Computational Fluid Dynamics* (Oxford University Press, New York).

[122] Puzdrowsky, RL (1989) Peripheral distribution and central projections of the lateral-line nerves in goldfish *Carassius auratus*, Brain Behav Evol **34** 110–131.

[123] Rieke, F, Warland, D, & de Ruyter van Steveninck, R (1997) *Spikes -Exploring the Neural Codes* (MIT press, Cambridge).

[124] Roddey, JC, Girish, B, & Miller, JP (2000) Assessing the performance of neural encoding models in the presence of noise, J Comp Neuro **8** 95–112.

[125] Sadeghi, SG, Chacron, MJ, Taylor, MC, & Cullen, KE (2007) Neural variability, detection thresholds and information transmission in the vestibular system, J Neurosci pp. 771–781.

[126] Sand, O (1981) The lateral line and sound reception, in WN Tavolga, AN Popper, & RR Fay (editors), *Hearing and Sound Communication in Fishes*, pp. 459–480 (Springer, New York).

[127] Satou, M, Takeuchi, HA, Nishii, J, Tanabe, M, et al. (1994) Behavioral and electrophysiological evidences that the lateral line is involved in the inter-sexual vibrational communication of the himé salmon (landlocked red salmon, *Oncorhynchus nerka*)., J Comp Physiol A **174** 539–549.

[128] Schlichting, H & Gertsen, K (2003) *Boundary Layer Theory* (Springer, Berlin).

[129] Schmitz, A, Bleckmann, H, & Mogdan, J (2006) Array morphology of the lateral line in goldfish *Carassius auratus*, in *99th annual meeting of the German Zool Soc* (Münster).

[130] Schwartz, E & Hasler, AD (1966) Superficial lateral line sense organs of the mudminnow, Z vergl Physiol **53** 317–327.

Bibliography

[131] Sichert, AB, Balmer, R, & van Hemmen, JL (2009) Hydrodynamic object recognition: When multipoles count, Phys Rev letter **102** 0581 041–4.

[132] Simmons, AM, Costa, LM, & Gerstein, HB (2004) Lateral line-mediated rheotactic behavior in tadpoles of the African clawed frog (*Xenopus laevis*)., J Comp Physio A **190** 747–758.

[133] Slee, SJ, Higgs, MH, Fairhall, AL, & Spain, WJ (2005) Two dimensional brain coding in the auditory brainstem, J Neurosci **25** 9978–9988.

[134] Sokolov, I, Klafter, Y, & Blumen, A (2002) Theory of arachnid prey localization, Physics Today. **55(11)** 48–55.

[135] Song, J & Northcutt, RG (1991) The primary projections of the lateral-line nerves of the florida gar, *Lepisosteus plathyrhincus*, Brain Behav Evol **37** 38–63.

[136] Stein BE, Stanford, TR (2008) Multisensory integration: Current issues from the perspective of the single neuron, Nat Rev Neuro **9** 255–266.

[137] de Ruyter van Stevenninck, R & Bialek, W (1988) Real-time performance of a motion-sensitive neuron in the blowfly visual system, Proc R Soc London B Biol Sci **234** 379–414.

[138] Vanegas, H, Ebesson, SOE, & Laufer, M (1984) Morphological aspect of the teleostean optic tectum, in H Vanegas (editor), *Comparative Neurology of the Optic Tectum*, pp. 93–120 (Plenum Press, New York).

[139] Vanegas, H, Williams, B, & Essayac, E (1984) Electrophysiology and behavioral aspect of the teleostean optic tectum, in H Vanegas (editor), *Comparative Neurology of the Optic Tectum*, pp. 121–162 (Plenum Press, New York).

[140] Wandell, BA (1995) *Foundations of Vision* (Sinauer Associates, Inc.).

[141] Webb, JF (1989) Gross morphology and evolution of the mechanoreceptive lateral-line system in teleost fish, Brain Behav Evol **33** 34–53.

[142] Wessel, R, Koch, C, & Gabbiani, F (1996) Coding of time-varying electric field amplitude modulations in a wave-type electric fish, J Neurophysiol **75** 2280–96.

[143] Wong, ROL (1999) Retinal waves and visual system development, Ann Rev Neurosci **22** 29–37.

[144] Zhang, LI, Tao, HW, Holt, CE, Harris, WA, et al. (1998) A critical window for cooperation and competition among developing retinotectal synapses, Nature **395** 37–44.

[145] Zittlau, KE, Claas, B, & Münz, H (1986) Directional sensitivity of lateral line units in the clawed toad *Xenops laevis* Daudin, J Comp Physiol. A **158** 469–477.